NTNU
Norwegian University of
Science and Technology

Experimental study of surface waves on strongly sheared currents

Laboratory, design, building, testing, and measurements

Eirik Æsøy

Mechanical Engineering
Submission date: December 2017
Supervisor: Simen Andreas Ådnøy Ellingsen, EPT

Norwegian University of Science and Technology
Department of Energy and Process Engineering

NTNU

Norwegian University
of Science and Technology

Department of Energy
and Process Engineering

EPT-M-2017-97

MASTER THESIS

for

Student Eirik Æsøy

August 2017

Experimental study of surface waves on strongly sheared currents: laboratory design, building,
testing, and measurements.

*Eksperimentell studie av overflatebølger på strømning med sterkt skjær: design, bygging og
testing av eksperimentelt oppsett, og målinger.*

Background and objective

In coastal waters, surface waves typically interact with currents which vary with depth. Such
shear currents will affect wave properties. The research group of Ass. Prof. S. Å. Ellingsen has
published a broad range of theoretical work on this subject, which will be tested in a new
laboratory which is to be built, tested and used by the student. Particular topics to be investigated
in the near future include (1) first observations of shear-modified 3D wave phenomena; ship
waves and ring waves, (2) careful measurement of shear-modified wave dispersion relations.

The following tasks are to be considered:

The following list is highly ambitious, to be considered a best-case scenario:

1. Building, implementation and testing of particle image velocimetry (PIV) setup for
   measuring shear flow velocity field.
2. Building, implementing and testing an optical Schlieren method for precise measurement
   of surface position in the presence of waves
3. Implementing a pneumatic system for non-intrusive wave generation, well controlled in
   time and space
4. Building and implementing a set of curved lattices for generation of controlled shear-
   currents, and studying these currents with respect to repeatability and downstream
   uniformity.
5. Combining the different elements (PIV, Schlieren, wave-maker) in a synchronised control
   programme (LabView)
6. Perform first qualitative and quantitiative measurement of 3D shear-modified wave
   phenomena
7. Perform measurements of wave dispersion relations with shear, and comparing with
   theoretical predictions.

Within 14 days of receiving the written text on the master thesis, the candidate shall submit a research plan for his project to the department.

When the thesis is evaluated, emphasis is put on processing of the results, and that they are presented in tabular and/or graphic form in a clear manner, and that they are analyzed carefully.

The thesis should be formulated as a research report with summary both in English and Norwegian, conclusion, literature references, table of contents etc. During the preparation of the text, the candidate should make an effort to produce a well-structured and easily readable report. In order to ease the evaluation of the thesis, it is important that the cross-references are correct. In the making of the report, strong emphasis should be placed on both a thorough discussion of the results and an orderly presentation.

The candidate is requested to initiate and keep close contact with his/her academic supervisor(s) throughout the working period. The candidate must follow the rules and regulations of NTNU as well as passive directions given by the Department of Energy and Process Engineering.
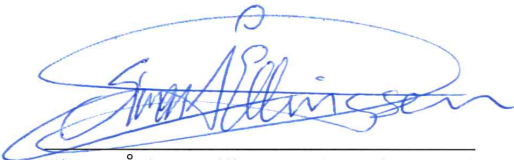
Risk assessment of the candidate's work shall be carried out according to the department's procedures. The risk assessment must be documented and included as part of the final report. Events related to the candidate's work adversely affecting the health, safety or security, must be documented and included as part of the final report. If the documentation on risk assessment represents a large number of pages, the full version is to be submitted electronically to the supervisor and an excerpt is included in the report.

Pursuant to "Regulations concerning the supplementary provisions to the technology study program/Master of Science" at NTNU §20, the Department reserves the permission to utilize all the results and data for teaching and research purposes as well as in future publications.

The final report is to be submitted digitally in DAIM. An executive summary of the thesis including title, student's name, supervisor's name, year, department name, and NTNU's logo and name, shall be submitted to the department as a separate pdf file. Based on an agreement with the supervisor, the final report and other material and documents may be given to the supervisor in digital format.

☒ Work to be done in lab (Fluids engineering lab)
☐ Field work

Department of Energy and Process Engineering, 24. august 2017

Simen Ådnøy Ellingsen, Associate Professor
Academic Supervisor

Research Advisor:

Summary

In this thesis experimental methods to measure shear-dependent wave dispersion is implemented and used to study waves propagating on currents. To achieve such measurements one needs to establish the following measurement systems listed below, which is the objectives of this work.

1. Measure surface topology both in space and time.

2. Generate waves which can be controlled in space and time.

3. Measure velocities present in the flow.

4. Generate steady and uniform shear flow conditions.

Surface topology: Two optical methods for reconstructing the liquid surface topology are implemented, tested and used in case study experiments, where wave phenomenon has been measured and compared to theory.

- **Fourier Transform Profilometry (FTP):** FTP is shown to be an accurate method for measuring how a free liquid surface deforms in space and time by analyzing the deformation of an optical fringe pattern reflected on the free surface. An optical method to calibrate system parameters are designed, tested, and implemented and is shown to be an accurate calibration method. Using FTP on a liquid surface depends on diffuse reflection, hence color pigment has to be added, where titanium dioxide is chosen as the pigment. The relation between pigment concentration and image quality is studied together with the effect on wave damping properties. Dispersion of linear surface waves is measured and compared to linear wave theory, which shows good correlation between measured values and theoretical predictions showing that FTP captures the periodicity and time development of the surface topology.

- **Free Surface Synthetic Schlieren (FS-SS):** FS-SS is also shown to be an accurate method to reconstruct surface topology. FS-SS relates diffraction of a dot pattern to the surface gradient and is compatible with Particle Index Velocimetry (PIV), which also requires a transparent fluid, hence topology and velocity can be measured simultaneously. However, this method measures the surface gradient, hence the topology is reconstructed by a least square inversion technique implemented. Dispersion experiments do not require the surface topology since the dispersion of waves can be related directly to the specter of the gradient components, hence the inversion is not necessary for shear dispersion studies. The accuracy of the reconstruction surface gradient is measured through dispersion measurements performed on linear waves in quiescent waters, where the known linear dispersion relation is compared to measured values. Wave patterns (surface topology) are also demonstrated in a study where ring and ship wave patterns in quiescent waters are measured and compared to theoretical predictions, which quantitatively show good agreement with theoretical predictions.

Wave-makers: To generate waves, two wave-maker mechanisms are implemented where spectrograms calculated from dispersion analysis shows agreement between generated waves and calculated wave spectrum from the measured surface topology. Wave-makers are used to generate waves used in experiments where dispersion data are used to calculate flow velocities and linear and nonlinear waves are studied and compared to theoretical predictions from wave theory.

Velocity measurements by Particle Image Velocimetry (PIV): To measure the velocity field an LED powered PIV system is designed and implemented where image pairs of tracer particles are used to calculate the average flow velocities in the camera focus plane. Velocities are measured and compared to measurements from an inversion technique where the the an integral relation between dispersion data and the vertical structure of the velocity profile is inverted.

Wave-tank and shear flow generation: A centrifugal pump is circulating water between two tanks flowing over a flat transparent plate, where both PIV and FS-SS are installed to measure surface topology and velocities occurring in the wave-tank. The flow is directed through a combination of a curved mesh and straight honeycombs which generates a depth varying velocity profile, which is approximately linear.

Inversion technique for current profile reconstruction: FS-SS, Wave-makers, and PIV are combined in a case study where space and time-averaged velocity profiles are measured both using PIV and shear affected dispersion data in an inversion algorithm, where the integral relation between wave-number dependent Doppler shifts and flow velocities are inverted to calculate the vertical structure of the current. Both methods show measurements in agreements with each other.

Sammendrag

I denne oppgaven har eksperimentelle teknikker for å måle skjær påvirket bølge dispersjon blitt utviklet, implementert, og testet. For å oppnå komplette målinger må følgende punkter oppnås, noe som er målsetningen til denne oppgaven, i tillegg til å kombinere og bruke metodene til å måle skjærpåvirker bølgedispersjon.

1. Måle veskeoverflate som beveger seg i tid og rom.

2. Generere bølger ved kjente bølgetall, og frekvenser.

3. Måle veskehastighet som er til stede i strømningen.

4. Generere tidsuavhengige og uniforme strømningsforhold.

Måling av væskeoverflate: To metoder for å måle væskeoverflate er implementert og testet gjennom case studier hvor bølge fenomener er målt og sammenlignet med teoretiske predikasjoner.

- **Fourier Transform Profilometry (FTP):** FTP er vist til å være en nøyaktig metode for å måle væskeoverflate som beveger seg i tid og rom ved å analysere deformasjonen av et optisk periodisk mønster prosjektert på væskeflaten. En optisk metode for å kalibrere systemparametere er utviklet, testet, og viser seg å være en nøyaktig og effektiv metode. For å bruke FTP på en væskeflate, er man avhengig av diffus refleksjon som oppnås ved å tilsette fargepigmenter til væsken, hvor titaniumdioksid er valgt i denne studien. Relasjonen mellom pigment konsentrasjon og bilde kvalitet er målt sammen med effekten pigmentkonsentrasjon har på demping av overflaten. Bølgedispersjon er også målt og viser god korrelasjon med teoretisk dispersjonsrelasjon, noe som viser at FTP måler periodisiteten og tidsavhengigheten nøyaktig.

- **Free Surface Synthetic Schlieren (FS-SS):** FS-SS er også vist til å være en nøyaktig metode for å måle væsketopologi. FS-SS relaterer diffraksjonen av et mønster visualisert gjennom den frie overflaten til gradienten, hvorav vinkelen til overflaten måles. Metoden er avhengig av gjennomsiktig væske og er derav kompatibelt med Particle Index Velocimetry (PIV) som måler væskehastigheter direkte. Siden det er vinkelen til væskeflaten som måles, må man invertere gradientfelt for å få overflatetopologien noe som gjøres ved en inversjonsteknikk implementert i denne oppgaven. Bølgedispersjon kan kobles direkte til gradientfeltet, noe som fører til målingene fra FS-SS kan brukes direkte til å analysere skjærpåvirket dispersjon. Nøyaktigheten av metoden er målt gjennom dispersjonsmålinger hvor lineære bølger er målt i stille vann og sammenlignet ved kjent dispersjonsrelasjon. Inversjonsteknikken er også demonstrert ved at kjente bølgemønstre er målt og sammenlignet med teoretiske predikasjoner.

Bølgegenerering: Til å generere bølger er to metoder utviklet, implementert, og testet. Nøyaktigheten er målt gjennom sammenligning av bølgespekter kalkulert fra målinger av fri væskeflate, og påtrykt bølgekarakteristikk fra bølgemakerne.

Strømningshastigheter fra Particle Image Velocimetry (PIV): For å måle strømningshastigheter er et LED drevet PIV system designet og implementert hvor man via bildepar av partikler som følger strømningen kan kalkulere strømningshastigheter.

Bølgetank og generering av skjærstrømning: En sentrifugalpumpe sirkulerer vann mellom to tanker tilkoblet med en gjennomsiktig plate hvor vannet strømmer over. PIV og FS-SS er installert for å måle overflatetopologi og strømningshastigheter. For å generere skjærstrømning, er vannet ledet gjennom kurvet hønsenetting og en finmasket honeycombseksjon fro å lede strømlinjene og generere an dybdeavhengig hastighetsprofil.

Strømprofilinversjon fra måling av skjærpåvirket bølgedispersjon: FS-SS, Bølgemakere, og PIV er installert og kombinert i forsøk, hvor skjærpåvirket bølgedispersjon er brukt for å måle strømningshastigheter. Dette er gjort ved å invertere et integralforhold mellom bølgedispersjonen målt fra FS-SS, og hastighetsprofilet som påvirker bølgemønsteret. Hastighetsprofilet som er målt fra dispersjonsdata, er videre sammenlignet med målingene fra PIV.

Preface

This thesis is written at the Fluid Mechanics group at the Department of Energy and Process Engineering at NTNU Trondheim. The work was initiated autumn 2016 and the design, building and laboratory experiments were performed from spring 2017 to winter 2017, and finalizes my 5-year education as a Mechanical Engineer at NTNU.

First of all, I would like to thank Ph.D. Candidate Benjamin Keeler Smeltzer, who has largely participated in the work presented in this thesis and has acted as a co-supervisor as well as a coworker. I would also like to thank my supervisor Simen Andreas Ådnøy Ellingsen for his great support, guidance, and help throughout the project and master-work.

Beside my supervisors, I would like to thank the workshop staff and especially Arnt Egil Kolstad, who has been very helpful with practical consultation in the laboratory.

Last but not least I would like to thank my family for support and help, especially in the writing process, which at times have been demanding.

Table of Contents

Nomenclature

Symbols

Detailed lists of symbols are given in the introduction of each chapter.

Abbreviations

FTP Fourier Transform Profilometry

PIV Particle Image Velocimetry

FS-SS Free Surface Synthetic Schlieren

SNR Signal-to-Noise Ratio

ADCP Acoustic Doppler Current Profiler

LED Light Emitting Diode

CCD Charge Coupled Device

DTFT Discrete Time Fourier Transform

FFT Fast Fourier Transform

DIC Digital Image Correlation

CC Cross Correlation

LSI Least Square Inversion

HPF Hight Pass Filter

LPF Low Pass Filter

NC Noise Capping

IC Intensity Capping

Chapter 1

Introduction

1.1 Background

The study of water waves is one of the main fields of fluid mechanics. Water waves can be fascinating to look at, but also destructive. Humans are dependent on coastlines and the oceans where constructions, vessels, installations, and operations are typically affected by forces from waves and currents. Waves and ocean currents are also playing a major role in transfer processes such as transfer of momentum, heat, and mass, which is important for understanding local and global climate and bioprocesses. Therefore monitoring ocean behavior is of great importance, and improved techniques to perform measurements of waves and currents are required. Current measurements in the upper ocean layers are hard to perform by traditional methods, such as acoustic Doppler current profiler (ADCP), where the received signal is contaminated by disturbances from waves normally down to 20 meters. Other measurement techniques where probes are inserted into the flow experiences similar problems and methods which are able to distinguish between wave-induced velocities and current velocities are needed. Methods using wave dispersion data to do current predictions in the upper ocean layer are being developed, where Bragg scattering measured by X-band radar is related to wave patterns, which are used to calculate shear affected wave dispersion that are used to calculate the average depth varying current[1, 2].
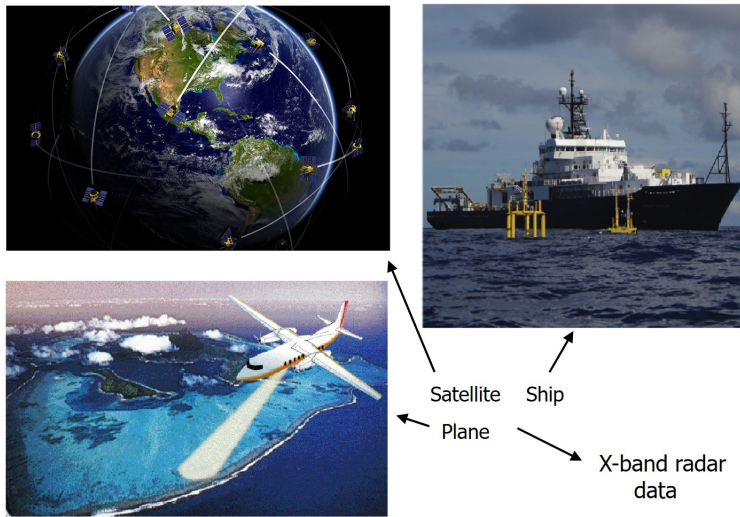
Figure 1.1: X-band radar systems can be installed on planes [1], ships [2], or satellites [2], hence due to the range of application, the method has great potential.

In theory, the technique should works on different scales (seen in Figure 1.1), provided that there are waves on the respective scale to be measured. Dispersion data can be obtained from X-band radar measurement of the ocean surface(example from ship seen in Figure 1.2), where the radar can be installed on land, vessels, airplanes, or satellite, hence the due to the range of applications, the technique has great potential.
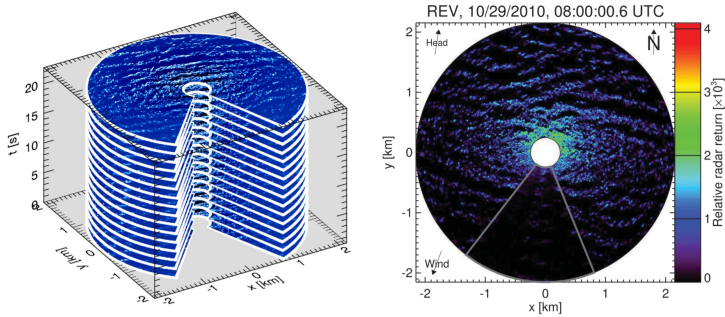

Figure 1.2: Dispersion data (left) calculated from surface topology (right) measured by an X-band radar system installed on a ship [2].

---

[1]https://earth.esa.int/documents/10174/2052852/c3_side-looking_full.jpg
[2]http://www.spatial-business-integration.com/wp-content/uploads/2015/04/F_7_Satellite-data-tuning-for-index-interoperability.jpg

The relation between depth varying currents and wave dispersion has been studied by scientists over the years [3, 4, 5]. To calculate velocities from dispersion measurements, an inversion of an integral relation between shear affected dispersion and current profiles derived by R. H. Steward and J. W. Joy [6], later extended by J. T. Kirby and T. M. Chen [5] is performed. The relation relates the depth-averaged current to a wave number dependent Doppler shift of the wave dispersion, which is calculated by performing a weighted integral over the water depth. This integral method has been extensively used to describe wave phenomenon affected by non-uniform currents, and only recently new alternative methods have been proposed to estimate these relations [7, 8], which is superior to the previous methods. The relations have been extended to 3D were wave phenomenon generated by moving objects (ships) or initial disturbances (impulse responses) influenced by sheared currents have been studied, resulting in asymmetric patterns [9, 10].

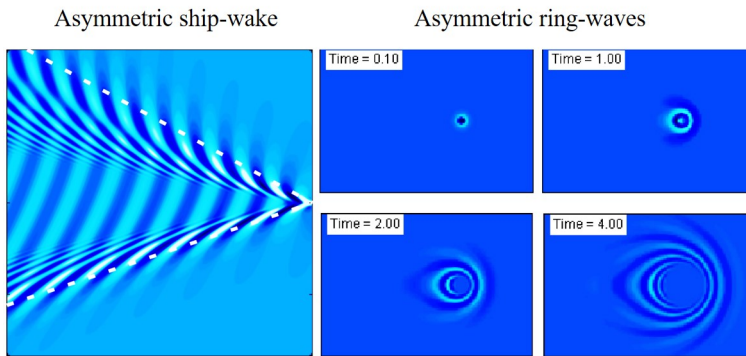**Figure 1.3:** Asymmetric wave pattern caused by shear dispersion [9, 10].

Until now the X-band radar current measurements are evaluated by comparing with (ADCP), which fails in the region of interest. Proper evaluation and improvement on the methods are needed, hence laboratory scale experiments, where one has full control parameters are an important step towards proper evaluation of the inversion method.

1.2 Research objectives

This study aims to build and implement experimental methods to study waves propagating on depth varying currents, where proper evaluations of inversion algorithms can be performed as well as studies of asymmetric wave patterns caused by shear dispersion. The research objectives are summarized below, where following goals are established.

1. **Free surface measurements:** The free surface topology is needed to reconstruct wave patterns and obtain dispersion data for water current analysis.

2. **Velocity measurements:** The velocity field needs to be measured to evaluate the actual flow conditions as well as to evaluate the accuracy of the current inversion.

3. **Wave generation:** Waves needs to be generated, ideally in a way where both periodicity (wavelength) and amplitude can be tuned and controlled.

4. **Flow conditions:** Wanted shear flow conditions needs to be generated such that parametric studies can be performed on different shear profiles.

5. **Combining methods for case studies:** When the above objectives are met, combining to perform case studies to test methods and study wave-current interaction.

Project work:

The work performed in this thesis started autumn 2016 where an experimental flow channel was designed and built at the fluid mechanic's laboratory at NTNU. The tank was finished May 2017, and Parallel to the construction, testing of a method to measure surface topology were perform in a separate tank as project work as well as a method to generate controlled surface perturbations.

Surface measurements: Fourier Transform Profilometry (FTP) is an optical method were phase deformations of a projected fringe pattern is analyzed to reconstruct topology. The method was first developed by Takeda and Mutoh[11], and has been used by scientists for different purposes[12, 13, 14, 15]. The following steps were performed during spring 2017 in the project thesis.

- Technical implementation

- Optical calibration technique

- Data analysis

- Experiments in quiescent waters

Project work
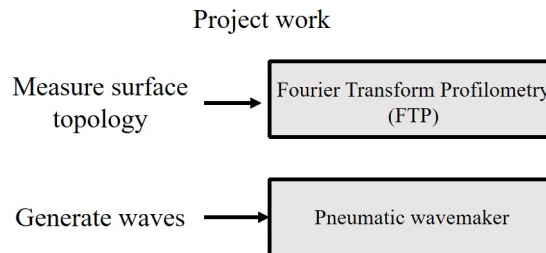
Figure 1.4: Methods implemented in the project thesis. FTP was implemented to measure surface topology and a pneumatic wave-maker was implemented to generate waves.

Wave-maker: To generate waves several methods were discussed, and the first implementation was to use a pneumatic jet as a pressure wave-maker (later supplemented by a mechanical wave-maker). An analytic model is derived and tested through stagnation point measurements by a differential pressure sensor and a pitot tube.

- Pressure model

- Technical implementation

- Model verification

Master work:

When the construction of the flow channel was finished the work progressed where methods to generate suitable shear flow conditions, and measure velocities were implemented.

Shear flow generation: Several methods to achieve a sheared velocity profile were investigated based on literature and a combination of flow straightening honeycombs and curved meshes are constructed and implemented [16, 17, 18, 19].

- Technical implementation
- Flow measurements
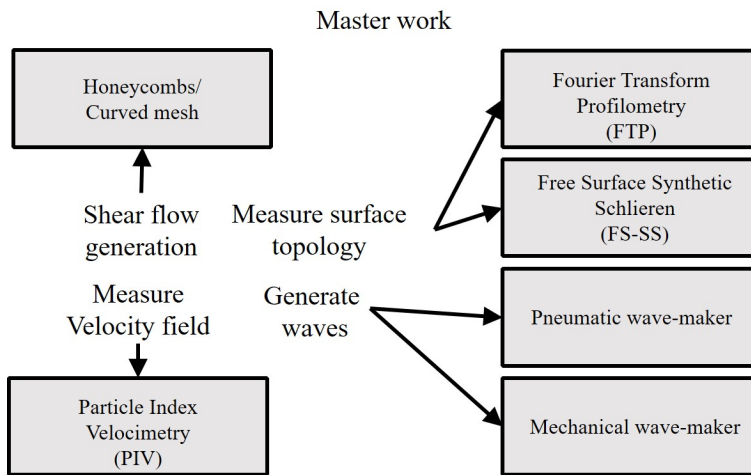
Figure 1.5: Master thesis objectives to perform experiments on wave shear interactions.

Flow measurements: To measure velocities several methods, such as pitot tube, Laser Doppler Velocimetry (LDV), and Particle Image Velocimetry (PIV) was discussed and the decision landed on PIV, which is an optical method where movement of illuminated tracer particles are measured and related to flow velocities [20, 21, 22]. A setup inspired by Willbert, Stasicki, Klinner, and Moesseners PIV setup[20], where high power LED's are used as a pulsing light source, is designed, built and implemented.

- Technical implementation
- Data analysis
- Flow measurements

Surface topology: FTP is not compatible with PIV measurements. Therefore, a synthetic schlieren method, where the free surface gradient is measured by refraction of a random dot pattern is tested and implemented, which is inspired by the setup developed by Mosiy, Rabaud and Salsac [23].

Case studies:

Case studies are performed where the experimental methods are combined (Figure 1.6) to measure wave phenomenon (as case studies listed below) both propagation on currents and in quiescent waters.

1. Damping of waves.

2. Ring and ship wave patterns.

3. Nonlinear waves and wave steepness.

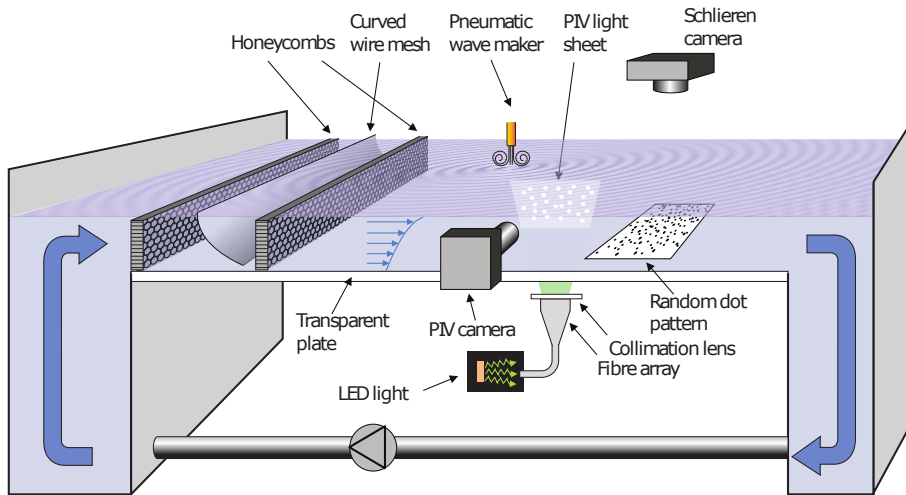4. Velocity measurements by current inversion of dispersion data.

Figure 1.6: Combining experimental methods for case studies (fig. by S.Å.E).

1.3 Structure of the thesis

The following list shows the structure of the thesis. chapter 2 consists of wave theory where the mathematical descriptions of waves are derived or illustrated for the simplest case of linear waves in quiescent, nonlinear waves solved by stokes expansion, and current wave interactions waves propagating on uniform, linear, and arbitrary currents. In the end of the chapter an algorithm where current profiles are calculated from inverting the relationship between shear affected wave dispersion and the corresponding sub surface current are shown and demonstrated on mock data. In chapter 6 all the theories are tested through experiments of waves propagating in quiescent waters, or on a variety of currents, where the current inversion algorithm will be used on data obtained from experiments of waves propagating on real currents and compared to velocity measurements by Particle Image Velocimetry.

chapter 3 describes the theoretical background and gives a detailed descriptions of the signal processing algorithms used to obtain physical quantities from the various signals measured with the experimental methods implemented in this thesis, which are later implemented in chapter 4.

1. chapter 2: Wave theory.

2. chapter 3: Theory for experimental methods.

3. chapter 4: Implementation of experimental methods.

4. chapter 5 and chapter 6: Case studies of waves.

Chapter 2

Free surface flows

A free surface is a surface that is not subjected to parallel shear forces. In a gravitational field, a free surface will form between liquids of different densities, where the heavier liquid forms the bottom layer. The ocean seen in Figure 2.1 is an example of where the water density is roughly thousand times greater then that of atmospheric gasses, hence is subjected to higher gravitational force and forms a free surface. Under mechanical equilibrium, this free surface must be perpendicular to forces acting on the fluid which is a concept exploited when the mathematical description of a free surface is defined.
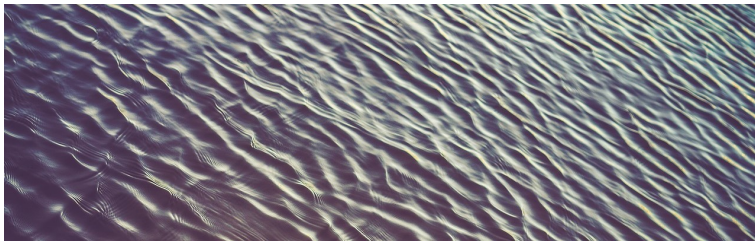
Figure 2.1: The ocean is an example of a free liquid surface[1].

This project focuses on the interface between liquid and gas, where the gas density is normally several orders of magnitude smaller and can therefore be neglected. This simplifies the analysis although the procedure for the interface between two immiscible fluids are the same. The procedures presented in this section is a common way to formulate water wave theory and similar or identical approaches with more details can be found in several textbooks [24, 25, 26, 27, 28]. All the content in this chapter will be used later (in chapter 5 and chapter 6) when experimental measurements are compared to theoretical predictions described in this chapter.

---

[1]https://cdn.pixabay.com/photo/2017/08/07/20/27/nature-2607484_1280.jpg

Symbols used in Wave Theory

(x, y, z)	Cartesian coordinates	c	Wave phase velocity
(r, θ, z)	Polar coordinates	s	Wave steepness
g	Gravitational constant	T	Wave period
ρ	Fluid density	h	Water depth
σ	Fluid surface tension	F	Force
u	Fluid velocity	F_σ	Surface tension Force
μ	Fluid dynamic viscosity	σ_{ij}	Fluid stress tensor
ν	Fluid kinematic viscosity	δ_{ij}	Kronecker delta
f	Fluid volume force	$R_{1,2}$	Radii of curvature
E	Fluid Energy	ϕ	Velocity potential
p	Fluid pressure	U	Fluid velocity
Φ	Viscous dissipation	S	Shear parameter
q	Heat flux	ϵ	Expansion parameter
ζ	Surface height	ϵ_e	Inversion residual
λ	Wavelength	J_0	Bessel Function of the First Kind
k	Wave number	t	Time
a	Wave amplitude	τ	Time
ω	Wave angular velocity	H	System impulse response

2.1   Wave theory - problem description

Governing equations: The starting point in most fluid flow analysis is the momentum, continuity, and energy equations, which are valid for the vast majority of flow problems. To solve these equations, simplifications and assumptions are essential to reduce the complexity of the problem. If the free surface is subjected to a disturbance waves will form, which can be expressed as periodic functions that have to satisfy the equations expressed in Equation 2.1. ρ and ν are the fluid density and dynamic viscosity, which are fluid properties assumed to be constant. $\mathbf{u}$ is the velocity vector consisting of components (u, v, w). Equation 2.1b is the Navier-Stokes equation which is Newton's second law of motion formulated for an incompressible Newtonian fluid. p is the mechanical pressure. $\mathbf{f}$ is the volume force, which for most cases are the gravitational force $g\vec{a_z}$. $E = U + \frac{1}{2}u_i u_i$ is the energy where U is the internal and $\frac{1}{2}u_i u_i$ is the kinetic energy. Φ is viscous dissipation and $\mathbf{q}$ is the heat flux.

$$\frac{D\rho}{Dt} + \rho(\nabla \cdot \mathbf{u}) = 0 \tag{2.1a}$$

$$\frac{D\mathbf{u}}{Dt} = -\frac{1}{\rho}\nabla p + \nu\nabla^2\mathbf{u} + \mathbf{f} \tag{2.1b}$$

$$\frac{DE}{Dt} + \frac{p}{\rho}(\nabla \cdot \mathbf{u}) = \Phi + \mathbf{q} \tag{2.1c}$$

$$\frac{D[*]}{Dt} = \frac{\partial[*]}{\partial t} + (\mathbf{u} \cdot \nabla)[*] \tag{2.1d}$$

Scale	Dimensionless variable	Dimensionless number	Expression
Length	$x^* = x/L$	Reynolds number	$Re = UL/\nu$
Velocity	$u^* = u/U$	Froud number	$Fr = U/\sqrt{gL}$
Time	$t^* = tU/L$		
Pressure	$p^* = p/\rho U^2$		

Table 2.1: Scales and dimensionless numbers introduced in the governing equations.

Scaling and simplification: Scales are chosen (Table 2.1) such that Equation 2.1b become dimensionless (Equation 2.2a). The velocity and length scales for waves are the phase velocity (c) and the wavelength (λ) and a Reynolds number can be expressed as $Re = c\lambda/\nu$, which is large for most waves ($Re \gg 1$), hence viscous terms can be neglected and the wave motion is described by the Euler equations. Another assumption is that the fluid is incompressible and the continuity equation simplifies, hence the energy equation is not needed to describe pressure and velocities, which reduces the complexity of the problem significantly. Waves that satisfies these assumptions can therefore be described by the Euler equations and the simplified continuity equation expressed in Equation 2.2b.

$$\frac{D\boldsymbol{u}^*}{Dt^*} = -\nabla^* p^* + \frac{1}{Re}\nabla^{*2}\boldsymbol{u}^* + \frac{1}{Fr^2}\boldsymbol{f}^* \qquad \frac{D\rho}{Dt} + \rho(\nabla \cdot \boldsymbol{u}) = 0 \qquad (2.2a)$$

$$\frac{D\boldsymbol{u}}{Dt} = -\frac{1}{\rho}\nabla p + \boldsymbol{f} \qquad \nabla \cdot \boldsymbol{u} = 0 \qquad (2.2b)$$

Symbol	Value	Unit
ρ	1000	[kg/m^3]
σ	0.072	[N/m]
μ	1×10^{-3}	[Pa s]
g	9.81	[m/s^2]

Table 2.2: Fluid properties for water at $25°$C.

Free surfce height: (ζ): The free surface height (ζ) is described as a vector pointing at the free surface with $z = 0$ as a reference, which along with pressure and velocities needs to be described through equations.
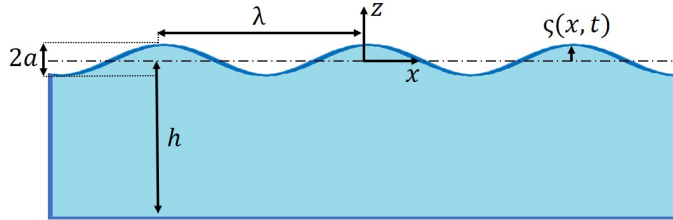

Figure 2.2: Important wave parameters. ζ describes the height of the wave relative to the reference plane $z = 0$. h is the water depth. λ is the wavelength, and a is the amplitude of the wave.

$$\zeta(\mathbf{x}, t) = a \cos\left(\mathbf{k} \cdot \mathbf{x} - \omega t\right) \quad \mathbf{u} = (u, v, w) \quad p(\mathbf{x}, t) \tag{2.3}$$

$\mathbf{x}$ is spatial coordinates (usually chosen to be (x, y, z) or (r, θ, z)), and $\mathbf{k}$ are wave-numbers related to direction of propagation $((k_x, k_y)$ or $(k_r, k_\theta))$.Table 2.3 shows important parameters and relations for waves, and Figure 2.2 shows the geometry for a plane wave $\zeta(x, t)$ propagating in the x-direction.

Name	Symbol	Relation	Unit
Wavelength	λ		$[\text{m}]$
Wavenumber	k	$2\pi/\lambda$	$[1/\text{m}]$
Amplitude	a		$[\text{m}]$
Angular velocity	ω	$\omega = 2\pi/T$	$[1/\text{s}]$
Wave period	T		$[\text{s}]$
Phase velocity	c	$c = \omega/k$	$[\text{m/s}]$
Steepness	s	$s = ka$	$[-]$

Table 2.3: Important wave parameters. Some of the parameters are related to each other but have different physical meaning.

Boundary conditions: To fully describe the problem, boundary conditions need to be established where three conditions are derived from conservation laws, and kinematics.

Impermeability (Wall condition): The first condition is that no water can penetrate the seabed (Figure 2.3), which is known as impermeability and can be mathematically described by Equation 2.4.
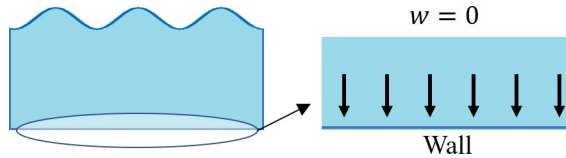
$$w|_{z=-h} = 0 \tag{2.4}$$

Figure 2.3: Impermeability conditions. No fluid can penetrate a wall and the normal velocity must be zero.

Kinematic boundary condition: The second condition is that a particle has to stick to the surface, and a kinematic condition is describe through the material derivative of $z - \zeta$, which is mass concervation of a moving boundary (Figure 2.4). $\frac{\partial z}{\partial t} = u\frac{\partial z}{\partial x} = v\frac{\partial z}{\partial y} = 0$ and $w\frac{\partial z}{\partial z} = w$ since z is a constant reference plane and hence the kinematic boundary condition simplifies to Equation 2.5.

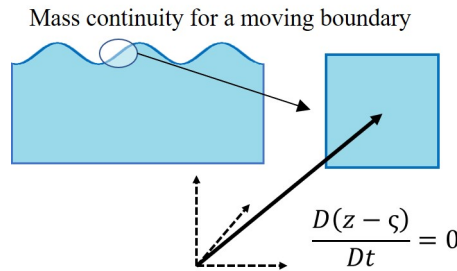$$\frac{D(z - \zeta)}{Dt} = 0 \Rightarrow \frac{D\zeta}{Dt} = w \tag{2.5}$$

Figure 2.4: Kinematic boundary condition on the free surface. The free surface is a moving boundary where no mass is transported through.

Dynamic boundary condition: (Force equilibrium) The third condition is called the dynamic boundary condition which is a force equilibrium at the free surface (Figure 2.5).

$$\sum F = 0 \tag{2.6}$$

When the surface has curvature ($\nabla^2 \zeta \neq 0$), surface tension forces (F_σ) acts along the surface seeking to minimize surface area, leading to a discontinuous pressure jump, which can be related to the curvature according to the Young-Laplace relation (Equation 2.7) [29].

$$F_\sigma = \sigma \frac{1}{R1} + \frac{1}{R2} = -\sigma \left[\frac{\zeta_{xx}}{\sqrt{1+\zeta_x^2}} + \frac{\zeta_{yy}}{\sqrt{1+\zeta_y^2}} \right] \approx -\sigma \left[\zeta_{xx} + \zeta_{yy} \right] \tag{2.7}$$

The free surface is by definition perpendicular to the forces acting on it hence there are no shear forces acting on the free surface and the stress tensor reduces to a pressure balance over the free surface.

$$\sigma_{ij} \Rightarrow -\delta_{ij} p \tag{2.8}$$

σ_{ij} is the stress tensor which reduces to a pressure difference, which occurs at a free surface. δ_{ij} is the Kronecker which is 0 when $i \neq j$ and 1 when $i = j$. In Equation 2.7 R_1 and R_2 represents the radii of curvature in each of the axes parallel to the surface, which is related to the curvature of ζ. An equation coupling pressure forces in the fluid and the free surface curvature is established (Equation 2.9).

$$p_{\text{above}} = p_{\text{below}} + F_\sigma \Rightarrow p_{\text{above}} = p_{\text{below}} - \sigma(\zeta_{xx} + \zeta_{yy}) \tag{2.9}$$
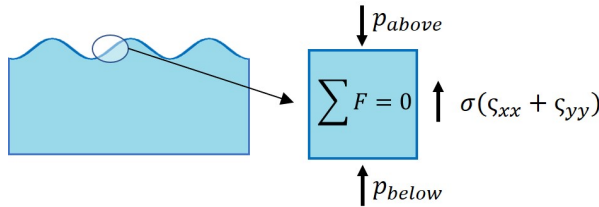

Figure 2.5: Mechanical equilibrium. Pressure and surface tension forces acting on the fluid at the free surface must be in equilibrium.

2.2 Linear waves - potential solution

Linear waves: In linear theory, the wavelength (λ) is much larger than the amplitude (a) indicated by the steepness parameter $(ka \ll 1)$. All higher order terms of (ζ, ϕ) can therefore be neglected, which reduces the problem significantly, since in general the Euler equations are non-linear.

Potential field(ϕ): Another assumption that simplifies the analysis is to consider the flow to be irrotational, which means that the vorticity is zero. For irrotational flow the velocity field can be described as a potential field ϕ, which has to satisfy the Laplace equation. Substituting ϕ for velocities into the Euler equations reduces it to the unsteady Bernoulli equation expressed in Equation 2.10b.

$$\omega = \nabla \times \mathbf{u} = 0 \qquad \nabla^2 \phi = 0 \qquad \frac{\partial \phi}{\partial x_i} = u_i \tag{2.10a}$$

$$\phi_t + \frac{1}{2}(\phi_x^2 + \phi_y^2 + \phi_z^2) + gz + \frac{p}{\rho} = \text{constant} \tag{2.10b}$$

Simplified equations: The unsteady Bernoulli equation is used to express the pressure (p_{below}) in the fluid, reducing the dynamic and kinematic boundary condition to Equation 2.11c and Equation 2.11d, which has to be satisfied by ϕ and ζ along with the Laplace equation and Impermeability.

$$\nabla^2 \phi = 0 \tag{2.11a}$$

$$\phi_z|_{z=-h} = 0 \tag{2.11b}$$

$$\zeta_t = \phi_z|_{z=0} \tag{2.11c}$$

$$\phi_t|_{z=0} + g\zeta = \frac{\sigma}{\rho}(\zeta_{xx} + \zeta_{yy}) + \frac{p_{\text{above}}}{\rho} \tag{2.11d}$$

The Laplace equation can be solved by separation of variables where k has to be constant.

$$\frac{X''}{X} + \frac{Y''}{Y} = -\frac{Z''}{Z} = -k^2 \tag{2.12a}$$

$$X = e^{ik_x x} \quad Y = e^{ik_y y} \quad Z = e^{kz} \quad k_x^2 + k_y^2 = k^2 \tag{2.12b}$$

If $Z = \cosh k(z + h)$, ϕ satisfies Equation 2.11b. The expressions for ϕ and ζ are substituted into the boundary conditions on the free surface resulting in ordinary differential equations (ODE) for coefficients A and B, which are coupled and has the form of wave equations. ω is the angular velocity, which is related to the wave speed and is coupled to the spatial wave-number through the linear dispersion relation (Equation 2.13c), which will be discussed in the next section.

$$\phi(t, r, z) = Ae^{i\mathbf{k}\cdot\mathbf{x}} \cosh k(z + h) \qquad \zeta(t, r) = Be^{i\mathbf{k}\cdot\mathbf{x}} \tag{2.13a}$$

$$\ddot{B} + \omega^2 B = 0 \quad \ddot{A} + \omega^2 A = 0 \tag{2.13b}$$

$$\omega^2 = k[g + \frac{\sigma}{\rho}k^2] \tanh hk \tag{2.13c}$$

The general solution for A and B is given by Equation 2.14, where all solutions at different values of k are added (integrated), hence the total solution is expressed as a Fourier integral over all wave-numbers.

$$\phi(t, r, z) = \int \frac{d^2k}{2\pi^2} \frac{i\omega}{k} [C_+ e^{i\omega t} - C_- e^{-i\omega t}] e^{i\mathbf{k}\cdot\mathbf{x}} \frac{\cosh k(z + h)}{\sinh kh} \tag{2.14a}$$

$$\zeta(t, r) = \int \frac{d^2k}{2\pi^2} [C_+ e^{i\omega t} + C_- e^{-i\omega t}] e^{i\mathbf{k}\cdot\mathbf{x}} \tag{2.14b}$$

Initial conditions: The constants in Equation 2.14 has to be determined from initial conditions and can be expressed by substituting the Fourier components $\hat{\zeta}_0$ and $\dot{\hat{\zeta}}_0$ into Equation 2.14b and solve for $C_\pm$ (Equation 2.15).

$$C_\pm = \frac{1}{2}[\hat{\zeta}_0 \pm \frac{1}{i\omega}\dot{\hat{\zeta}}_0] \tag{2.15}$$

Dispersion relation and regimes:

The dispersion relation for linear waves is perhaps the most important relation which will be measured experimentally in different configurations in chapter 5 and chapter 6.

Dispersion relation: An important result is Equation 2.16a, which is called the dispersion relation that contains important features of surface waves. In the previous section the free surface was described as a sum of single harmonics and the dispersion relation relates the angular velocity (ω) to the wavenumber (k). Phase velocities ($c = \omega/k$), which is the absolute speed of the wave is is in general wave number dependent and an initial wave packet will spread out and disperse as the different wavelengths it consists of propagates in space. Equation 2.16b determines the group velocity which is related to the velocity of the overall shape of the waves amplitude commonly known as *modulation* or *envelope* of the wave. The group velocity is related to the energy propagation of a *wave packet* and both c and c_{group} can be viewed from the dispersion relation curve as the average slope ω/k, and the gradient $\partial\omega/\partial k$.

$$\omega^2 = k[g + \frac{\sigma}{\rho}k^2]\tanh hk \qquad \text{Bo} = \frac{\rho g}{\sigma k^2} \tag{2.16a}$$

$$c = \frac{\omega}{k} \qquad c_{group} = \frac{\partial\omega}{\partial k} \tag{2.16b}$$
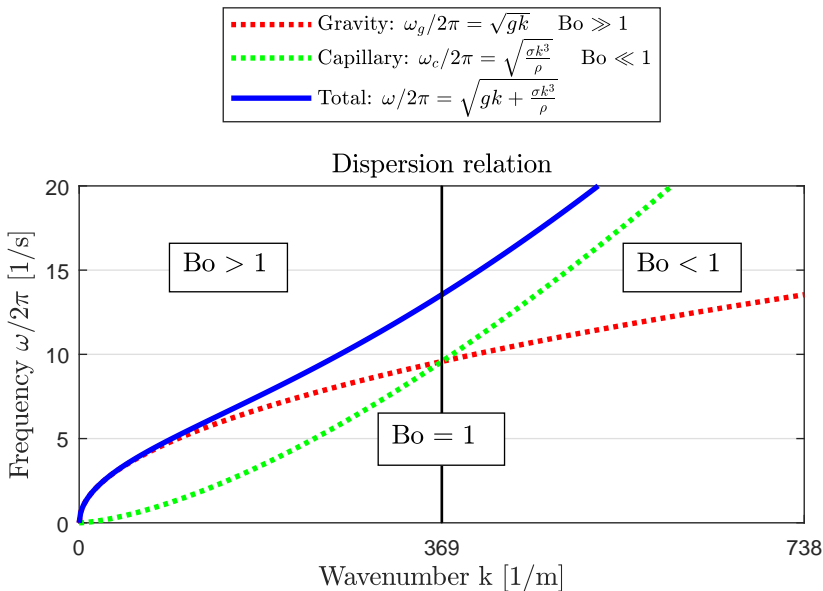

Figure 2.6: Dispersion relation for linear waves which contains information about angular velocity ω, phase velocity c, and group velocity c_{group}.

Bond number: Dispersion of water waves are driven by gravity (g) and surface tension $(\sigma k^2/\rho)$ forces. The relative importance are related to the Bond number, which determines the ratio of these two forces. Bo $\gg 1$ implies that gravity forces dominates (called gravity waves) and Bo $\ll 1$ means that surface tension dominates (called capillary waves).
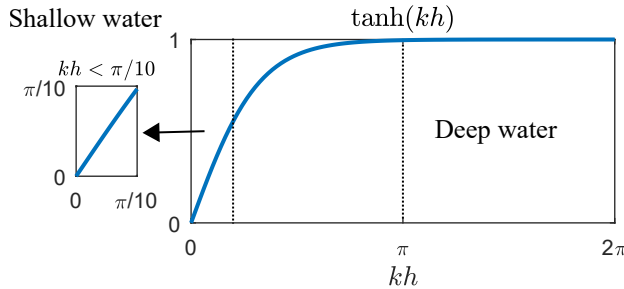

Figure 2.7: Bottom effect on dispersion. Waves where $kh < \pi/10$ is constrained, while $kh > \pi$ is unconstrained by the bottom.

Depth and bottom effects: The term $\tanh(kh)$ determines how much the bottom is constraining the wave motion. When the depth becomes sufficiently large $(kh > \pi)$, the wave is not affected by the bottom and $\tanh(\pi) \approx 1$ (right in Figure 2.7), which are called deep water waves. The wave motion will not penetrate deeper than $z = \lambda/2$ (Figure 2.8). If $h \ll \lambda/2$, $\tanh(kh)$ becomes approximately linear $(\tanh(kh) \approx kh)$ and the wave is fully constrained by the bottom (called shallow water waves). The limit for this is often set to $h < \lambda/20$ (left in Figure 2.7).
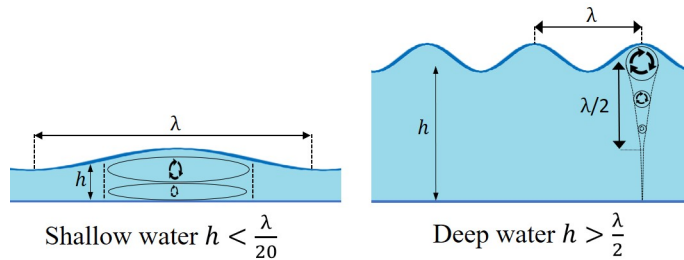

Figure 2.8: Orbital paths for waves at deep and shallow water regimes. For deep water waves, the motion only penetrates half of the wavelength toward the seabed, while shallow water is fully affected by the bottom.

Regimes: Waves defined in this section can be sorted into four regimes (Table 2.4), where both capillary and gravity waves might occur in deep or shallow waters.

	Deep $h > \frac{\lambda}{2}$	Shallow $h < \frac{\lambda}{20}$
Gravity waves $\text{Bo} \gg 1$	$c = \sqrt{\dfrac{g}{\|k\|}}$ $c_{\text{group}} = \frac{1}{2}c$	$c = \sqrt{gh}$ $c_{\text{group}} = c$
Capillary waves $\text{Bo} \ll 1$	$c = \sqrt{\dfrac{\sigma\|k\|}{\rho}}$ $c_{\text{group}} = \frac{3}{2}c$	$c = \|k\|\sqrt{\dfrac{\sigma h}{\rho}}$ $c_{\text{group}} = 2c$

Table 2.4: Phase and group velocities at different flow regimes.

2.3 Nonlinear Stoke waves

In chapter 6, steepness parameter and dispersion of nonlinear Stoke waves will be estimated from measurements and compared to theory described in this section.

The theory in section 2.2 is derived with the assumption that the steepness (ka) is small, which is not the case for nonlinear waves, hence the linearization performed of Equation 2.10 is not valid. However, the velocity potential (ϕ) can still be used to describe velocities.

Stokes expansion: Sir George Gabriel Stokes developed a nonlinear theory describing higher order waves based on a perturbation approach, where ϕ and ζ is expanded in a series (Equation 2.17) and substituted into Equation 2.10, were solutions for ϕ and ζ are obtained by sorting expanded terms and solving the equations. Finding solutions is tedious due to coupling between higher order terms of the expanded quantities, and the derivations are not shown here but can be found in [28].

$$\phi = \sum_{i=0}^{\infty} \epsilon^i \phi_i \qquad \zeta = \sum_{i=0}^{\infty} \epsilon^i \zeta_i \tag{2.17}$$
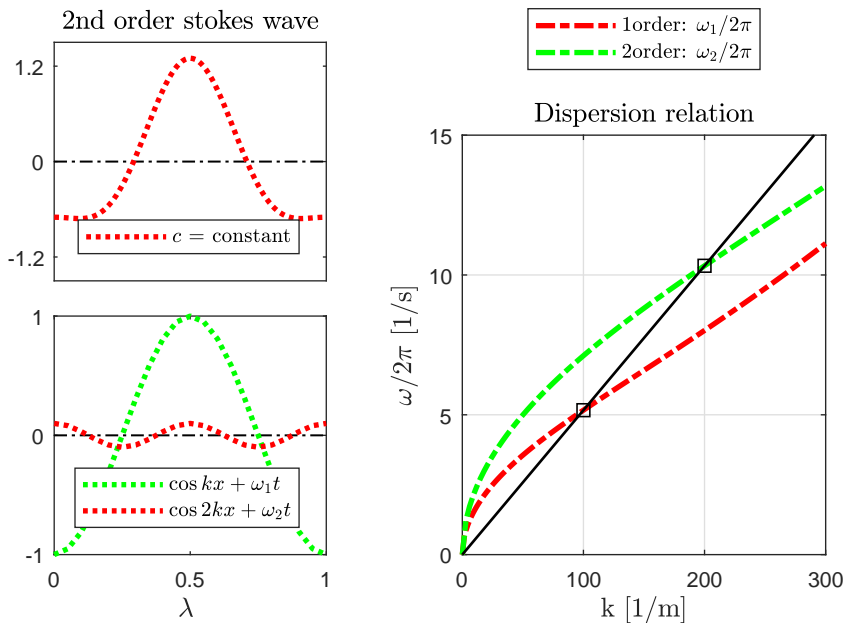

Figure 2.9: Dispersion relation for 2nd order Stoke waves (right) which shows the first and second order harmonic lines and superimposed harmonics (left) propagating with the same phase velocity.

Second order solution at finite depth: Stokes showed that if second order terms are kept in the expanded equations, a solution is found for ζ_1 and ζ_2 where wave harmonics of k and $2k$ propagates at same phase velocity (c), hence form a steeper monochromatic wave as shown in Figure 2.9. The right plot show the dispersion relation for k and $2k$, where the phase velocity, given by the average slope ω/k, intersects at k and $2k$, illustrated by the black line.

$$\zeta(x,t) = a[\cos\theta + ka\frac{3 - \sigma_n^2}{4\sigma_n^3}\cos 2\theta] \tag{2.18a}$$

$$\phi(x,t) = a\frac{\omega}{k}\frac{\cosh k(h+z)}{\sinh hk}\left[\sin\theta + ka\frac{3\cosh 2k(h+z)}{8\sinh^3 kh}\sin 2\theta\right] \tag{2.18b}$$

$$\sigma_n = \tanh kh \qquad \omega_0 = \sqrt{k(g + \frac{\sigma}{\rho}k^2)\sigma_n} \qquad \theta(x,t) = kx - \omega_0 t \tag{2.18c}$$

Equation 2.18 contains the second order solution for ϕ and ζ, for uniform depth h where the linear dispersion relation (ω_0) is still describing the relation between angular velocity and wavenumber.

Third order solution infinite depth: To third order (for deep water waves $kh > \pi$), the dispersion is dependent on the steepness and a correction factor α appears in the dispersion relation (Equation 2.19b), which tends to speed up the wave (positive contribution to the phase velocity). Figure 2.10 show nonlinear dispersion lines plotted for a variety of α.

$$\zeta(x,t) = a\{\cos\theta + \frac{1}{2}(ka)\cos 2\theta + \frac{3}{8}(ka)^2 \cos 3\theta\} \qquad \phi(x,t) = a\frac{\omega}{k}e^{kz}\sin\theta \quad \text{(2.19a)}$$

$$\omega = \omega_0 \alpha \qquad \alpha = \left[1 + \frac{1}{2}(ka)^2\right] \tag{2.19b}$$
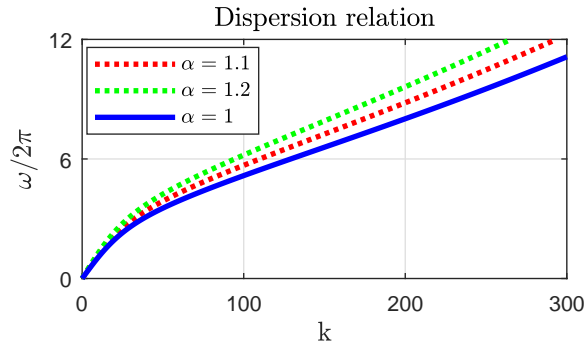

Figure 2.10: Nonlinear dispersion relation for different steepness parameters (ka).

2.4 Wave-current interaction

The main topic of this thesis is to study the interaction between wave dispersion and currents. The theoretical background will be described in this section, which will be used in chapter 6 when shear affected dispersion is measured and related to the velocity profile.
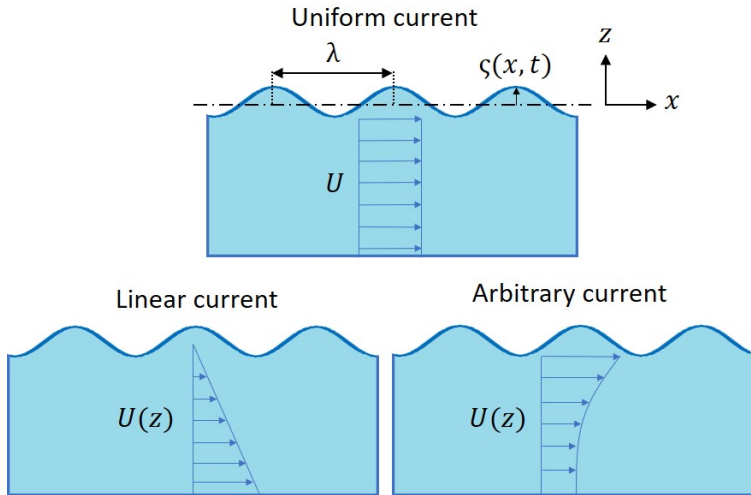

Figure 2.11: Wave-current interaction geometry shown for uniform flow $(U(z) = U)$, linear shear current $(U(z) = -U(z/h))$, and an arbitrary profile $(U(z))$.

Figure 2.11 show the 2D geometries for waves propagating on uniform, linear, and arbitrary sheared currents. The problem formulation with the simple case of a uniform current can still be described with a velocity potential representing the velocity field, hence an extension of the theory described in section 2.2 is enough to includes the effect of a uniform current. However, when the velocity profile is varying with depth and contains shear, the assumption of irrotational flow is invalid. Therefore the problem needs to be formulated from the Euler equations.

Uniform currents:

Waves propagating on a uniform current is similar to the general case described in section 2.2, since the velocity still can be described as a potential field. The only difference is that one of the convective terms has to be kept in Equation 2.20a and Equation 2.20b, since U is not a small quantity, hence the terms can not be neglected when the equations are linearized.

$$\frac{d\zeta}{dt} + U\frac{d\zeta}{dx} = \frac{d\phi}{dz}|_{z=0} \tag{2.20a}$$

$$\frac{\partial\phi}{\partial t}|_{z=0} + U\frac{d\phi}{dx} + g\zeta = \frac{\sigma}{\rho}(\zeta_{xx} + \zeta_{yy}) + \frac{p_{\text{above}}}{\rho} \tag{2.20b}$$

$$\zeta(t,r) = \int \frac{d^2k}{2\pi^2}[C_+e^{i(\omega - Uk_x)t} + C_-e^{-i(\omega + Uk_x)t}]e^{i\mathbf{k}\cdot\mathbf{r}} \tag{2.20c}$$

$$\omega = \omega_0 + Uk_x \qquad c = c_0 + U \tag{2.20d}$$

The solutions are obtained by following the same steps as in section 2.2. The dispersion relation has an extra term related to the uniform current, which can be visualized as a constant Doppler shift of the phase velocity in the $k - c$ plane shown in Figure 2.12. The physical interpretation is equivalent to observing the propagating waves from a moving reference plane, translating with the current.
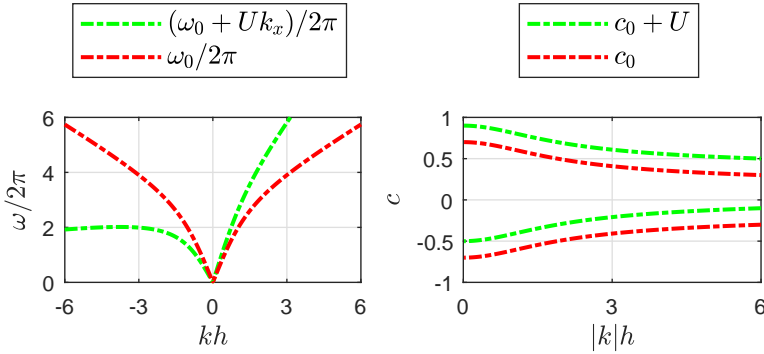

Figure 2.12: Angular and phase velocities for waves propagating on a uniform current when $U = 0$ [m/s] (green lines) and $U = 0.2$ [m/s] (red lines).

- **Doppler shift** (Δc): Waves propagating on uniform currents are affected by wave number independent Doppler shifts ($\Delta c = U$), which is the same as change of reference plane.

Sheared currents:

All the solutions in previous chapters are solved by describing velocities by a potential function, which significantly simplifies the analysis. For waves propagating on depth varying currents, the potential formulation is invalid due to rotational flow, hence the Euler equations are needed to describe velocities and pressure.

Problem formulation: Physical quantities can be split into mean $(\mathbf{U}, P)$, and perturbed quantities $(\hat{\mathbf{u}}, \hat{p})$, where $(\mathbf{U} \ll \hat{\mathbf{u}})$.

$$\mathbf{u} = (U(z) + \hat{u}, \hat{v}, \hat{w}) \qquad p = -\rho g z + \hat{p} \tag{2.21a}$$

$$\frac{D\mathbf{u}}{Dt} = -\frac{1}{\rho}\nabla p \qquad \nabla \cdot \mathbf{u} = 0 \tag{2.21b}$$

The expressions for $((\mathbf{u}, p))$ are substituted into the continuity and Euler equations. After transforming the equations to the frequency domain (Fourier transform) and simplifying one obtains the Rayleigh equation for the vertical velocity $(\hat{w})$ and phase velocity (c) [9].

1. Substitute Equation 2.21a into Equation 2.21b.

2. Linearize by neglecting higher order terms $\hat{u}\hat{v} \approx 0$.

3. Reduce the system by ellinating $(\hat{u}, \hat{v}, \hat{p})$.

$$\left(\delta_z^2 - k^2\right)w = \frac{U(z)''}{\left(U(z) - c\right)}w \tag{2.22a}$$

$$\Delta p = \left(\frac{\sigma}{\rho}k^2\right)\zeta \qquad w|_{z=-h} = 0 \qquad \left(\delta_t + ik_x U(z)\right)\zeta = w \tag{2.22b}$$

In general Equation 2.22 has no closed form solution and assumptions on $U(z)$ are needed to progress further. Equation 2.22a contains singularities at $\left(U(z) - c\right) = 0$ which is called critical layers, where the phase velocity matches the current velocity.

Uniform vorticity: If one assumes a linear current profile with no curvature $(U(z)'' = 0)$, a closed form solution for ω can be obtained (Equation 2.23) by solving Equation 2.22. S. Å. Ellingsen extended the analysis of shear dispersion to 3D, where he studied asymmetric wave patterns such as ship wakes and ring waves [9, 10].

$$\omega_{\pm}/k = -c_1 \pm \sqrt{c_0^2 + c_1^2} \tag{2.23a}$$

$$c_0^2 = \left(\frac{g}{k} + \frac{k\sigma}{\rho}\right) \tanh kh \qquad c_1 = \frac{1}{2} S \tanh (kh) \cos \theta \tag{2.23b}$$

$S = dU/dz$ is the shear parameter, and θ is the angle between $\mathbf{k}$ and $U(z)$. The sheared current results in a Doppler shift (Δc), which is wave-number and angle dependent (Figure 2.13) and asymmetric dispersion leading to asymmetric wave patterns might occur under these conditions.
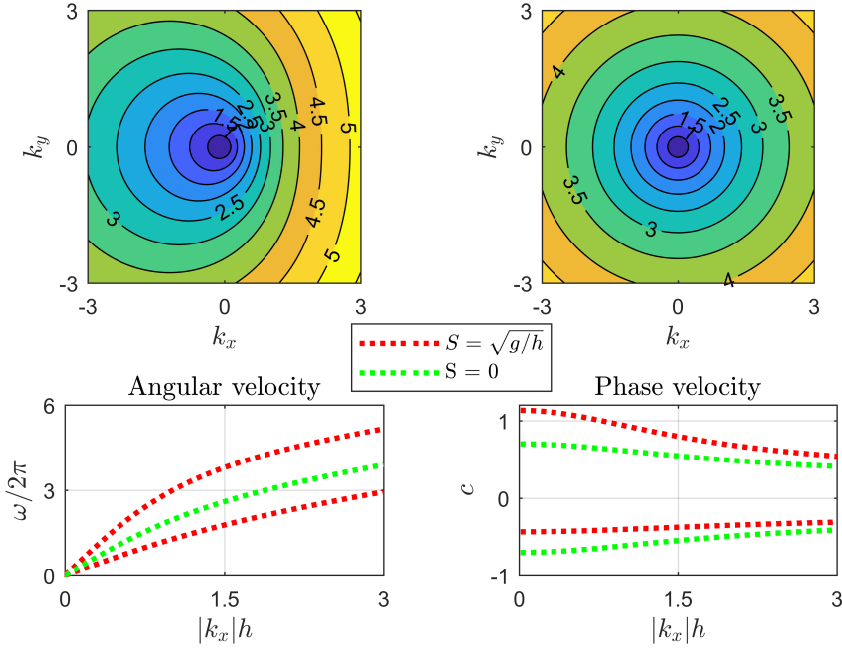

Figure 2.13: Linear shear affected dispersion (red dots) and dispersion in quiescent waters (green dots), shown in the (k_x, k_y) plane in the contour plots.

- **Doppler shift:** Waves propagating on depth varying currents ($U(y)$) results in wave-number dependent Doppler shifts ($\Delta c(k)$), which for a linear profile has an explicit expression.

General profiles and integral relation: In 1989, J T. Kirby and T. M. Chen extended the analysis performed by R. H. Steward and J. W. Joy where the dispersion relation is approximated for linear waves riding on a weak current of arbitrary shape [5, 6]. c_1, which is the depth averaged Doppler shift, is obtained by solving a weighted integral (Equation 2.25) over depth for each wave-number. This integral relation expressed in Equation 2.25 has been extensively used to describe waves propagating on arbitrary currents and in the next section a current inversion formulation will be described where the integral relates the shear affected dispersion and current velocities.

$$c = \sum_{i=0}^{\infty} \epsilon^i c_i \qquad \epsilon \sim U/c \tag{2.24}$$

$$c_1 = \frac{2k}{\sinh 2hk} \int_{-h}^{0} dz \frac{\mathbf{u} \cdot \mathbf{k}}{k} \cosh 2k(h+z) \tag{2.25}$$

The phase velocity is expanded in a series where c_0 is the linear phase velocity, and c_1 approximates the shear affected phase velocity to first order accuracy ($\epsilon(O^1)$ for arbitrary currents, except in a few cases where $U(z)$ is strongly sheared.
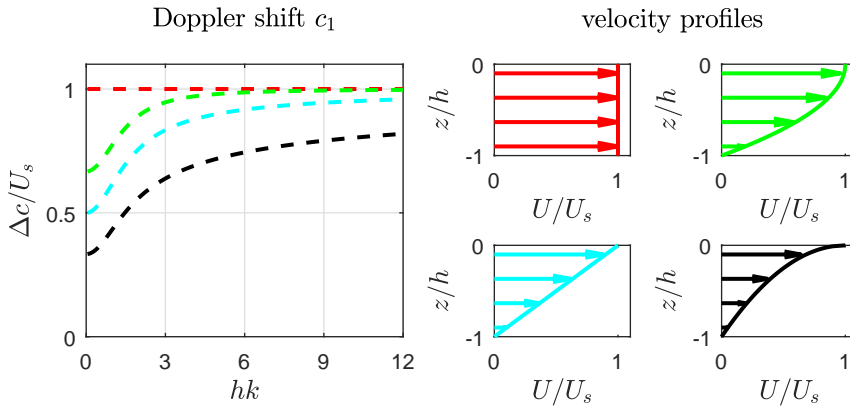

Figure 2.14: Shear affected Doppler shifts (left) and corresponding current profiles(right) denoted by the line color.

- **Depth averaged Doppler shift:** c_1 can be physically viewed as a weighted average Doppler shift obtained by integrating over the depth, where the wave is affected in the region ($z < \lambda/2$) by an exponential reducing factor. Note that Δc is asymptotically reaching the surface current for large kh.

2.5   Current inversion algorithm

In section 2.4 the relationship between propagating waves and subsurface currents are established and for the general case of an arbitrary velocity profile, the Doppler shift velocity can be obtained by solving an integral provided that the velocity profile is known. In this section, the inverse problem will be formulated where one knows the Doppler shifted velocity, hence one must solve an integral equation to obtain the unknown velocity field. The method described in this section will be used in chapter 6 where the velocity profile will be calculated from dispersion data obtained from experimental measurements of the free surface.

Inversion formulation: Measuring velocities close to a free surface with propagating waves atop, by traditional measurement techniques (such as probes or ADCP) is challenging due to waves interfering with the measurements. An alternative approach using the information about wave dispersion and the relation to currents can be used to perform these velocity measurements. By measuring the free surface ($\zeta(x, y, t)$), dispersion data ($\Delta c, \Delta \omega$) can be extracted and related to the Doppler shift velocity c_1 described in section 2.4.

Problem formulation:

1. **Rewrite integral relation as residual:** ϵ_e is the residual between measured, and calculated dispersion data from an assumed velocity profile solving the integral relation.

2. **Minimize residual with respect to velocity:** (ϵ_e) is minimized with a nonlinear solver, where the curvature of $U(z)$ is constrained, forcing the solution to be smooth.

$$\epsilon_e = \frac{1}{N} \sum_{i=1}^{N} (F(k_i, U)k - \Delta \omega_i)^2 \quad F(k, U) = c_1(k, U) \quad U = [U_1, U_2, ...U_n]^T \quad (2.26)$$

$F(k, u)$ is the Doppler shift velocity (Δc) calculated by solving Equation 2.25, while $\Delta \omega$ is the measured dispersion data obtained from experimental analysis of the free surface. U is calculated by minimizing the residual defined in Equation 2.26, using fmincon in Matlab.

Curvature constraint: Curvature (d^2U/dz^2), is constrained to obtain smooth solutions from the inversion. However, over constraining leads to errors while under constraining leads to nonphysical oscillating solutions. One method (implemented here) is to start by fully constraining the problem ($b = 0$) and reduce the constrain ($b > 0$), calculating the residual error (ϵ) for each time. When the residual converges, one obtain the smoothest solution without over constraining the problem (illustrated by the flow chart in Figure 2.15).

$$\left| \frac{d^2U_i}{dz^2} \right| = \frac{1}{\Delta z^2} \left| \begin{bmatrix} 1 & -2 & 1 & 0 \\ 1 & -2 & 1 & \dots \\ & \vdots & \ddots & \\ 0 & 1 & -2 & 1 \end{bmatrix} \begin{bmatrix} U_1 \\ U_2 \\ \vdots \\ U_N \end{bmatrix} \right| < b \qquad (2.27)$$
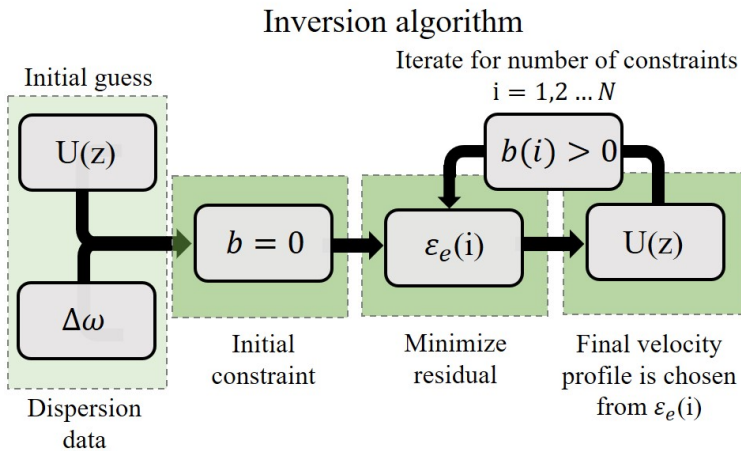

Figure 2.15: Flow chart showing the steps involved in the current inversion algorithm.

The curvature is calculated from U by finite differences (Equation 2.27), which is constrained ($< b$). $U(z)$ is calculated for N number values of b, where the residual ϵ_e is plotted for each iteration (Figure 2.16). The solution is chosen when the residual is stagnating (in this case $i = 8$).

Demonstration on mock data: Figure 2.17 and Figure 2.16 demonstrates the inversion where mock data is generated from a quadratic velocity profile ($U(z) = U_0(1 - (z/h)^2)$), where Δc is calculated (red line). White Gaussian noise is added resulting in noisy data (black crosses), which are used to calculate the velocity from minimizing ϵ_e (green line).
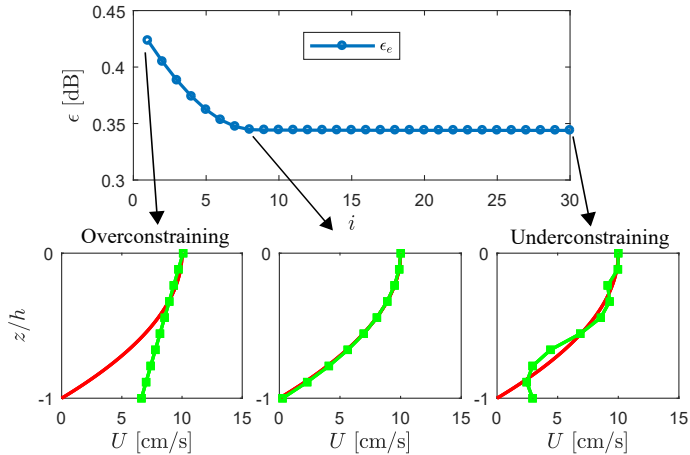

Figure 2.16: Current inversion for different constrain tolerance. Over constraining leads to errors, while under constraining leads to non smooth solutions.
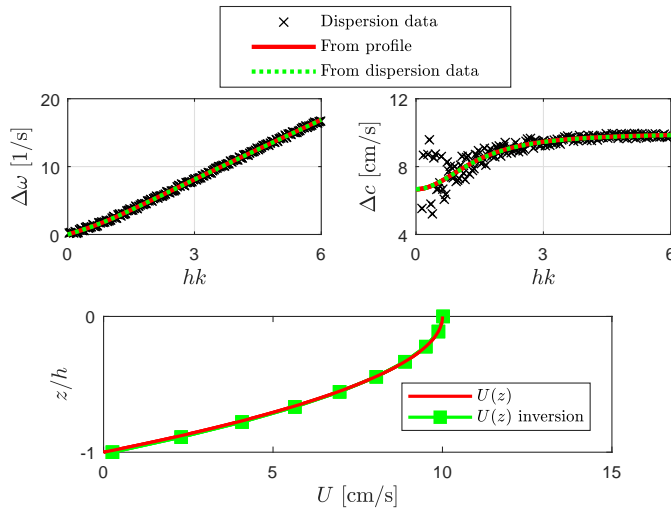

Figure 2.17: Inversion of a polynomial velocity profile. Fit to dispersion data (top) based on minimizing error, and velocity profile (bottom)

2.6 Examples of 3D wave patterns

In chapter 5 and chapter 6 experiments where classical wave patterns are generated by wave-making mechanisms are presented, hence theoretical predictions to compare with the measurements are needed and will be presented in this section.

Initial value description (ζ_0):

Perhaps the simplest example of waves are the formation of linear ring waves in quiescent waters, which might be described by the solutions obtained in section 2.2. The constants in Equation 2.14b and Equation 2.14a are obtained from initial condition ($\zeta(r, 0)$ and $\dot{\zeta}(r, 0)$), and if a Gaussian initial shape is assumed, an explicit expression for the waves can be described as an integral equation (Equation 2.28b) which is solved by numerical integration. Figure 2.18 shows solutions to Equation 2.28b both for gravity and capillaryy waves.

$$\hat{\zeta}(k, 0) = 2\pi\zeta_0 a^2 e^{-ka^2/2} \qquad \dot{\hat{\zeta}}(k, 0) = 0 \tag{2.28a}$$

$$\zeta(r, t) = \zeta_0 a^2 \int_0^\infty k e^{-k^2 a^2/2} J_0(kr) \cos(\omega t) dk \tag{2.28b}$$
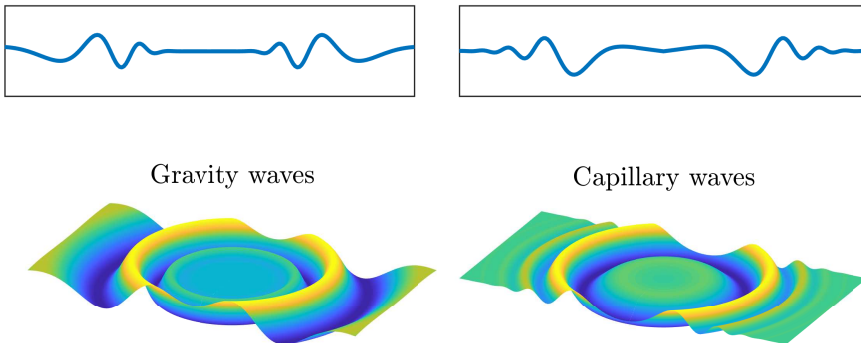

Gravity waves   Capillary waves

Figure 2.18: Linear ring waves from Gaussian initial shape, both for gravity waves (left) and for capillary waves (right)

Free surface defined by the impulse response:

A more general way of describing the problem is by the means of an impulse response, where the free surface ζ is defined by a convolution sum of the system impulse response and an applied disturbance $p_{\text{ext}}(x, y, t)$. From wave theory one can derive the impulse response H_ζ (Equation 2.29a), where the dispersion relation ω is needed to calculate H. In general ω needs to be determines by approximation methods (For instance Kirby and Chens integral method), but for a constant shear current where the closed form solution exists (Equation 2.23) one can calculate H without approximations. A detailed formulation and derivation of Equation 2.29can be found in the following reference [30].

$$\zeta(\mathbf{k}, t) = \int_{-\infty}^{t} d\tau p_{\text{ext}}(\mathbf{k}, \tau) H_\zeta(\mathbf{k}, t - \tau) \tag{2.29a}$$

$$H_\zeta = \frac{ikF(\mathbf{k})}{2\rho\omega_{\text{div}}}(e^{-i\omega_- t} - e^{-i\omega_+ t}) \qquad F(\mathbf{k}) = \frac{k\widetilde{\omega}^2}{gk^2 - \mathbf{k} \cdot \mathbf{U_0'}\widetilde{\omega}} \tag{2.29b}$$

$$\widetilde{\omega} = \omega - \mathbf{U_0} \qquad \omega_{\text{div}} = 1/2(\omega_+ - \omega_-) \tag{2.29c}$$

Single impulse resulting in ring waves:

In the case of one single impulse response appearing at $t = 0$, the convolution becomes a single multiplication $p_{\text{ext}}(\mathbf{k}, 0)H_\zeta(\mathbf{k}, t)$, which is solved by a Fast Fourier Transform (FFT) implementation. By simply setting $S = 0$ both shear affected and shear unaffected dispersion can be illustrated by the same code, which is shown in Figure 2.20 and Figure 2.19. Scales for dimensionless time (T), shear (Frs), and space ($x/a, y/a$) are used to generalize the plots. A Gaussian pressure defined by Equation 2.30a is applied at $T = 0$ and the axis are scaled by the half width a of the applied pressure, showing the time development of waves both for Frs= 1 and Frs= 0.

$$p_{\text{exp}} = Ae^{-\pi^2(x^2+y^2)/a^2} \tag{2.30a}$$

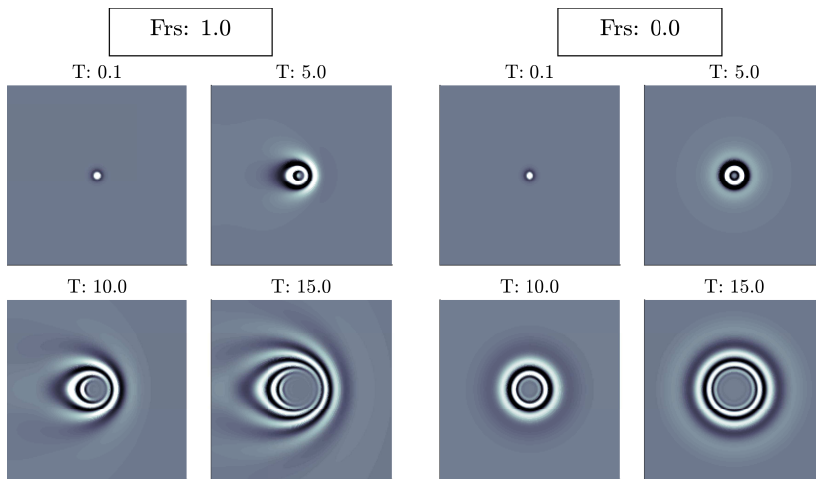$$\text{Frs} = S\sqrt{a/g} \qquad T = t\sqrt{g/a} \tag{2.30b}$$

Figure 2.19: Snapshots of ring waves at different time instances (T) both for waves propagating on a linear current (left) and no current (right)
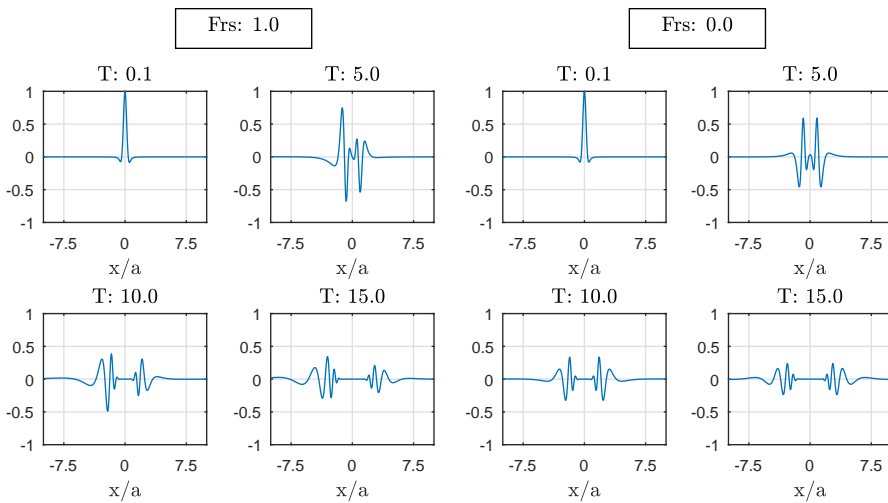

Figure 2.20: Snapshots of ring waves at different time instances (T) both for waves propagating on a linear current (left) and no current (right) plotted along the center line (x/a, 0)

Figure 2.20 shows normalized amplitude,$\zeta(y = 0, x/a, t)/\zeta_0$ plotted along the center line $y = 0$ where waves propagating left is shear assisted, while waves propagating right is shear anhibited. For Frs $\neq 0$, shear dispersion results in asymmetrical ring wave patterns.

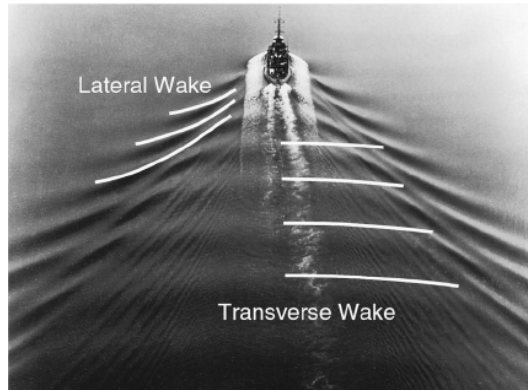**Series of impulses resulting in ship waves - the Kelvin wake:**

Figure 2.21: Kelvin wake pattern behind a ship. The ship generates transverse and lateral wake patterns which is stationary relative to the ship motion [2].

By choosing a coordinate system $(x' + U_x t, y' = y + U_y t)$, which translates along a moving pressure source, starting at $t = 0$ and integrating the impulse response in time from 0 to t (time convolution), gives the time evolution of waves generated by a pressure source set to motion at $t = 0$. When t becomes sufficiently large the surface pattern becomes stationary in the reference frame of the moving source and a fully developed wake pattern is obtained. The effect of shear dispersion is modeled by calculating the dispersion relation (ω) relative to the coordinate axes (x', y').

$$p_{\text{ext}}(x, y, t) = p_{\text{ext}}(x + U_x t, y + U_y t) \tag{2.31a}$$

$$\text{Fr} = \frac{|U|}{\sqrt{ga}} \qquad \text{Frs} = \frac{|U|S}{g} \qquad \text{Frh} = \frac{|U|}{\sqrt{gh}} \tag{2.31b}$$

---

[2]`https://www.researchgate.net/profile/John_Goree/publication/`
`8952800/figure/fig1/AS:280204204363778@1443817296965/`
`FIG-1-A-Kelvin-wedge-behind-a-ship-moving-in-deep-water-consists-of-multiple-lateral.`
`png`

Scaling and transient ship wakes: The Fr number is the fraction between the velocity scale of the source and the velocity scale of the waves, which determines the relative importance of the lateral or transverse wake. Frs and Frh are scales for shear and depth, which determines the importance of shear dispersion and bottom effects. Figure 2.22 show the time evolution a moving Gaussian pressure source, which becomes stationary in the relative reference frame (x', y').
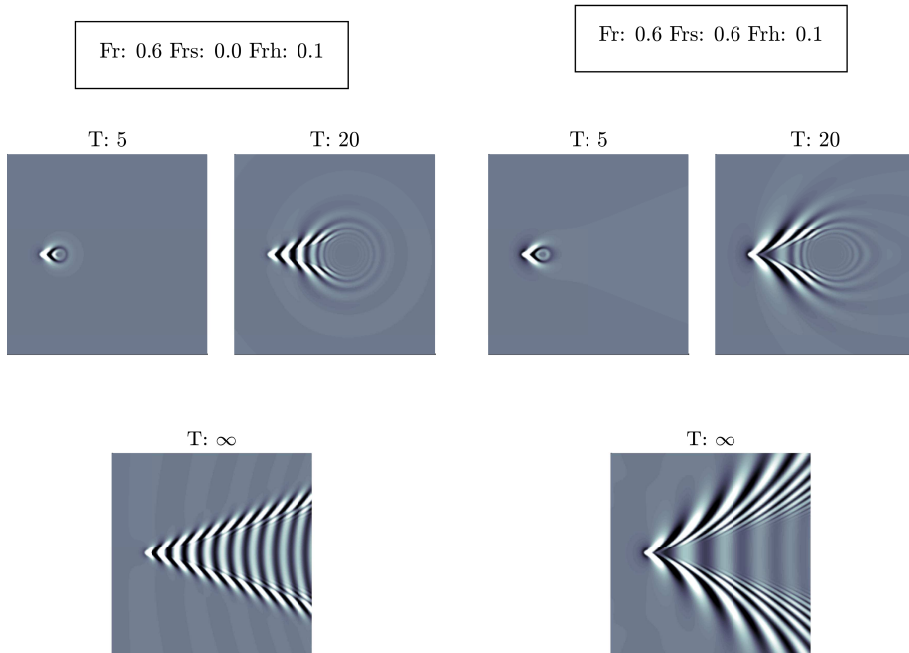
Fr: 0.6 Frs: 0.0 Frh: 0.1

Fr: 0.6 Frs: 0.6 Frh: 0.1

T: 5   T: 20   T: 5   T: 20

T: ∞ T: ∞

Figure 2.22: Time development of moving pressure source. After sufficient time T, the wake pattern becomes stationary relative to the moving reference plane.

Steady ship patterns: Figure 2.23 shows kelvin patterns for a variety of scaling parameters Fr,Frs, where Frh$\approx$ 0. $\zeta(x, y, t = \infty)$ is obtained by solving the convolution in Equation 2.29a until the pattern becomes stationary for a Gaussian pressure impulse. Fr determines if the lateral or transverse wake will dominate, while Frs determines the effect of shear, which for Frs $\neq$ 0 and $\theta \neq (0, 180)$ becomes results in asymmetrical wake patterns if the relative angle between the moving source and the current differs from 0 or 180.
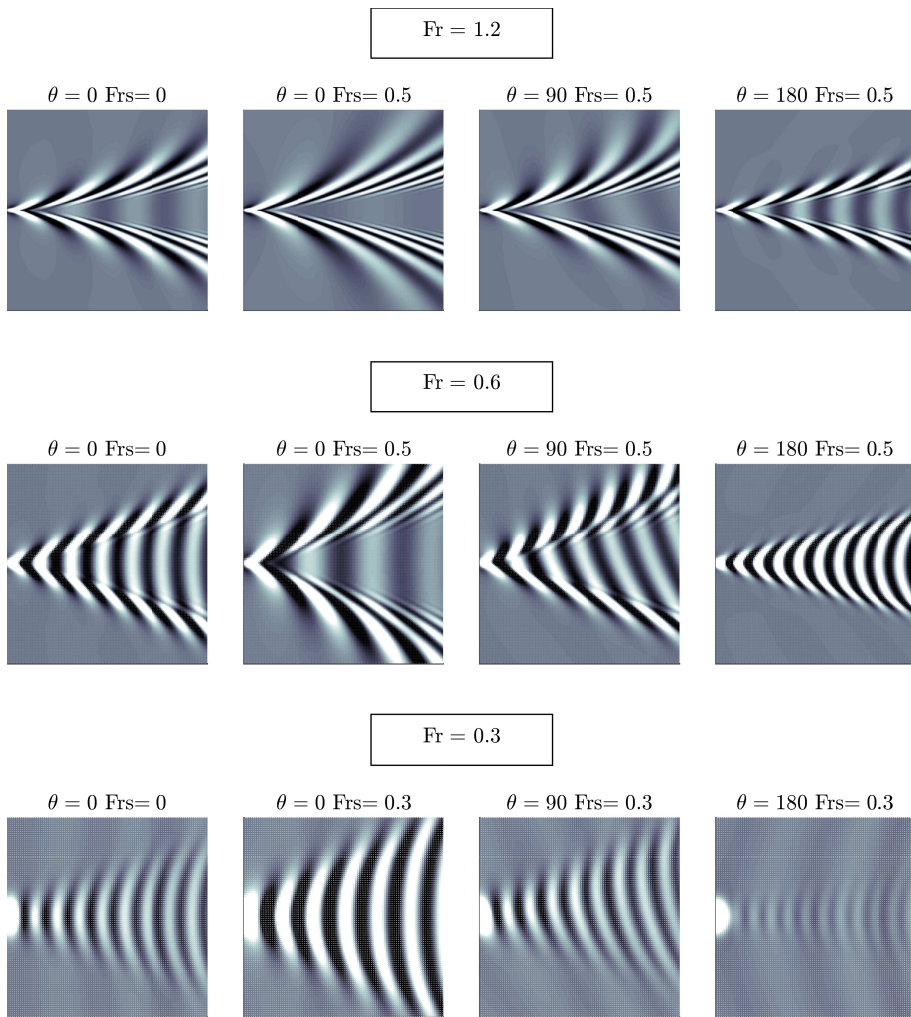
Figure 2.23: kelvin wake patterns for different flow regimes (Fr,Frs,Frh=0).

Chapter 3

Experimental methods

In this section a selection of experimental methods implemented in chapter 4 and used in chapter 5 and chapter 6 are introduced and explained in detail, where the mathematical descriptions of the signal processing are provided.

1. **Surface topology measurements:**

   (a) **Fourier Transform Profilometry (FTP):** Optical method to measure topology of a surface by analyzing the reflection of a periodic fringe pattern on the free surface.

   (b) **Free Surface Synthetic Schliren(FS-SS):** Optical method to measure the surface gradient of a transparent fluid by analyzing a refracted schlieren pattern visualized through the free surface.

2. **Velocity measurements:**

   (a) **Particle Image Velocimetry (PIV):** Optical method to measure fluid velocities by measuring the movement of tracer particles seeded in the fluid.

3. **Wave generation:**

   (a) **Pneumatic wave-maker:** Pneumatic jet imposing stagnation pressure on the free surface generating waves.

   (b) **Mechanical wave-maker:** Translating plate displaces fluid, driving it into wave motion.

4. **Shear flow generation:**

   (a) **Flow through selected obstacles:** Flow directed through a curved mesh, non uniformly spaced rods, or depth varying honeycombs to generate a depth varying pressure gradient, deflecting streamlines, hence generate velocity gradients.

Symbols used in Fourier Transform Profilometry

L	Projector reference length	φ	Image phase shift
D	Projector camera length	Φ	Normalized phase shift
P	Gray scale pattern length	α	Optical parameter
h	Surface height	λ	Wavelength
I	Gray scale intensity	k	Wave-number
C	Constant	g	Gaussian filter
(x, y)	Image coordinates	d	Filter width
(x', y')	Shifted image coordinates	δ	Delta function

Symbols used in Free Surface Syntethic schlieren

∇h	Surface gradient	$h*$	Optical depth
Δr	Image strain	α	optical parameter
n	Refractive index	I	Image gray scale intensity
L	Length Schlieren pattern	β	Contrast threshold
H	Camera water distance	t	Time
h	Surface height	τ	Time
h_0	Water depth	C	Cross-correlation
h_g	Thickness Perplex plate	(f, g)	Functions
h_p	Effective depth	p_{pitch}	Pixel pitch

Symbols used in Particle Image Velocimetry

U	Velocity	u_p	Particle velocity
$\mathbf{u}$	Velocity	u_f	Fluid free stream velocity
Δr	Image strain	μ_c	Fluid dynamic viscosity
t	Time	f_{drag}	Particle drag force
Δt	Time separation	A_p	Particle surface area
I	Image gray scale intensity	C_d	Particle drag coefficient
H	Camera water distance	τ_v	Particle response time
ρ_p	Particle density	C	Cross correlation
d_p	Particle diameter	p_{pitch}	Pixel pitch
V_p	Particle volume		

Symbols used in Wave generation

L	Nozzle free surface length	κ	Heat capacity ratio
b	Jet half width	C_v	Specific heat capacity constant volume
u	Jet velocity		
u_{mean}	Mean outlet jet velocity	C_p	Specific heat capacity constant pressure
U_{max}	Max jet velocity		
J	Jet momentum	c	Speed of sound
ρ	Fluid density	T	Air Temperature
ρ	Fluid density	H	Wave height from wave-maker
$A*$	Surface area Nozzle	S	Stroke length wave-maker
Δt	Time separation	k_p	Wave-maker wave-number
C_d	Nozzle drag coefficient	h	Water depth

3.1 Fourier Transform profilometry

Fourier Transform Profilometry (FTP) is an optical technique used to measure the surface of an object by analyzing the phase deformation of a periodic fringe pattern due to change of reflection surface (h). Optical relations relates the phase shift $(\Delta\varphi)$ of the reflected image to the change in surface height (h). The phase characteristics are extracted by Fourier analysis and through optical relations, the shape of the deformed surface h can be reconstructed. The technique was first developed by M. Takeda and K. Mutoh to measure topography of 3D objects [11], and has been extended by P. Cobelli, A. Maurel, V. Pagneux and P. Peititjeans to measure liquid surface topology [12, 13, 14].
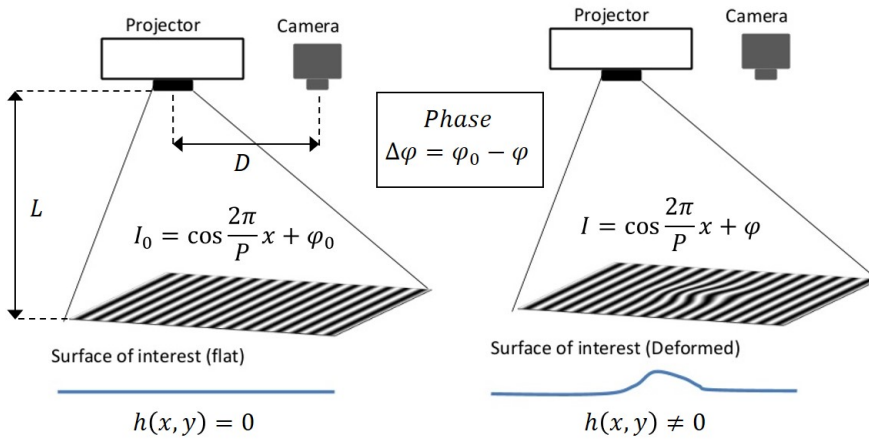
Figure 3.1: Coaxial setup for Fourier Transform Profilometry, where $h(x, y)$ is proportional to a phase shift $\Delta\varphi$, which is extracted by Fourier analysis.

The technique is to project a periodic fringe pattern on a reference surface, where images are obtained by a camera mounted coaxial to the projector (Figure 3.1). The pattern is viewed by the camera due to diffuse reflection on the surface topology resulting in a phase shifted fringe pattern compared to a flat reference where the pattern is viewed as a sinusoidal gray scale image.
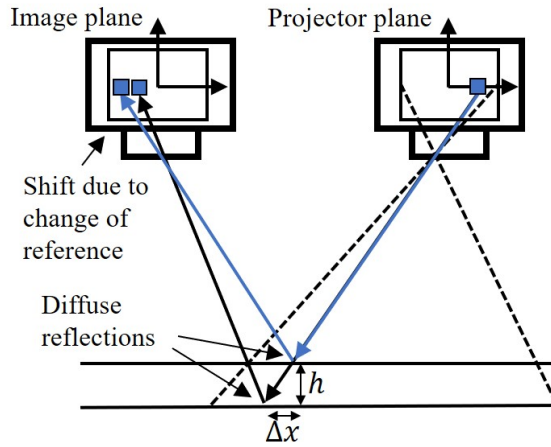
Figure 3.2: Ray geometry for coaxial FTP. The same position in the projector plane is shifted due to change of reflection surface.

A projected pixel in the projector plane, will be shifted due to a change of reflection surface, hence the same pixel will be shifted in the camera plane as seen in Figure 3.2. By choosing the projected image to be a periodic fringe pattern, one obtains a favorable mathematical description, where phase information can be extracted from the images by spectral analysis.

Procedure: The procedure implemented in this thesis is listed below and shown in Figure 3.3.

1. **Imaging:** I_0 and I is obtained from images, where I_0 is from a known reference.

2. **Signal processing:** $\Delta\varphi$ is extracted by analyzing I_0 and I.

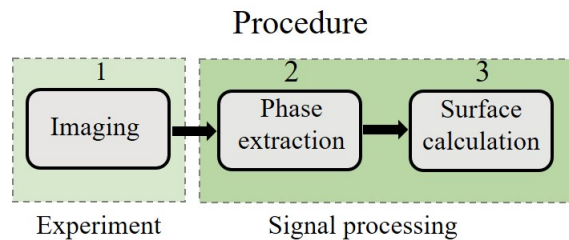3. **Surface reconstruction:** h is related to $\Delta\varphi$ through geometrical optical relations.

Figure 3.3: Procedure for FTP.

3.1.1   Optical relations for coaxial FTP

Optical relations shown Equation 3.1, are used to calculate the surface height from phase characteristics extracted from images. The relations are obtained by optical trigonometry where ray tracing leads to shifts in the camera plane. A full derivation can be found in the following reference [13].

$$h(x', y') = \frac{\Delta\varphi(x, y)L}{\Delta\varphi(x, y) - \frac{2\pi D}{P}} \tag{3.1a}$$

$$x' = \left(1 - \frac{h(x', y')}{L}\right)x \qquad y' = \left(1 - \frac{h(x', y')}{L}\right)y \tag{3.1b}$$

$\Delta\varphi(x, y) = \varphi_0(x, y) - \varphi(x, y)$ represents the phase difference between the I_0 and I. L and D are the physical lengths, where L is the distance from the reference surface to the optical devices, while D is the distance between the camera and projector. P is the wavelength of the projected fringe pattern.

Interpolation to image coordinates: h is calculated in shifted coordinates (x', y') due to optical effects (Δx in Figure 3.2). Therefore, $h(x', y')$ needs to be interpolated to $h(x, y)$ to correct for spatial distortion.

Further study of relations: The optical relation can be rewritten as Equation 3.2, where $\Phi = (P\Delta\varphi)/(2\pi)$ and $\alpha = L/D$. For a setup both α and D will be constant, and Φ is the phase shift scaled to physical dimensions, which is convenient since the optical relation becomes independent of P and can be used to do simple scaling analysis.

$$\Phi = (P\Delta\varphi)/(2\pi) \qquad \alpha = L/D \tag{3.2a}$$

$$h(\Phi) = \alpha\frac{\Phi}{(\Phi/D) - 1} \qquad x'_i = \left(1 - \frac{(\Phi/D)}{(\Phi/D) - 1}\right)x_i \tag{3.2b}$$

The Taylor expansion of Equation 3.2b can be expressed as Equation 3.3, which becomes approximately linear for in the limit $\Phi/D \ll 1$ seen in Figure 3.4.

$$h(\Phi) = h(0) + \sum_{n=1}^{\infty} \frac{d^n h(0)}{d\Phi^n}\frac{1}{n!}\Phi^n = -\alpha\Phi\left[1 + \sum_{n=2}^{\infty} (-1)^n \left(\frac{\Phi}{D}\right)^n\right] \tag{3.3}$$
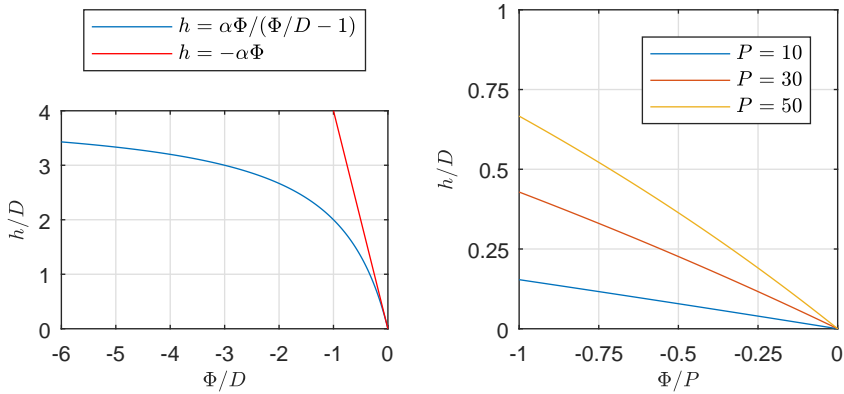
Figure 3.4: Optical relation curves for FTP ($L = 1000, D = 250, \alpha = 4$). Full range normalized by D (left) and range normalized by P (right), where $\Phi/P < -1$ indicates discontinuous phase characteristics.

Design conditions: Depending on size characteristics of the objects desired to measure, the parameters (L, D, P) are designed to obtain desired phase characteristics, where the criterias below are met.

- **Domain size:** L must be large enough for the projected pattern to cover the domain of interest.

- **Shape size:** $P < \lambda_{min}$ is chosen such that shapes of wavelength λ_{min} can be measured (not filtered out in the signal processing).

- **Sensitivity:** D and P is chosen such that $\Delta\phi < 2\pi$ is in the range h for the object.

3.1.2 Spectral analysis by Fast Fourier Transform

When analyzing periodic signals, it is favorable to work in the frequency domain, where operations such as convolution and cross correlation becomes multiplications and spatial filtering is easy to implement. Fourier analysis is a key part of FTP, where the convolution theorem is exploited to extract phase information from the obtained gray scale images.
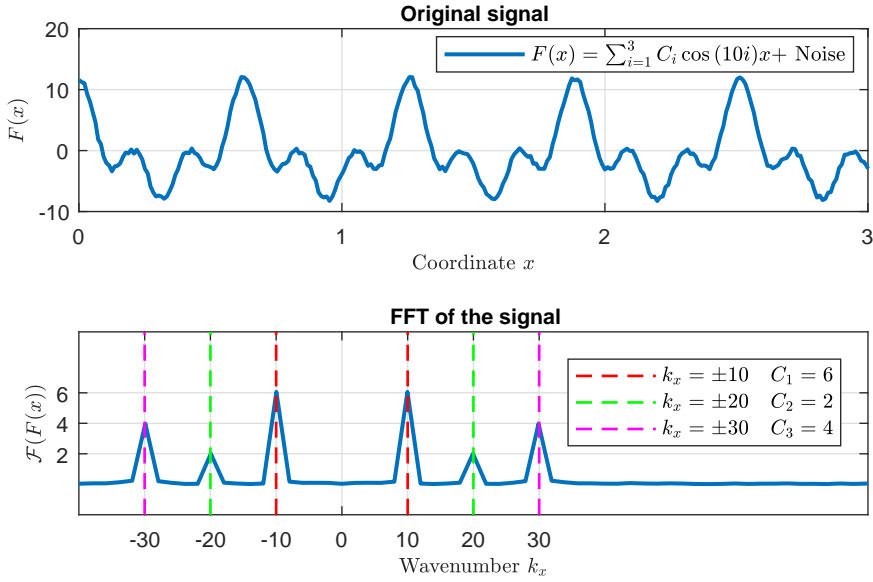

Figure 3.5: A signal and its spectral magnitude computed by a Fast Fourier Transform (FFT) implementation.

Spectral magnitude: Figure 3.5 shows spectral magnitude of F where Discrete Time Fourier Transform (DTFT) (Equation 3.4) is calculated. Fast Fourier Transform (FFT) is an implementation where symmetry and periodicity is exploited to perform this sum faster. The advantage of Fast Fourier Transform (FFT) is that the number of computation is reduced from N^2 to $N \log N$, which makes operations like convolution, cross-correlation and linear filtering for large data much more efficient, which will be exploited in this thesis. In general, the signal can be of multiple variables and be represented both in time and space (x, y, t).

$$X_k = \sum_{n=0}^{N-1} x_n e^{-i2\pi kn/N} \qquad k = 0, \ldots, N-1. \tag{3.4}$$

$x_0, \ldots, x_{N-1}$ contains the signal in discrete points and the algorithm calculates X_k, which is a complex number describing modulus and phase of X.

3.1.3 Signal processing algorithm

Phase extraction algorithm: The phase characteristics $(\Delta\varphi)$ is extracted by the use of spectral analysis of the images (I_0, I) described in this section. Thereafter, $h(x, y)$ is calculated and interpolated to image coordinates. A flowchart of the procedure is shown in Figure 3.6.

1. **Fast Fourier Transform:** FFT is used to transform the images to spectral domain, $I(x, y) \Rightarrow I(k_x, k_y)$.

2. **Filter:** A Gaussian filter centered on $2\pi/p$ is multiplied (convolution in real space) to remove signal convoluted with the negative wave-number $-2\pi/p$

3. **Inverse Fast Fourier Transform:** IFFT is used to transforms the filtered signal back to spatial domain.

4. **Phase extraction** The phase characteristic is extracted from the filtered signal $\Delta\varphi(x, y) = \arg\left(\frac{I_0}{I}\right)$.

5. **Surface calculation:** $h(x', y')$, x', y' is calculated from the optical relations.

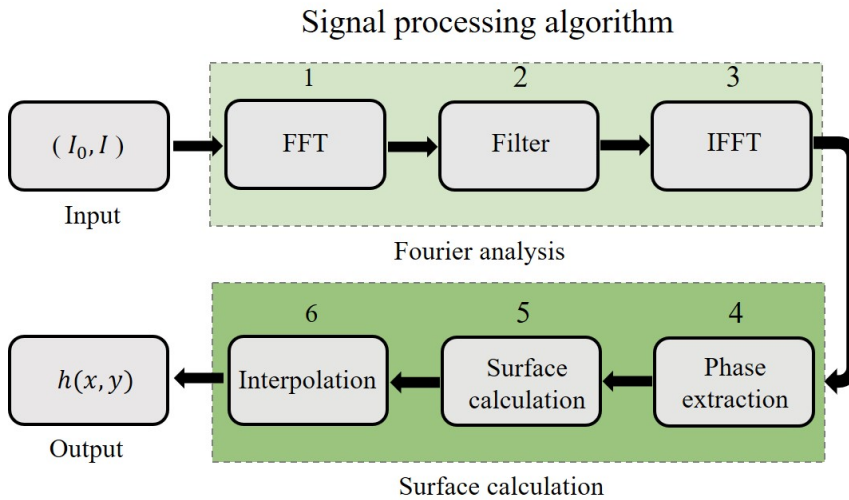6. **Interpolation:** $h(x', y')$ is interpolated to $h(x, y)$.

Figure 3.6: Signal processing algorithm.

Mathematical description:

$$I_i(x, y) = C + \cos\left(\frac{2\pi}{p}x + \varphi(x, y)\right) \tag{3.5}$$

Complex exponentials: The periodic part of Equation 3.5 (measured signals) is written as a sum of two complex exponentials, where i can be either 0 (reference) or 1 (deformed image).

$$I_i(x, y) = C + e^{i(k_p x + \varphi(x,y))} + e^{-i(k_p x + \varphi(x,y))} \tag{3.6}$$

Convolution theorem: A multiplication in in real space is a convolution in the frequency domain. $\delta(\mathbf{k})$ is the delta function, which is the Fourier transform of a constant function, while $\delta(k - k_p)$ is the transform of a linear exponential and $\mathcal{F}$ is the Fourier transform of a general function. $\varphi(x, y)$ is convoluted around $k = \pm k_p$ and the constant intensity is centered on $k = 0$ as seen in Figure 3.7.

$$I(\mathbf{k}) = \delta(\mathbf{k}) + \mathcal{F}(e^{i\varphi(x,y)}) * \delta(k - k_p) + \mathcal{F}(e^{-i\varphi(x,y)}) * \delta(k + k_p) \tag{3.7a}$$

$$g(k) = e^{((k_p - k)^2/(2\sigma^2))^n} \tag{3.7b}$$

Filtering: The first and third term in Equation 3.7a is removed by multiplying a Gaussian filter centered on $k = k_p$ with $I(\mathbf{k})$. A parameter d is defined to scale the filter width σ, as a fraction of k_p. Figure 3.7 shows a graphic representation of the filter process (in 1D for simplicity). Wavelengths shorter than $k_p d$ will be removed from $\Delta\varphi$, hence some information is lost in this process if $\Delta\varphi$ contains signal of higher frequencies.

$$I_{\text{filt}}(k) \approx \mathcal{F}(e^{i\varphi(x,y)}) * \delta(k - k_p) \qquad I_{\text{filt}}(x, y) \approx e^{i(k_p x + \varphi(x,y))} \tag{3.8}$$

The filter procedure is performed both on the reference and the deformed image and the phase map $(\Delta\varphi(x, y))$ is extracted from Equation 3.9.

$$\frac{I_{0\text{filt}}(x, y)}{I_{\text{filt}}(x, y)} = e^{i(\varphi_0(x,y) - \varphi(x,y))} \Leftrightarrow e^{i\Delta\varphi(x,y)} \Rightarrow \Delta\varphi(x, y) = \arg\left(\frac{I_0}{I}\right) \tag{3.9}$$

Compact notation: In Matlab all the above steps are combined in one expression and implemented as Equation 3.10, which is calculated using Fast Fourier Transform (FFT).

$$\Delta\varphi(x, y) = \arg\left(\frac{\mathcal{F}^{-1}(\mathcal{F}(I_0)g)}{\mathcal{F}^{-1}(\mathcal{F}(I)g)}\right) \tag{3.10}$$
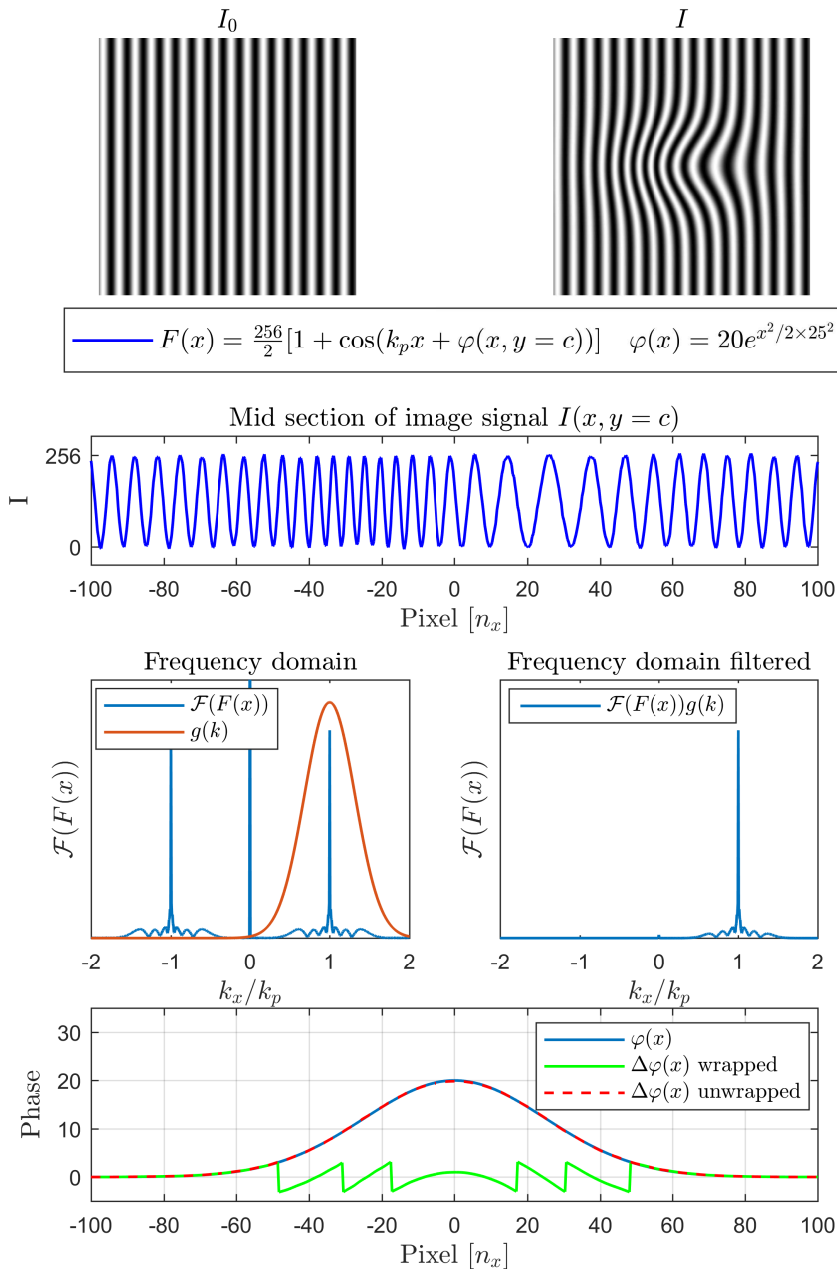
Figure 3.7: Filtering process in FTP. The top images shows typical gray scale signals from the camera. To illustrate the signal processing, the below steps are demonstrated on a 2D strip taken from the mid section of I and I_0, where the two mid images show the Gaussian filtering process and the bottom image show the extracted phase $\Delta\varphi(x)$, before and after phase unwrapping.

Phase jumps and phase unwrapping: If $\Delta\varphi$ exceeds 2π (corresponding to $\Phi/P < -1$), $\Delta\varphi(x, y)$ will contain discontinuous jumps and phase unwrapping is necessary to obtain a continuous surface profile. Figure 3.8 shows an image pair where the phase map contains several discontinuities. FTP is performed on a coffee filter taped to the wall, where the top images show the signal obtained from imaging, and the bottom images shows the reconstructed height without phase unwrapping, hence h is discontinuous.
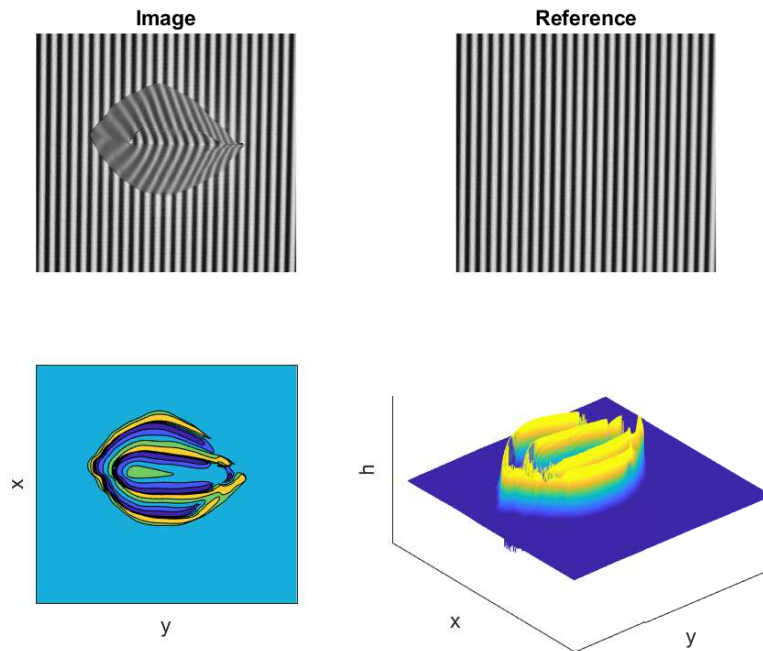
Figure 3.8: FTP performed on topology of a standing coffee filter.

Interpolation: When $\Delta\varphi$ has been extracted, $h(x', y')$, x' and y' is calculated from the optical relations (Equation 3.1) and $h(x', y')$ is interpolated to image coordinates $h(x, y)$ to correct for spatial distortion.

3.2 Free surface synthetic schliren

Free surface synthetic schliren (FS-SS) is an optical method used to measure surface gradients by analyzing refraction of an image visualized through the free surface. A random dot pattern is printed out and visualized through a transparent perplex plate and a camera is mounted above as seen in Figure 3.9. Due to refraction, the dots will be displaced by Δr, proportional to the surface gradient ∇h, which is calculated from Digital Image Correlation (DIC) of the images captured by the camera. The refracted dot pattern due to a Gaussian shaped surface can be seen in Figure 3.10. $h(x, y)$ can be extracted by a least square inversion technique, where ∇h is discretized by finite differences, resulting in a system of equations for h. The techniques was developed by F. Moisy, M. Rabaud, and K. Salsac, who used it to measure water surface topology [23]
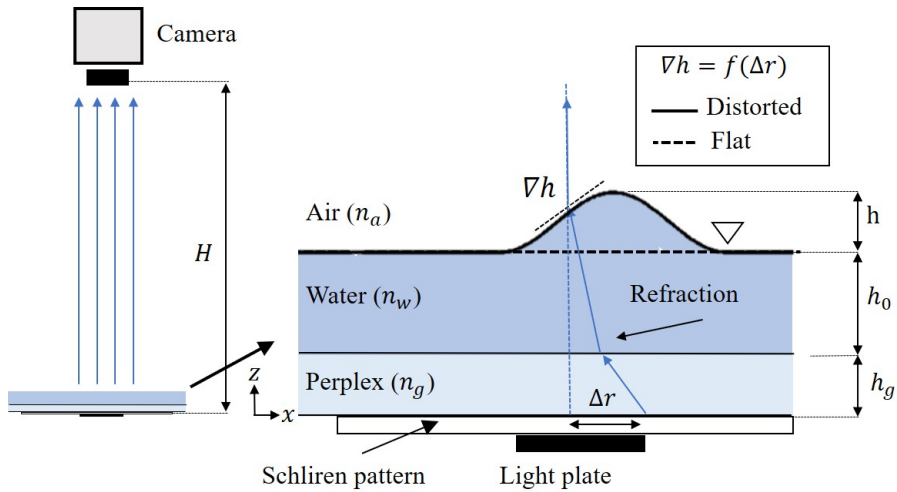

Figure 3.9: principle of Free surface synthetic schlieren. When the surface is deformed, the schlieren pattern will appear distorted, due to refraction at the interface $h(x, y)$, which is proportional to the surface gradient ∇h.
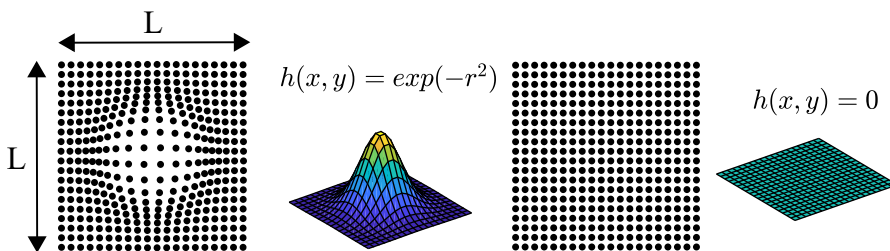

Figure 3.10: Refracted dot pattern, due to a Gaussian surface profile(left) and a flat reference surface (right)

Procedure: The method is to record images of the refracted dot pattern as it deforms in time. A Digital Image Correlation (DIC) algorithms is used to extract local displacement in sub regions of the recorded images, which are related to the surface gradient. The surface topology is reconstructed by solving a system of equation for h obtained by discretizing the gradient field by finite differences.

1. **Imaging:** Record refracted images ($I(x, y, t)$) by camera.

2. **Pre-processing:** Pre-process images to enhance Digital Image Correlation.

3. **Digital Image Correlation (DIC):** Movement of dots (Δr) are calculated by Digital Image Correlation.

4. **Gradient calculation:** Surface gradient field is calculated by optical relations ($\nabla h = f(\Delta r)$).

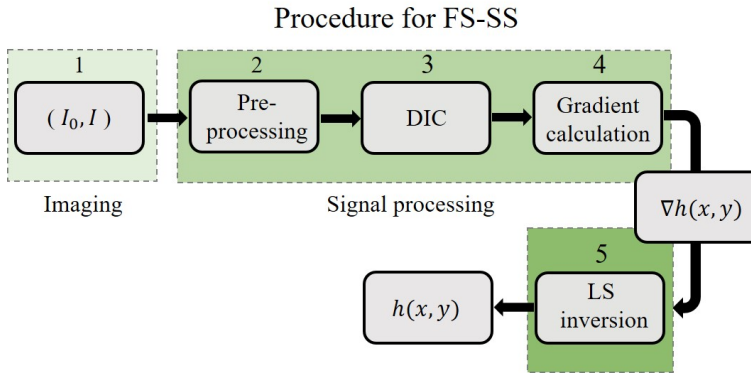5. **Least Square Inversion:** Surface topography (h) is calculated by solving a linear system of equations by discretizing ∇h.

Figure 3.11: Flow chart for the procedure of Free Surface Synthetic Schlieren.

3.2.1 Optical relations for FS-SS

Equation 3.11 relates the surface gradient (∇h) to the deformation (Δr) of the dot pattern. n is the refractive index of different mediums (air, water, plexiglas), and h_p is an effective distance taking additional layers into account in h^*. The relations are derived by using Snell's law and ray tracing, and further details about assumptions and derivations can be found in the following reference [23].

$$\nabla h = -\frac{\Delta r}{h^*} \qquad \frac{1}{h^*} = \frac{1}{\alpha h_p} - \frac{1}{H} \tag{3.11a}$$

$$h_p = h_0 + \frac{n_a}{n_g} h_g \qquad \alpha = 1 - \frac{n_a}{n_w} \tag{3.11b}$$

Approximations: There are three assumptions and approximations restricting the use of the optical relations.

1. **Paraxial approximation:** The pattern-camera distance H has to be much larger than the field size L.
   Criterea: $L/(\sqrt{2}H) \ll 1$.

2. **Weak Slope Approximation:** The method is only able to measure small angles due to a weak slope approximation in the derivation of the optical relation.
   Criterea: $\nabla h \ll \pi/2$

3. **Weak amplitude approximation:** The amplitude has to be small compared to h_p.
   Criterea: $h/h_p \ll 1$.

3.2.2 Pre-processing

The recorded images can suffer from defects such as uneven lighting, low contrast and out of focus, resulting in spurious strain vectors calculated from Digital Image Correlation (DIC). To compensate for these effects, pre-processing algorithms can be implemented to improve the quality of data obtained from images, which is demonstrated in Figure 3.12.

- **High Pass Filtering (HPF):** Compensates for low frequency intensity variation caused by uneven background lighting by filtering out low frequency components of the signal.

- **Intensity Capping (ICap):** Smooths the signal by reducing all intensities above a threshold ($I > I_{\text{threshold}}$) to threshold intensity ($I_{\text{threshold}}$), which reduced bright spots appearing in the signal.

- **Intensity Contrasting (ICon):** Adds contrast by multiplying all intensities above a threshold ($I > I_{\text{threshold}}$) by $1 + \beta$ and below ($I < I_{\text{threshold}}$) by $1 - \beta$, where β determines the magnitude of contrast.
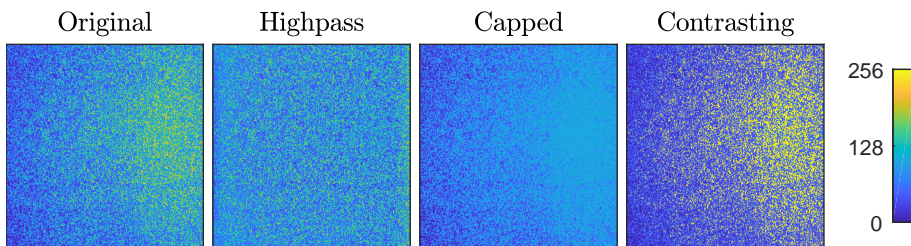

Figure 3.12: Pre processing. Original image (left) contains uneven lighting and three methods are used to pre process the image, where high pass filtering reduces the low frequency intensity variation.

3.2.3 Digital Image Correlation

Digital image correlation (DIC) is a pattern recognition technique used in many optical methods to find patterns in images, where the pattern (strain) can represent deformation, velocity, density difference etc. In section 3.3 an almost identical algorithm is implemented to measure particle shifts in images representing velocities.

Cross-correlation: The image is divided into interrogation widows, where a cross-correlation is calculated and the peak position of $\max(f \star g)$ represents the displacement vector $\Delta \mathbf{r}$. Cross-correlation (defined in Equation 3.12a) is a measure of similarity of two functions relative to each other, where the position of the maximum value determines the best fit.

$$(f \star g)(\tau) \stackrel{\text{def}}{=} \int_{-\infty}^{\infty} f^*(t)\, g(t+\tau)\, dt, \tag{3.12a}$$

$$(f \star g) = \mathcal{F}^{-1}\big[F^*(k)G(k)\big] \tag{3.12b}$$

Figure 3.13 show cross correlation calculated on a delayed Gaussian signal, where the peak of $f \star g$ determines the delay of g relative to f.
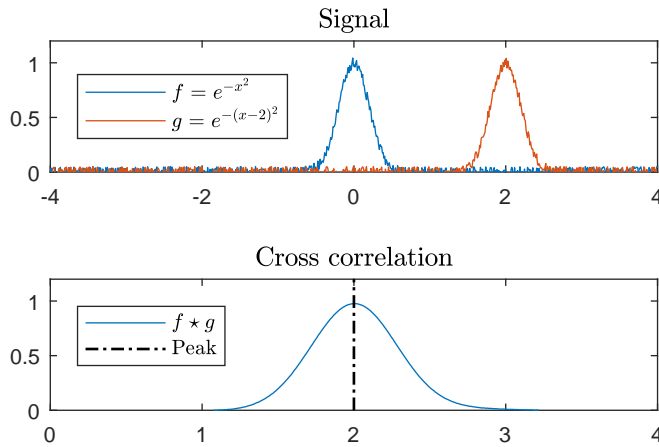

Figure 3.13: Cross correlation of a delayed Gaussian signal. The position of $\max(f \star g)$ gives the delay.

Digital Image Correlation algorithm: Similarity properties of cross-correlation is exploited to search for patterns in sub regions of image pairs:

1. **Interrogation windows:** The image pair $(I_0(x, y), I(x, y))$ is divided into sub regions f, g.

2. **Cross correlation:** A cross correlation $C = f \star g$ is calculated for the interrogation window.

3. **Peak location:** The peak of C is located and used to calculate the strain vector $(\Delta \mathbf{r})$, where accuracy is increased by performing sub pixel interpolation to compensate for spectral leakage.

4. **Loop:** Step 1-3 is repeated for all interrogation windows and the full strain field $\Delta \mathbf{r}(x, y)$ is obtained.
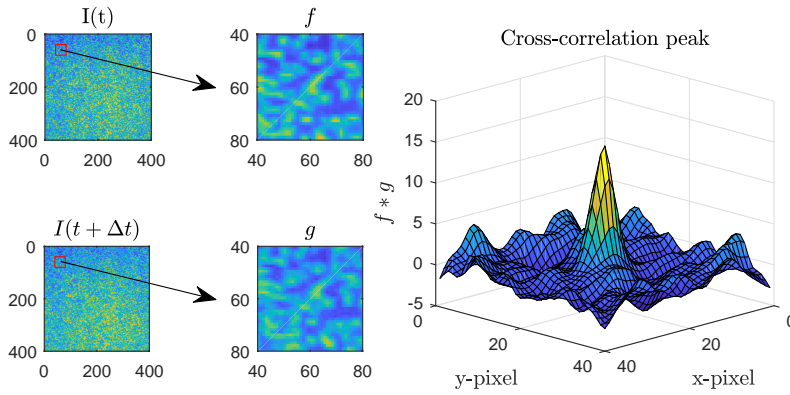

Figure 3.14: Interrogation windows and cross correlation peak. $\Delta \mathbf{r}$ is calculated in each interrogation widow resulting in $\Delta \mathbf{r}(x, y)$.

Figure 3.14 shows two schlieren images where a cross correlation is calculated on the red interrogation regions, where the location of the peak corresponds to the strain components $(\Delta x, \Delta y)$ located in the coordinates centered on the interrogation region.

Gradient calculation: The gradient field is calculated from optical relations and scaled to physical dimensions by a pixel pitch obtained from a calibration image (Equation 3.13).

$$\nabla h = \Delta \mathbf{r} / h^* p_{\text{pitch}} \tag{3.13}$$

3.2.4 Least Square Inversion

To obtain the surface height (h) from the gradient (∇h) calculated from Digital Image Correlation (DIC9, an inversion technique is performed where the gradient field is discretized by finite differences (Figure 3.15), resulting in a system of $2(M \times N)$ equations and $M \times N$ unknowns for h. The system is solved by least square matrix inversion defined in Equation 3.14b.
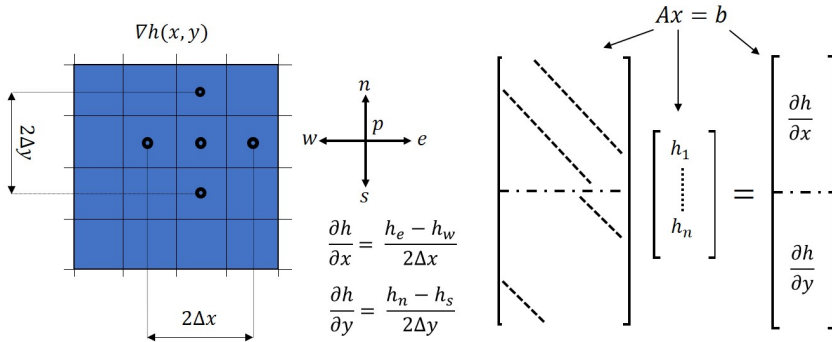

Figure 3.15: The gradientfield, ∇h is discretized in each pixel, resulting in an overdetermined system of equations for h.

$$\nabla h = \left[\frac{h_{\text{east}} - h_{\text{west}}}{2\Delta x}, \frac{h_{\text{north}} - h_{\text{south}}}{2\Delta y} \right] \tag{3.14a}$$

$$A\mathbf{x} = \mathbf{b} \qquad \mathbf{x} = (A^T A)^{-1} A^T \mathbf{b} \tag{3.14b}$$

Sparse matrix: The system has two main diagonals except for the boundary cells where forward and backward differences has been used. The system can therefore be described as a sparse system, significantly reducing inversion time.
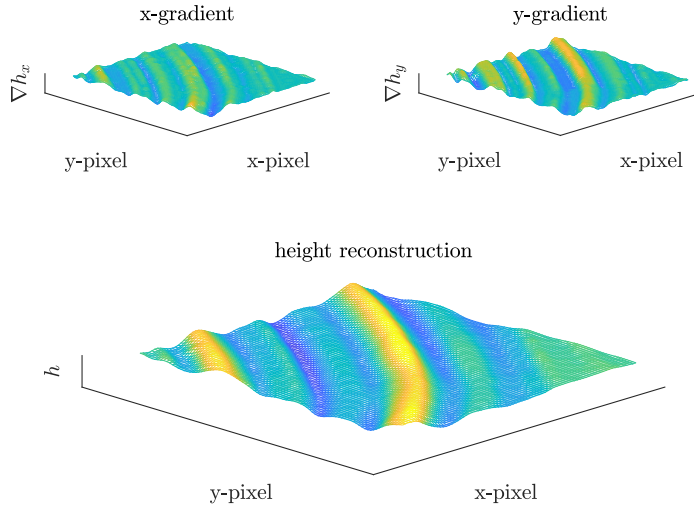
Figure 3.16: The gradient field ∇h, calculted from DIC and the reconstructed surface h from Least Square Inversion (LSI).

Singularity caused by non existing boundary conditions: Figure 3.16 show the inversion procedure performed on an image pair obtained from the schliren camera. However, there is a limitation to the reconstruction. since there are no boundary conditions, the inversion is singular (several solutions exists shown in Figure 3.17),hence the mean surface elevation $(\overline{h})$ is undetermined and has be constrained to be zero, which is a restriction of the method.
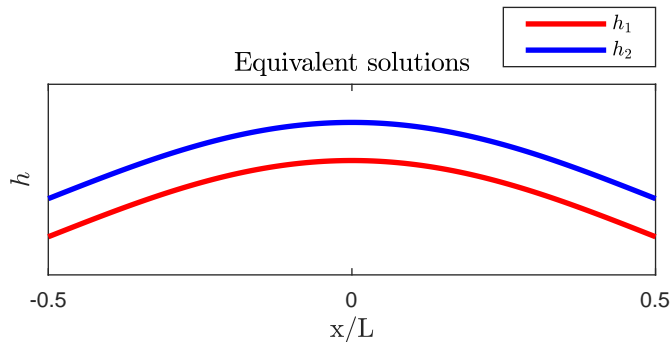

Figure 3.17: Equivalent solutions. The gradient is the same at all point for both curves, hence both are solution to the gradient inversion.
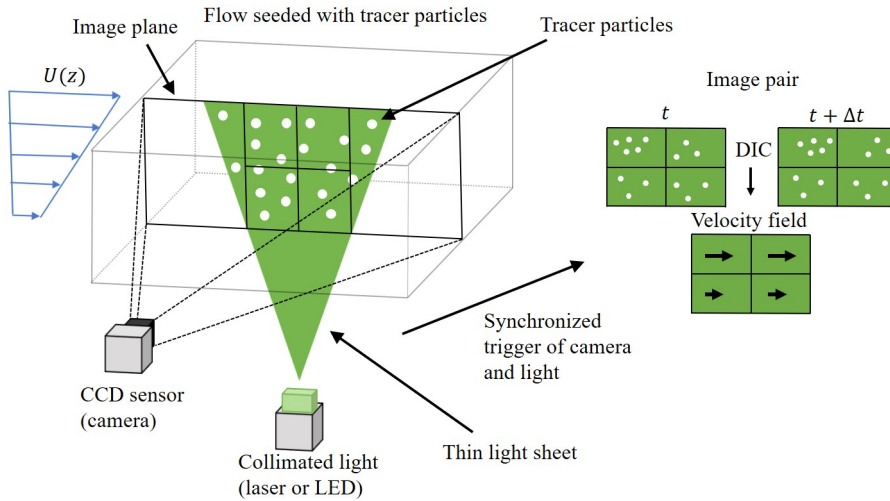
3.3   Particle Image Velociometry

Figure 3.18: PIV principle. The flow field is seeded with small tracer particles, which are illuminated and imaged in a light sheet. Movement of tracer particles between sub-sequential frames are calculated and used to calculate instantaneous velocities.

Procedure: Particle Image Velocimetry (PIV) is an optical method where the velocity field is measured by imaging the movement of seeding particles convected with the flow in a thin illuminated light sheet. Digital image correlation (DIC) is used to calculate the average movement ($\Delta\mathbf{r}$) of particles in interrogation windows between sub-sequential frames separated by time interval Δt, and velocity vectors are calculated. Figure 3.18 show the principle for monoscopic PIV, were the 2D instantaneous velocity field $u(x, z)$ is obtained.

1. **Data sampling by imaging:** Image pairs $(I(x, z, t), I(x, z, t + \Delta t))$ are sampled by a camera.

2. **Pre-processing:** To enhance the quality of DIC, the images are pre-processed.

3. **Digital Image Correlation:** The strain $(\Delta r(x, z))$ is calculated by DIC.

4. **Velocity calculations:** Velocities $(\mathbf{u})$ are calculated by scaling the strain to physical dimensions by $\mathbf{u} = \Delta\mathbf{r}/\Delta t$.
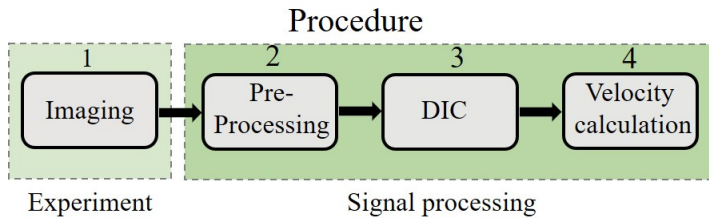
Procedure

Figure 3.19: PIV procedure.

Challenges: To obtain high quality PIV data, the major challenge lies within obtaining images with enough contrast and light intensity to get distinct peaks in the cross-correlation. Obtaining good images requires a sensitive camera with flexible aperture, shutter time, and gain along with a light source that can be collimated to a thin sheet with high light intensity, where both camera and light source is triggered in synchronized pulses.

Imaging and light optics:

- **Light optics:** Lasers are often used to generate a light sheet with high light intensity. In this thesis high power LED's are implemented instead.

- **Camera:** The camera needs to be sensitive where shutter time, gain, and aperture can be tuned to obtain good images.

- **Tracer particles:** Physical properties of the tracer particles needs be compatible with the fluid properties and flow velocities in order to be neutrally buoyant, scatter enough light, and follow fluid stream lines.

Data processing:

- **Pre-processing:** Different pre-processing steps can improve DIC results from image pairs.

- **Digital Image Correlation:** DIC is used to calculate the average movement of tracer particles within interrogation windows.

- **Post-processing:** Sometimes DIC results in bad or spurious vectors, which can happen if some regions are affected by noise, or if there are no tracer particles. Post-processing can be performed to improve the resulting velocity filed obtained from DIC.

3.3.1 Seeding particles and Stokes number

In order to calculate local velocities from image pairs of moving particles, the particles must represent flow velocities, hence follow flow streamlines. The particle response time can be calculated by solving the equations of motion (Equation 3.15a) for a particle released in a uniform flow, where the drag force is assumed to be modeled by creeping flow.
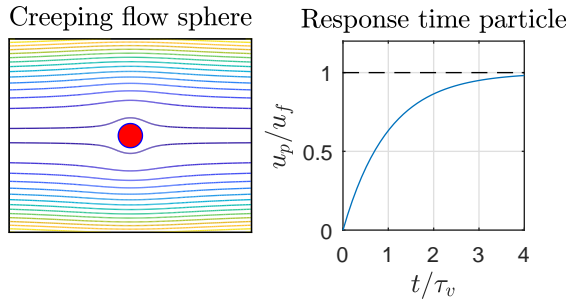

Creeping flow sphere   Response time particle

Figure 3.20: Streamlines for creeping flow around a sphere (left) and particle response time τ_v (right).

Particle response time: Solving Equation 3.15a results in an analytic expression (shown in Figure 3.20) for the particle response time as a factor of particle density and diameter (ρ_p, d_p), and flow speed and fluid viscosity (u_0, μ_c).

$$\rho_p V_p \frac{\partial u_p}{\partial t} = f_{\text{drag}} = \frac{1}{2} C_d A_{\text{surf}} \rho_f (u_f - u_p) \tag{3.15a}$$

$$u_p = u_f \left(1 - e^{-t/\tau_v}\right) \qquad \tau_v = \frac{\rho_p d_p^2}{18\mu_c} \tag{3.15b}$$

Stokes number: A dimensionless number called the Stokes number, is defined as the ratio between the particle response time and the characteristic time of the flow (Equation 3.16). Stk < 1 indicates that the particle follows fluid streamlines closely, which is required for particles to represent fluid velocities.

$$\text{Stk} = \frac{\rho_p d_p u_0}{18\mu_c} \tag{3.16}$$

Requirement: The Stokes number must be small (Stk< 1), hence the characteristics of the seeding particles must be chosen with respect to the stokes number.

3.3.2 Pre processing

Image pairs obtained from the PIV camera can be of poor quality caused by uneven light scattering, noise, out of focus particles and smearing effects. Pre-processing of the image pairs increases the signal to noise ratio (SNR) and can result in less spurious vectors from Digital Image Correlation (DIC).

Pre processing techniques:

- **High pass filter (HP):** Used to reduce the effect of uneven light intensity over the image. Using a Gaussian filter in Fourier space to achieve this.

- **Low pass filter (LP):** Used to reduce noise appearing as high frequency oscillation of intensity. Using a Gaussian filter in Fourier space to achieve this.

- **Intensity capping (IC):** Used to normalize the intensities such that all the particles left have the same intensities. Sets all intensities above a threshold to the threshold value, $I > I_{\text{threshhold}} = I_{\text{threshhold}}$.

- **Noise capping (NC):** used to reduce background noise. Set all intensities below a threshold to zero. $I < I_{\text{threshhold}} = 0$.
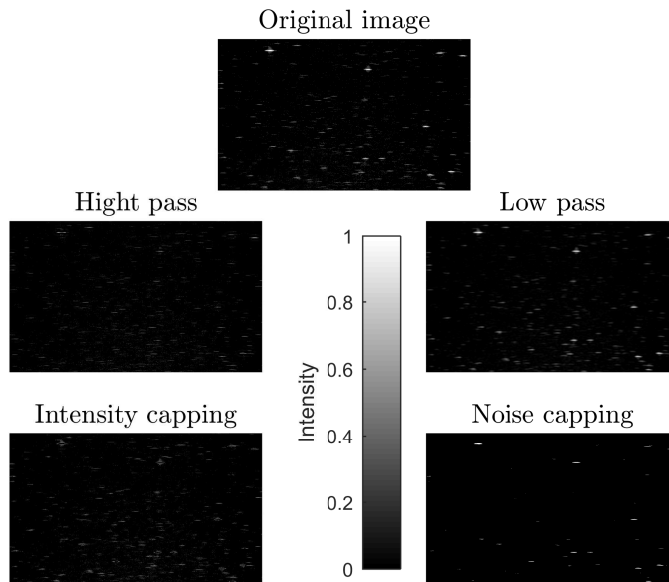

Figure 3.21: Pre-processing demonstrated on image obtained from the PIV camera.

3.3.3   Digital Image Correlation

DIC extracts the average displacement ($\Delta\mathbf{r}$) of particles between two sequential frames separated by time increment Δt. The procedure is performed in interrogation windows and a velocity is calculated by $\mathbf{u} = \Delta\mathbf{r}/\Delta t$.

Steady flow fields: In this thesis, steady flow velocities are considered, and averaging in time is performed to get better signal noise ratios for the measurements. There are two main approaches to obtain the averaged velocity field for several image pairs.

1. **Average strain vectors:** Calculate the cross correlation (C) for each image pair, then find $\Delta\mathbf{r}$ and average the strain vectors.

2. **Average correlation:** Calculate the average cross correlation function (C) for all image pairs, then find $\Delta\mathbf{r}$.

The second step has been shown to give better results for steady flows, and is implemented in the processing in this thesis [31].

Similar to FS-SS algorithm: Expept for the averaging step, the DIC algorithm is the same used to extract information from the schliren patterns in FS-SS, and is explained in more detail in subsection 3.2.3.
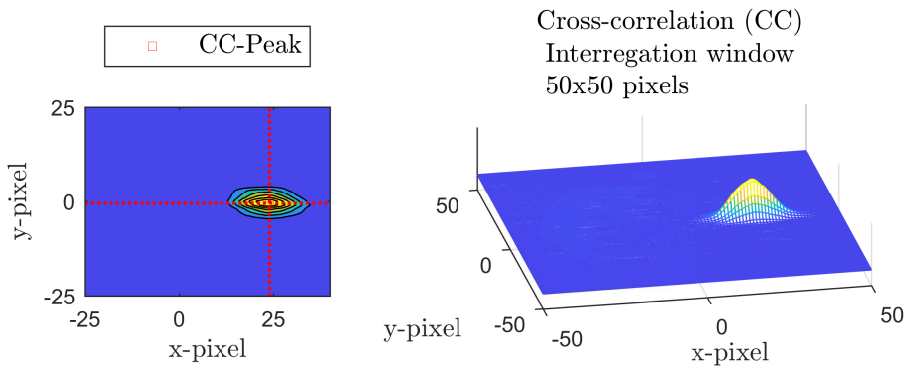

Figure 3.22: Average cross correlation function for interrogation window of size 50×50 pixels, where the peak location determines the strain $\Delta\mathbf{r}$.

Figure 3.23 shows the procedure performed on an image pair where particles are moving from left to right, where Figure 3.22 shows the averaged correlation function for the red marked interrogation window.

3.3.4   Velocity calculation

Interrogation window at t Interrogation window at $t + \Delta t$

Particle field at t Particle field at $t + \Delta t$
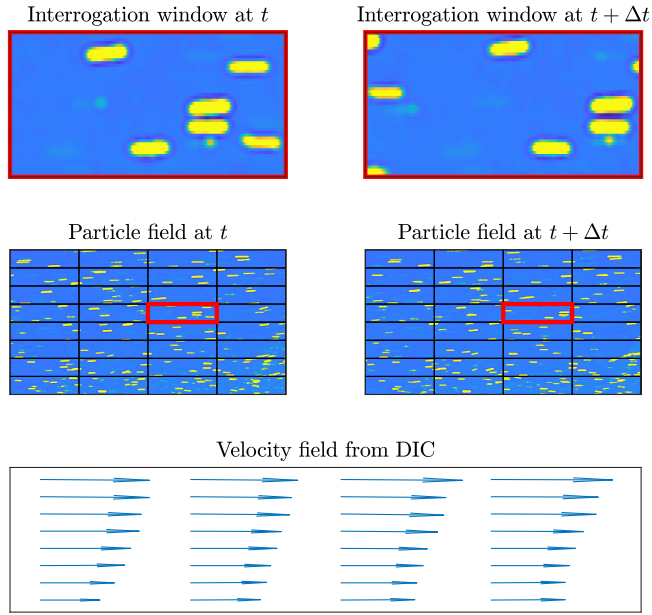
Velocity field from DIC

Figure 3.23: DIC for PIV image pair. The images is divided into interrogation windows where cross correlation determines local velocity as $\mathbf{u} = (\Delta\mathbf{r}/\Delta t)p_{\text{pitch}}$

$$\mathbf{u} = \big(\Delta\mathbf{r}/\Delta t\big)p_{\text{pitch}} \tag{3.17}$$

Velocity calculation: The vector field at the bottom (Figure 3.23) is calculated from Equation 3.17 where $\Delta\mathbf{r}$ is the strain vector which can be averaged over several image pairs. p_{pitch} is the pixel pitch scaling distances to physical dimensions.

3.4   Wave generation

To study waves in controlled environment, proper wave-making mechanisms where periodicity is predictable is essential. In this thesis two methods are implemented which will be described in this section.

1. **Pneumatic wavemaker:** A pneumatic system generating an air jet, causing a stagnation pressure on the free surface.

   Models: A model describing the stagnation pressure is developed where a combination of classic nozzle and jet flow is combined.

2. **Mechanical-wave makers:** A mechanical plate displaces fluid, where the plate motion is synchronized with the waves generated.

3.4.1   Pneumatic wavemaker

A pneumatic system generates airflow, resulting in stagnation pressure acting on the free surface as a perturbation. The stagnation pressure can be described as $p = \frac{1}{2}\rho u^2$ and a model is developed to obtain an explicit expression for $p(r, L)$. To describe p, the shape, and magnitude of u is needed and u will be approximated by assuming isentropic compressible flow through an orifice leading to a fully developed turbulent jet flow shown in Figure 3.24.
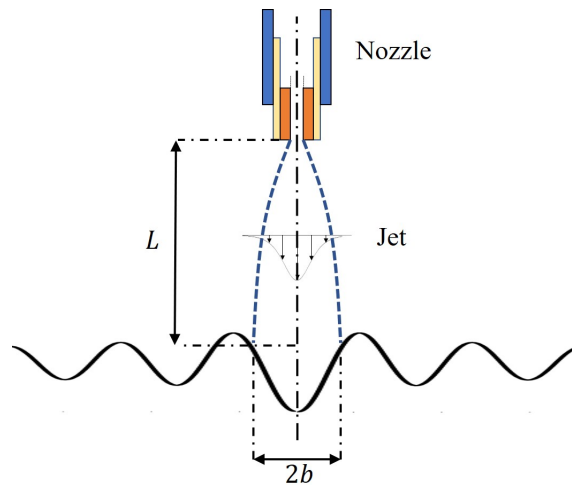

Figure 3.24: Pneumatic model where nozzle and jet flow is combined to describe $p(r, L)$.

Jet model: The solutions for a fully developed turbulent axisymmetric jet is shown in Equation 3.18 where the geometry is shown in Figure 3.25. More details on the derivations, assumptions etc. can be found in the following reference[32].
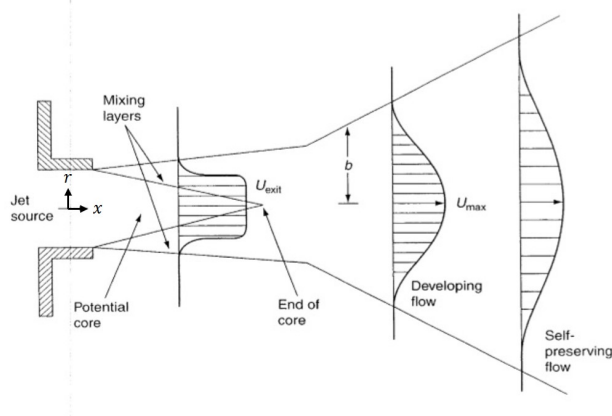

Figure 3.25: Turbulent jet [32]. Sufficently downstream, the flow is self preserving and J is enough to describe $u(x, r)$.

$$\frac{b}{x} \approx \tan 13 \qquad \frac{u}{U_{\max}} \approx \text{sech}^2 10.4 \frac{r}{x} \qquad U_{\max} \approx 7.4 \frac{\sqrt{J/\rho}}{x} \tag{3.18a}$$

$$J = \int_{-\infty}^{\infty} \rho u^2 dA = const = \rho u_{\text{mean}}^2 A^* = \dot{m} u_{\text{mean}} \tag{3.18b}$$

The divergence angle $\tan^{-1} b/x$ is independent of flow conditions and the velocity distribution depends only on J, which is the net momentum in the jet, that is preserved downstream. Hence, knowing the outlet conditions $(\dot{m} u_{\text{mean}})$ are enough to describe the flow field $u(x, r)$.

Nozzle model: Outlet conditions are modeled as a choked converging nozzle, meaning $Ma = 1$ and the flow has been accelerated to the speed of sound c. At choked conditions, the mass flow rate $\dot{m}$ reaches a maximum, described by Equation 3.19a, and is only dependent on the stagnation quantities related to the reservoir. Table 3.1 shows the critical ratios for air which relates the throat to the reservoir properties for $Ma = 1$.

$$\dot{m}_{\text{max}} = C_d A^* p_0 \sqrt{\frac{\kappa}{RT_0} \frac{2}{\kappa + 1}}^{\kappa+1/\kappa-1} \qquad u_{\text{mean}} = c = \sqrt{\kappa R T^*} \qquad (3.19a)$$

$$Ma = u/c \qquad \kappa = \frac{C_p}{C_v} \approx 1.4 \qquad J = \dot{m}_{\text{max}} u_{\text{mean}} = 0.74 C_d A^* p_0 \qquad (3.19b)$$

A^* is the throat area of the nozzle, p_0 and T_0 are the reservoir pressure and temperature. R is the universal gas constant and κ is the ratio of the two heat capacities, which for air is 1.4. C_d is the discharge coefficient corresponding to losses through the nozzle.

Property	Value
κ	1.4
p^*/p_0	0.5283
T^*/T_0	0.8333
ρ^*/ρ_0	0.6340

Table 3.1: Critical-pressure, temperature, and density ratios for isentropic air flow.[33].

Pressure model: The stagnation pressure on the surface is approximated as $p = \frac{1}{2}\rho u^2$. Substituting for u and simplifying results in Equation 3.20, explicitly describing the shape and magnitude of $p(r, L)$.

$$p(r, L) \approx 20.25 p_0 \frac{C_d A^*}{L^2} \text{sech}^4\left(10.4\frac{r}{L}\right) \quad b(L) \approx 0.23L \qquad (3.20)$$

3.4.2 Mechanical wave-makers

Description: Mechanical wavemakers are perhaps the most commonly used in scientific wave tanks [28]. The concept is to drive a mechanical part to displace liquid into wave motion, synchronized with the part motion. There exists numerous types which can be summarized by two fundamental modes, related to translation and rotation.
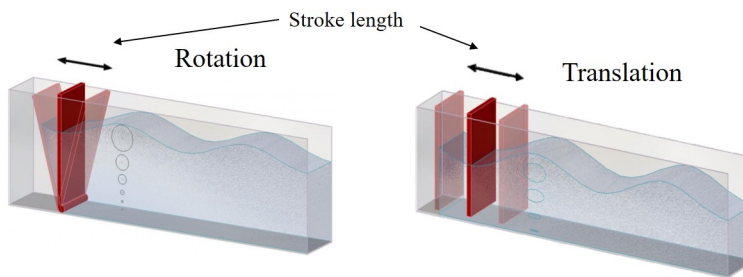

Figure 3.26: Paddle wavemaker (left) and Piston wavemaker(right) [1].

- **Flap wave-maker:** The plate is rotated resulting in a linearly depth displacement displacement.

- **Piston wave-maker:** The plate is translated resulting in a uniform displacement with depth.

Theoretical models describing the relationship between wave-maker motion and generated waves, can be derived from wave theory which can be found in detail in[28].

---

[1]http://www.edesign.co.uk/waves/some-wave-1/

Shallow water model: A simplified theory for plane wave-makers in shallow water, where the volume of the water displaced is assumed to be equal to the crest volume of the propagating wave (Equation 3.21). H/S is the height-to-stroke ratio where H is the wave amplitude and S is the stroke length. k_p is the wavenumber produced, and h is the water depth.

$$\left(\frac{H}{S}\right)_{\text{piston}} = k_p h \qquad \left(\frac{H}{S}\right)_{\text{flap}} = k_p h/2 \tag{3.21}$$
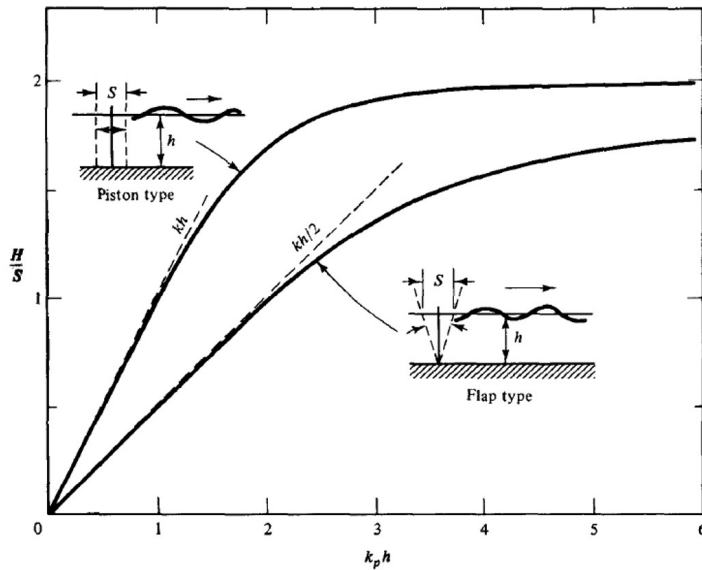

Figure 3.27: Displacement curves for piston (top) and flap (bottom) mechanical wavemakers [28].

Extended model: Equation 3.21 is only valid for shallow water waves where $k_p h < \pi/10$ and an extension of the theory is derived from wave theory where the resulting relationship for arbitrary depth is described by Equation 3.22, where Figure 3.27 shows the height to stroke ratio for relative depths $k_p h$.

$$\left(\frac{H}{S}\right)_{\text{flap}} = 4\left(\frac{\sinh k_p h}{k_p h}\right)\frac{k_p h \sinh k_p h - \cosh k_p h + 1}{\sinh 2k_p h + 2k_p h} \tag{3.22a}$$

$$\left(\frac{H}{S}\right)_{\text{piston}} = \frac{2(\cosh k_p h - 1)}{\sinh 2k_p h + 2k_p h} \tag{3.22b}$$

3.5 Shear flow generation

To study waves propagating on depth variation currents, generating a steady developed current profile is essential for the experiments. Scientists have generated models and implemented methods to generate flow conditions with uniform vorticity in experimental setups over the years [16, 17, 18, 19, 34]. In literature there are three common methods (Figure 3.28), which all share the same fundamental principle of directing streamlines through generating depth varying pressure drops across a section in the flow.

Methods: In this thesis the desired velocity field is not necessarily of uniform vorticity but of varying curvature with both strong and weak surface shear. However, the theories and implementations can inspire and be combined to generate other types of profiles.

- **Curved meshes:** A third method is add a curved mesh, where the flow streamlines are deflected, resulting in velocity gradients [16, 17, 18].

- **Staggered grids:** Perhaps the most common way is to add a plane parallel-rod grid of uniform rod diameter and non-uniform rod spacing. However this method introduces high turbulence intensities in the flow which is not desired for these experiments [19].

- **Shaped honeycombs:** Another method is to add a section of specially shaped honeycombs such that the pressure drag,which is modeled by pipe flow, gives a depth varying pressure drop across the honeycombs [34].
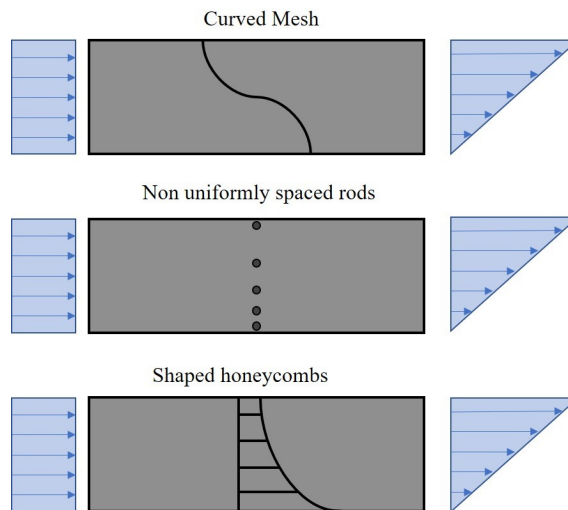

Figure 3.28: Methods for generating shear flows. The three methods (curved mesh,spaced rods,shaped honeycombs) all generate a depth varying pressure drop across a section in the flow resulting in deflection of streamlines.

Chapter 4

Experimental setup

In this section the experimental methods described in chapter 3 are implemented and tested individually before combined in chapter 5 and chapter 6 where case studies with waves are presented.

1. **Implementation of Fourier Transform Profilometry:** projector/camera configuration installed to perform coaxial FTP.

2. **Implementation of Free Surface Synthetic Schliren:** Camera/schliren pattern configuration to perform FS-SS.

3. **Implementation of Particle Image Velociometry:** Camera/light optics configuration to perform PIV measurements in the flow channel.

4. **Flow channel and shear flow generation:** Implementation of methods to generate shear flow conditions in the flow channel.

5. **Implementation of wave-makers:** Implementation of pneumatic and mechanical wave-makers.

Symbols used in Implementation Fourier Transform Profilometry

L	Projector reference length	k	Wave-number
D	Projector camera length	(H_1, H_2)	Height calibration pyramids
P	Gray scale pattern length	(L_1, L_2)	Base length calibration pyramids
p	Gray scale pattern wave-length in pixels	(β_1, β_2)	Average slope calibration pyramids
h	Surface height	X_{FTP}	Measured quantity FTP
I	Gray scale intensity	X_{Caliper}	Measured quantity caliper
p_{pitch}	Pixel pitch	σ_e	Relative difference
φ	Image phase shift	(x, y)	Cartesian coordinates image plane
Φ	Normalized phase shift		
α	Optical parameter	(x', y')	Cartesian coordinates shifted image plane
λ	Wavelength		

Symbols used in Implementation of Free Surface Syntethic schlieren

(x, y, z)	Cartesian coordinates	h_p	Effective depth
∇h	Surface gradient	h_a	Air gap distance
Δr	Image strain	$h*$	Optical depth
n	Refractive index		
L	Length Schlieren pattern	α	optical parameter
H	Camera water distance	N	Number of dots schlieren pattern
h	Surface height	D	Dot diameter schlieren pattern
h_0	Water depth		
h_g	Thickness Perplex plate	N_{pixels}	Number of pixels
		p_{pitch}	Pixel pitch

Symbols used in Implementation of Particle Image Velocimetry

I	Image gray scale intensity	ρ_p	Particle density
t	Time	μ_w	Dynamic viscosity water
Δt	Time increment	u_0	Flow velocity
h	Water depth	(R_1, R_2)	Circuit resistors
t_s	Light sheet thickness	(C_1, C_2)	Circuit capacitors
L_s	Light sheet length	V_{in}	Circuit voltage
t_s	Light sheet thickness	V_{LED}	LED voltage
L_d	Camera light sheet distance	(L_1, L_2)	Fiber array/lense/light sheet distances.
τ_l	LED pulse time length		
τ_s	LED pulse separation Time	N_{pixels}	Number of pixels
d_p	Particle diameter	p_{pitch}	Pixel pitch

Symbols used in Flow channel setup and implementation of curved mesh

b	Flow channel width	U	Flow velocity
h	Water depth	Q_{pump}	Pump flow rate

Symbols used in Implementation of Wave-makers

f	Forcing frequency nozzle/mechanical wave-maker	C_d	Drag coefficient
A^*	Nozzle throat surface area	(r, L)	Jet coordinates relative nozzle
p_0	Nozzle back pressure	D	Diameter nozzle exit
L	Distance nozzle/free surface	S	Stroke length
b	Radius of perturbed area	V_{in}	Input voltage

4.1 Implementation of Fourier Transform Profilometry

Figure 4.1 shows the implementation of a FTP setup where a projector and a camera is coaxial to a reference plane (free liquid surface/plate). L, D, and P, are lengths related to the optical relations $(h = f(\Delta\varphi))$, which needs to be calibrated to reduce uncertainty of the measured surface height (h). A lab computer controls the camera and the projector, where the fringe pattern is generated as a Matlab figure.
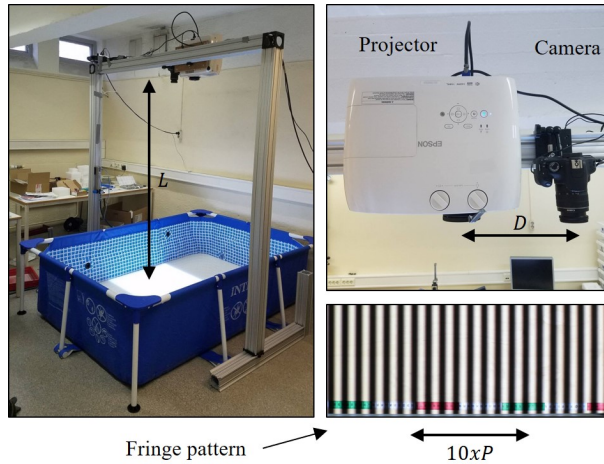

Figure 4.1: Optical setup for coaxial FTP. L, D and P are lengths related to the optical relations $h = f(\Delta\varphi)$.

Devices:

- **Camera:** Canon EOS 1200 controlled by EOS utility application.

- **Projector:** Epson EH-TW6700 which is a full HD projector with lens shift and high light output (3000 lumen). The projection Ratio (PR) can be set in the range [1.32 - 2.15:1].

- **Lab computer:** Data sampling of images and fringe pattern projection is controlled from a lab computer.

- **Titanium dioxide (TiO$_2$):** Water is transparent and titanium dioxide is added to enhance diffuse reflection on the free surface.

- **Linear polarizers:** To reduce bright spots caused by specular reflections, orthogonal polarizers are added as light filters.

4.1.1 Parameters and limitations

Parameters:

- **Lengths** (L, D)**:** L must be scaled to cover the region of interest $(L(\text{PR})>$ domain size), while D is scaled to adjust sensitivity $(\alpha = L/D)$, avoiding phase jumps $\Delta\varphi < 2\pi$.

- **Pattern wavenumber** (P)**:** $P = p_{\text{pitch}}p$ where p is the wavenumber scaled in pixels/period and P is scaled to physical dimensions by the pixel pitch. A limitation is that wavenumbers shorter than P $(k < P)$ is filtered in the signal processing algorithm.

- **Camera settings:** To obtain good image contrast, shutter-time, gain and aperture is tuned.

    - Frame rate: [25/50] Hz.

    - Resolution: [1920 x 1080 /1280 x 720] Pixels.

Limitations:

- $p < 16 \Leftrightarrow$ The fringe pattern must have sufficient contrast and $\lambda_{\text{max}} < P$ is the filtered and can not be reconstructed.

Figure 4.2 show two fringe patterns where $p = 32$ and $p = 8$ and if p is chosen too small, the recorded image is more sensitive to pixel intensity noise.

| nx = ny = 256 | p=32 | nx = ny = 256 | p=8 |

| Field of interest | zoomed area | Field of interest | zoomed area |
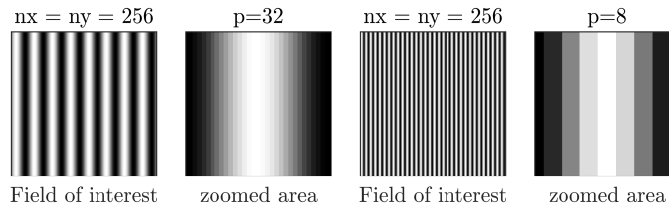
Figure 4.2: Fringe pattern characteristics. $p = 32$ (left) and $p = 8$ (right). $p < 16$ to avoid low SNR values.

4.1.2 Optical calibration

The uncertainty of optical parameters (L, D, P) determines the accuracy of the reconstructed surface (h). p_{pitch} is determined by adding a calibration plate to the reference image scaling p to physical dimensions P. L and D are obtained by a least square calibration technique. By inverting the problem, the parameters (α, L, D) can be calculated (Figure 4.4) using calibration blocks (shown in Figure 4.3) where h is known, and fitting the data points (Φ_i) to the optical relation model.
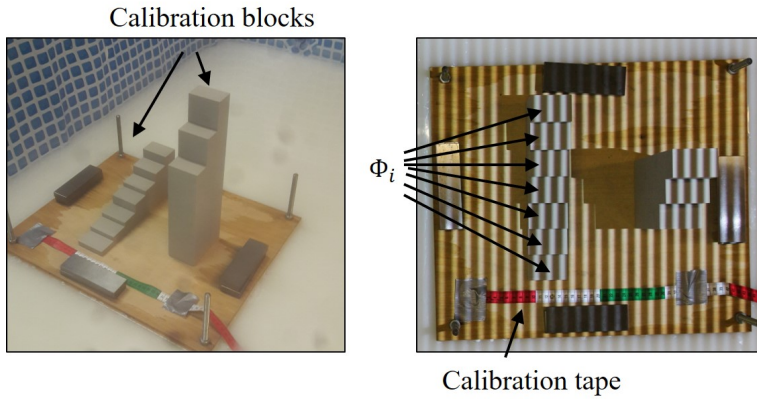
Calibration blocks

Calibration tape

Figure 4.3: Calibration blocks for FTP where Φ_i is extracted and fitted to the optical relation.

$\alpha = 3.52\ (3.506,\ 3.534)$

$L = 1507\ (1465,1550)\ [\text{mm}]$

$D = 428\ (418,438)\ [\text{mm}]$

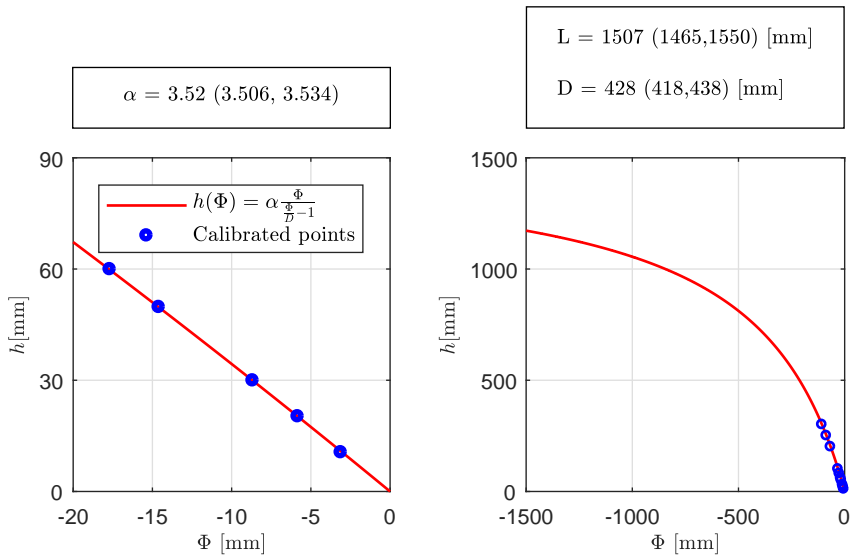$h(\Phi) = \alpha \frac{\Phi}{\frac{\Phi}{D} - 1}$

Calibrated points

Figure 4.4: Calibration points (blue dots) and least square fitted curve (red curve) for $h(\Phi)$. Linear region (left) and full region (right). Note that the uncertainty is lower for α than for (L, D).

4.1.3 Test object and error estimates

Objective: To test the accuracy of a calibrated system, two wedge pyramids (shown in Figure 4.5) are constructed and measured. FTP is used to reconstruct the height profiles (h) of the pyramids and compared to the designed characteristics, where the effect of spatial distortion is calculated and demonstrated.
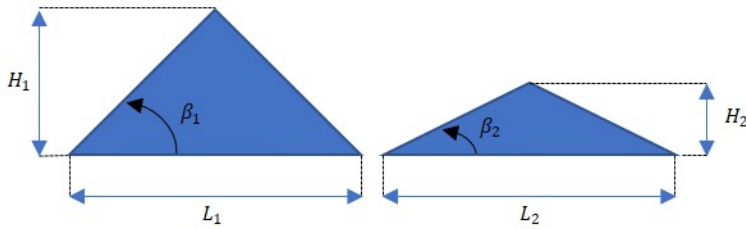
Figure 4.5: Wedges used to test calibrated FTP setup. Two wedge profiles (with base lengths $L1 = L2 = 200$ mm, and heights $H1 = 57.9$ mm, $H2 = 30.3$ mm) are constructed, where (β_1, β_2) is the average slope.
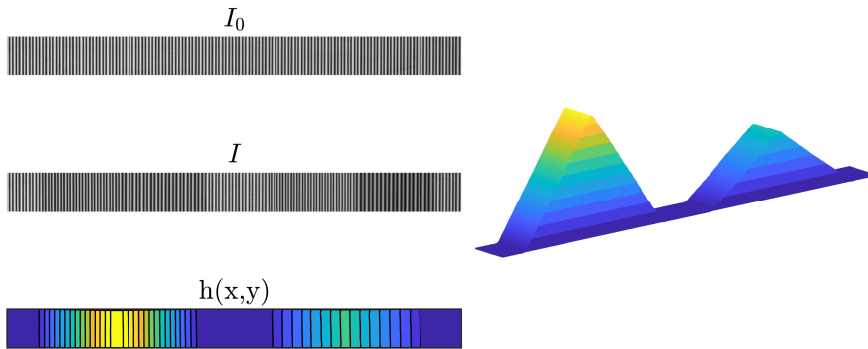
Figure 4.6: Reference and profile image (top left), contours of $h(x, y)$ (bottom left), and isometric view of $h(x, y)$ (right).

Reconstruction: Figure 4.6 shows images(I_0, I) and the reconstructed profile ($h(x, y)$), which are compared to the profiles measured by a caliper. The metrics shown in Figure 4.5 are compared (shown in Table 4.1), where σ_e is the relative difference calculated by Equation 4.1 where X represents any of the measured quantities. The error for a calibrated system is less than 1% for the reconstructed height (h), which is consistent with the uncertainty in the calibrated α.

	L_1	L_2	H_1	H_2	β_1	β_2
FTP	100	100	57.9	30.3	0.579	0.303
Caliper	100	100	58.4	30.16	0.574	0.302
σ_e	0	0	0.9	0.5	0.8	0.3

Table 4.1: Results test objects for calibrated FTP system.
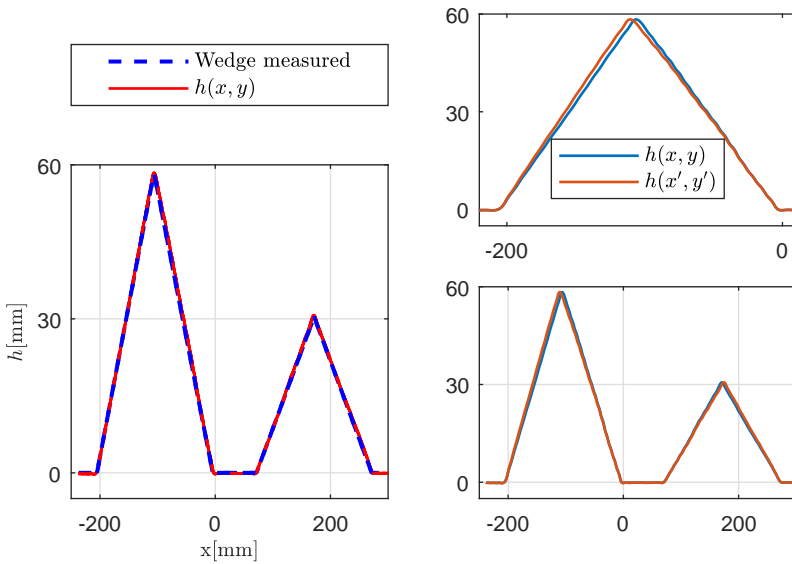
$$\sigma_e = \frac{X_{\text{FTP}} - X_{\text{Caliper}}}{X_{\text{FTP}}} \tag{4.1}$$

Figure 4.7: Wedge profiles FTP and caliper (left), and reconstructed profiles before and after interpolation (right)

Coordinate shift: The coordinate shift (top right Figure 4.7) is roughly 4.5% at $h = 60$, which is significant and is corrected by interpolating $h(x', y')$ to $h(x, y)$.

4.1.4 Bright spots and linear polarizers

FTP is depending on a reflective surface where the fringe pattern reflects due to diffuse reflections. Performing FTP on a water surface, is done by adding color pigments (TiO_2) to the liquid. There will also be bright spots due to specular reflections (Figure 4.8) saturating the images and contaminating the periodic signal.
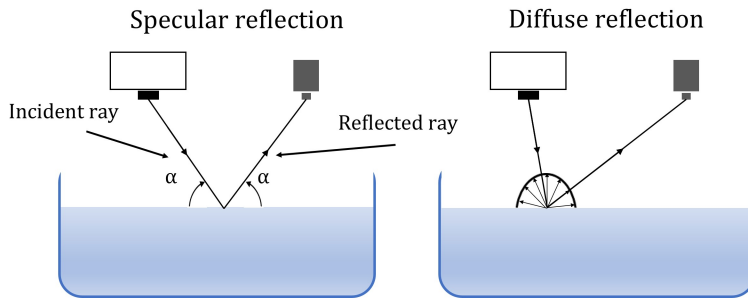
Figure 4.8: Specular (left) and diffuse (right) reflections. Specular reflections causes bright spots contaminating the signal ($I(x, y)$).

Orthogonal polarizers: Specular reflected light has the same polarization as the incoming light. To reduce bright spots from specular reflections, two orthogonal linear polarization filters are added to the optical system, which blocks the linearly polarized reflections. FTP images taken with and without polarizers are shown in Figure 4.9, where the bright spots are significantly reduced.
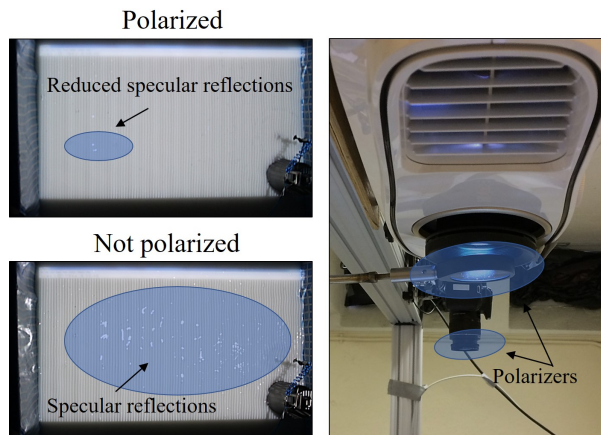
Figure 4.9: Images of the fringe pattern with (top) and without (bottom) polarizers, where the bright spots are significantly reduced.

4.2 Implementation of Free Surface Synthetic Schlieren

Figure 4.10 show the FS-SS setup where a schliren pattern (random dots covering 60×60 cm) is mounted below a transparent perplex plate lighted from below with a LED light plate. A camera is mounted above and used to record time series of the refracted pattern controlled from a computer.
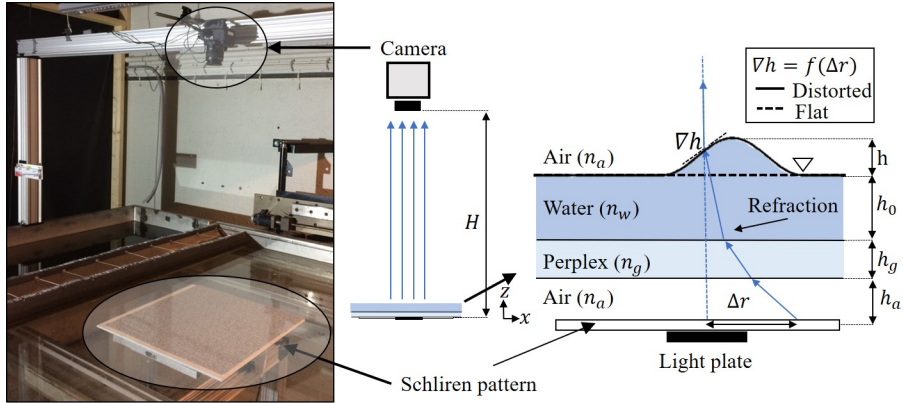

Figure 4.10: Optical setup for FS-SS where a camera is mounted above the free surface, and a random dot pattern is mounted below, lighted by a LED panel light (left). The schematics of the system are shown (right) where light gets refracted due to change of angle at the free surface.

Devices:

- **Camera:** Canon EOS 1200 controlled by EOS utility application.

- **Lab computer:** Data sampling of images is controlled from a lab computer.

- **Schlieren pattern:** A random dot pattern (generated by Matlab), is printed out and mounted below the perlex plate.

- **Light source:** A 60x60cm panel led light is mounted below the schliren pattern to enhance image contrast.

Transparency requirement:

1. **Transparent bottom:** The bottom plate shown in Figure 4.10 is made of perplex which allows for the pattern to be visualized from below.

2. **Transparent fluid:** The pattern must be diffracted through the fluid which restricts the method to only work for transparent fluids.

4.2.1 Parameters and limitations

- **Camera settings:** To obtain good image contrast, shutter-time, gain and aperture is tuned.

    - Frame rate: [25/50] Hz.

    - Resolution: [1920 x 1080 /1280 x 720] Pixels.

- **Air gap distance** (h_a)**:** An air gap (h_a) is added to scale the proportionality in Equation 4.2, where Figure 4.11 shows the linear relationship for different values of h_a, and optical parameters are listed in Table 4.2.

$$\nabla h = -\frac{\Delta r}{h^*} \qquad \frac{1}{h^*} = \frac{1}{\alpha h_p} - \frac{1}{H} \tag{4.2a}$$

$$h_p = h_0 + \frac{n_w}{n_g} h_g + \frac{n_w}{n_a} h_a \qquad \alpha = 1 - \frac{n_a}{n_w} \tag{4.2b}$$
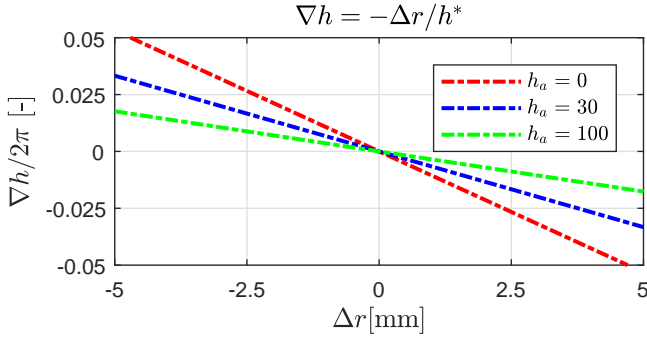
Figure 4.11: Optical relation for FS-SS. By adding an air gap (h_a) the sensitivity is increased (larger shifts)

Lengths	Unit [m]	Refracive index	Unit [-]
H	$\sim$2.00	air n_a	1.0
h_0	variable	water n_w	1.3
h_p	0.02	perplex n_g	1.5
h_a	Variable		

Table 4.2: Setup parameters for FS-SS. Water depth (h_0) and air gap distance (h_p) vary from the different experiments.

- **Pattern geometry:** Depending on the wavelengths and amplitudes of ∇h, the schlieren pattern are scaled to give favorable DIC. Random dot patterns for different parameters (N, D) is seen in Figure 4.12.

    1. **Dot density** (N)**:** Is the number of dots per area.

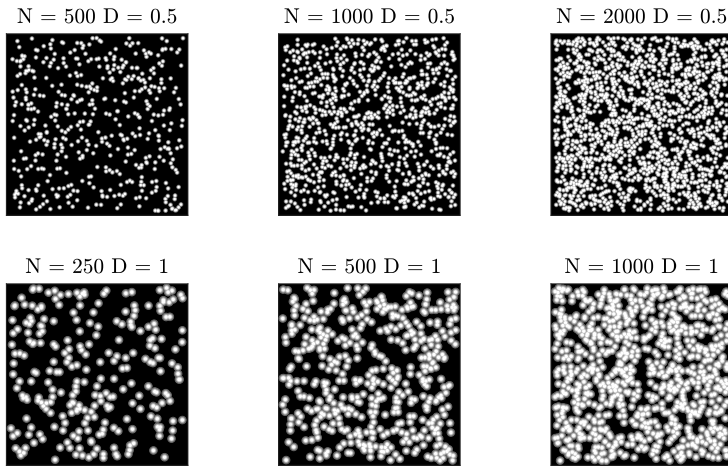   2. **Dot diameter** (D)**:** Is the diameter of the dots.

N = 500 D = 0.5   N = 1000 D = 0.5   N = 2000 D = 0.5

N = 250 D = 1   N = 500 D = 1   N = 1000 D = 1

Figure 4.12: Random dot patterns for different densities (N) and diameters (D).

- **Pattern/camera distance** (H)**:** Is chosen be such that small angle approximation is valid $(H \ll \sqrt{L}.)$

- **Water depth** (h_0)**:** The water depth changes from experiments but has to be $h \ll h_0$ to obey the small amplitude approximation.

- **Frame rate camera** f_0**:** The camera frame rate is chosen depending on which frequencies $(\omega/2\pi)$ that are studied.

Limitations:

- **Maximum wavelength:** The domain size determines the maximum measurable wavelength $(\lambda_{\mathrm{max}} = L)$.

- **Maximum frequency:** The camera frame rate determines the maximum measurable frequency $(\omega/2\pi = f_0/2)$.

4.2.2   Optical calibration

Pixel calibration: Δr is scaled to physical dimensions by multiplying by a pixel pitch (Equation 4.3) , calculated from a calibration image seen in Figure 4.13. L is the length of the calibration plate and N_{pixels} are the number of pixels obtained from the image.
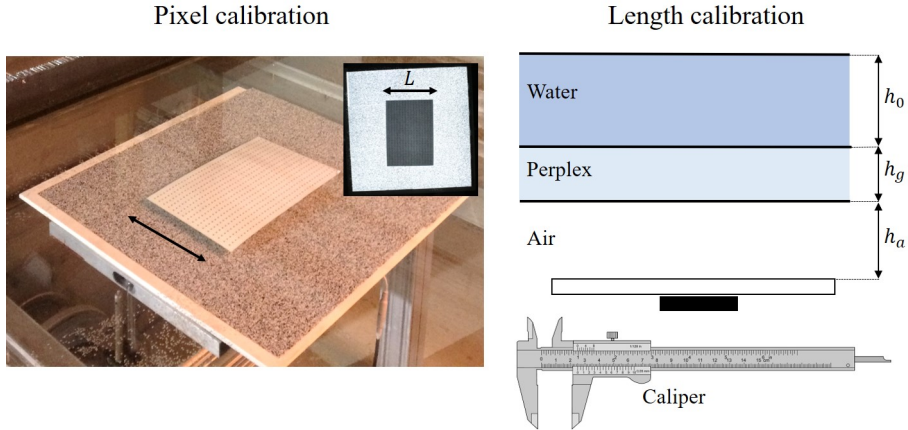
$$p_{\text{pitch}} = L/N_{\text{pixels}} \tag{4.3}$$

Figure 4.13: Pixel pitch calibration (left) and length calibration (right) for FS-SS. Δr is scaled to physical dimensions with the pixel pitch.

Length calibration: The optical parameters (h_0, h_g, h_a) are measured by a caliper. A calibration method similar to the inversion technique used for FTP were discussed, but the errors caused by the approximations used to derive the optical relations are in the same order of magnitude as the caliper measurements. Therefore a simple caliper calibration is sufficient for this setup.

4.3   Implementation of Particle Image velociometry

Figure 4.14 shows the optical PIV setup, where a scientific camera is mounted perpendicular to a light source, illuminating a thin sheet through the bottom of the plate. The camera is triggered in double exposures with a pulse separation resulting in image pairs where both the exposure time and pulse separation can be adjusted. The light source consists of a capacitor/LED circuit where a Mosfet transistor triggers high current pulses through the LED chip which is synchronized with the camera exposure.
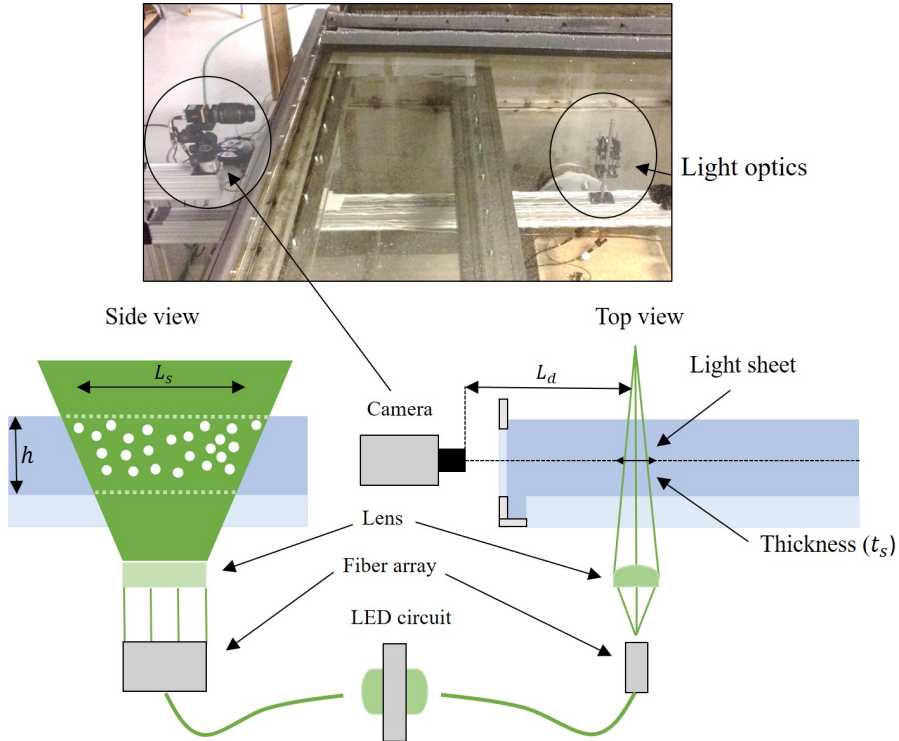
Figure 4.14: Flashes of light are synchronized with camera triggers giving image pairs of particles separated by the pulse separation time.

Devices:

- **Camera**: Imperx B1610 Monochrome which is a programmable scientific camera where shutter time and gain can be adjusted. The camera can be triggered in double exposure pulses resulting in image pairs with short time separation.

- **LED circuit**: A capacitor circuit, where pulses of high current is discharged through a high power Light Emitting Diode (LED).

- **Lens optics**: The light emitted from the LED is collimated to a thin sheet with high intensity by fixing a bundle of optical fiber in front leading to a thin array diverged through a cylindrical lens (described in subsection 4.3.2).

- **High speed DAQ**: Both the camera and the LED circuit is triggered by a high speed DAQ from National Instruments.

- **Lab computer:** The system is synchronized and controlled through a lab computer.
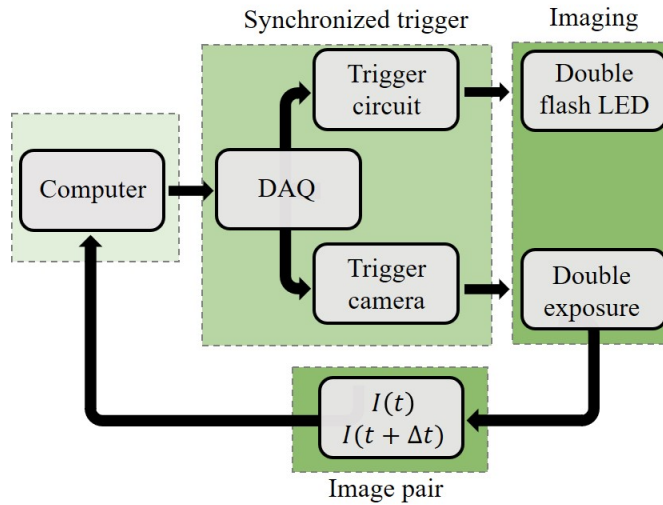
Figure 4.15: Flow chart showing the data sampling procedure for the PIV system.

4.3.1 Parameters and limitations

- **Light sheet:** Light sheet parameters depends on the position of the light optics.

  - **Thickness** (t_s)**:** Light sheet thickness is adjusted by the position of the lens relative to the fiber array.

  - **Camera/sheet distance** (L_d)**:** The distance from the camera to the light sheet. Larger distance results in weaker particle signal.

  - **Sheet length** (L_s)**:** The sheet length is roughly the same as the fiber array (40mm) which restricts the measurement area downstream

- **Camera settings:** Depending on PIV position and signal strength, camera settings are adjusted to obtain as clean signal as possible by adjusting the following camera parameters.

  - **Lens focus:** The camera is focused on the particles in the light sheet.

  - **Gain:** Gain amplifies the signal where too much enhances noise, while to little reduces signal strength.

  - **Shutter time:** Shutter time must be shorter than the pulse separation (τ_s).

  - **Aperture:** The aperture is fully opened to maximize the amount of light intensity reaching the CCD.

- **Trigger parameters:**

  - **Pulse length** (τ_l)**:** The time length of the trigger pulse.

  - **Pulse separation** (τ_s)**:** The time length between trigger pulses, which is proportional to particle separation. Pulse separation is tuned to obtained good DIC calculations (Roughly 25% displacement).

  - **Circuit voltage** (V_{in})**:** Proportional to the light intensity emitted from the LED. Must be operated within working conditions and is scaled according to the pulse length.

- **Particle size and Stokes number:** The particles used are polystyrene from Microbeads AS, which has similar density to water and are therefore neutrally buoyant.

  - **Diameter** d_p**:** 40μ [m]

  - **Density**ρ_p**:** 1000 [kg m^{-3}]

  - **Viscosity water** μ_c**:** $1.0021e - 3$ [Pa s]

  - **Stk:** Stk $= 2.2u_0$

Velocity limit: $u_0 < 0.45$ [m/s], which is calculated from the stokes number.

4.3.2 LED circuit and light collimation

Capacitor circuit: An LED chip powered by a capacitor circuit triggered by a mosfet transistor (seen in Figure 4.16) is used as light source. Pulses of high current is discharged through the LED resulting in flashes with high light intensity where both the pulse length (τ_l) and pulse separation (τ_s) is controlled by a computer.
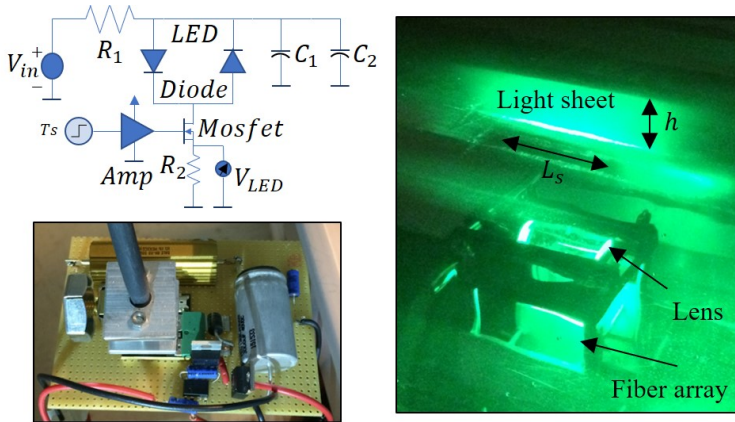

Figure 4.16: LED curcuit (left) and lens optics (right). High currents are dumped through the LED on triggered signal resulting in a thin light sheet of high intensity.

Light collimation: Figure 4.17 shows the schematic of ray geometry where light emitted from the fiber array is focused to a thin sheet by a cylindrical lens. f_{lens} is the lens focal length, L_1 is the array/fiber distance, and L_2 is the lens/focal point distance. The light sheet thickness (t_s) is adjusted by tuning L_1 and L_2.
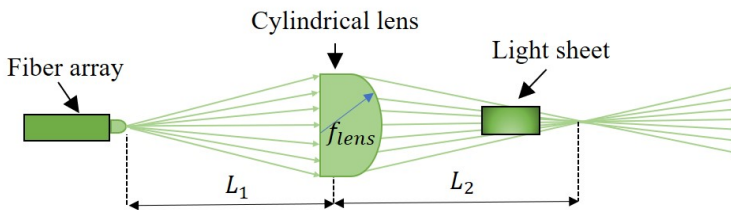
Figure 4.17: Light collimation. L_1 can be adjusted to change L_2 and the average light sheet thickness can be controlled.

Trigger synchronizing: When the camera is triggered in double exposures, the frame rate of the camera can not be controlled accurately, hence one controls the separation time Δt with LED flashes. The LED is triggered in pulses centered on the camera shutter times shown in Figure 4.18, giving image pairs as shown in Figure 4.19. During the two exposures, the particles will receive approximately the same amount of light intensity, and the separation between the triggers are well controlled.
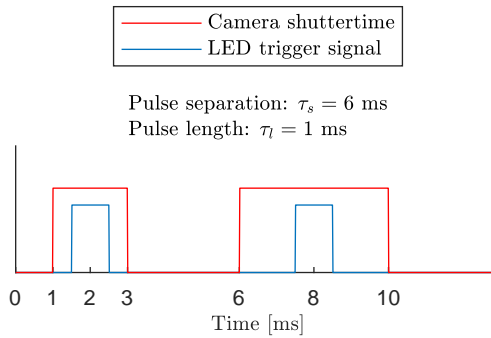

Figure 4.18: Trigger signal for PIV image pairs. To have better control of the pulse separation, the LED is flashed with the same pulse width centered on each shutter time.
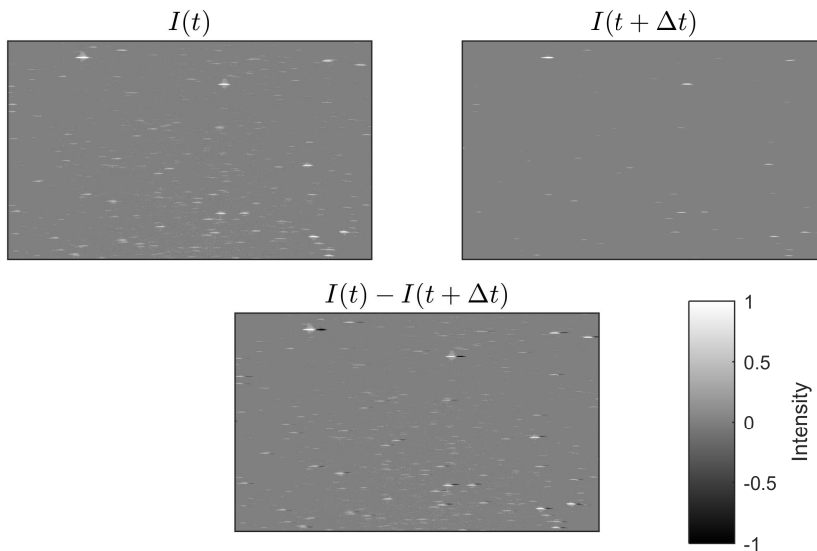
Figure 4.19: Image pair obtained from synchronized triggering of camera and light. Bottom image shows the difference where most particles moves from left to right.

4.3.3 Optical calibration

Pixel pitch calibration: Image coordinates are transformed to physical coordinates by a pixel pitch (p_{pitch}) calculated from an image containing a calibration plate as seen in Figure 4.20.
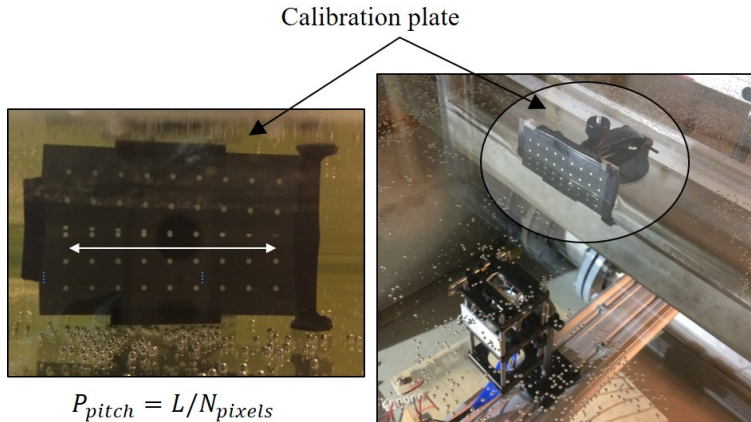

$$P_{pitch} = L/N_{pixels}$$

Figure 4.20: Calibration plate for PIV. A pixel pitch (p_{pitch}) is calculated from a calibration image (left).

Free surface calibration: A challenge is to detect the free surface from single particle images, hence know where to crop. A methods implemented here is to average a number samples leading to higher intensities in the region with particles. Figure 4.21 shows an averaged and a single image where one can clearly see the free surface and bottom, hence crop the image to obtain the measurement area used in DIC.
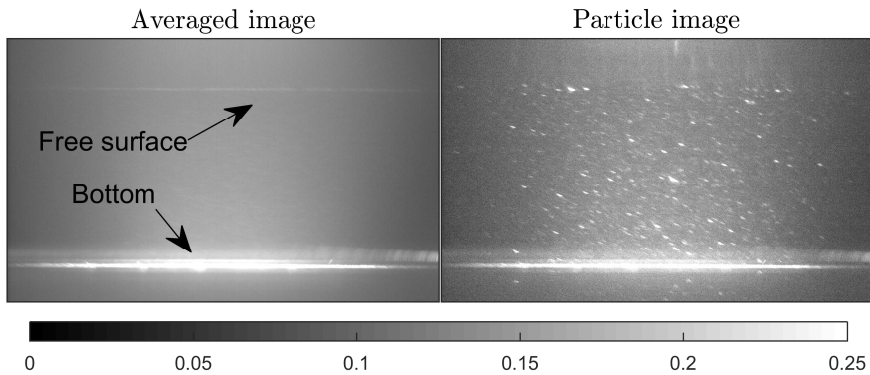
Figure 4.21: Free surface calibration by averaging (left) particle images (right) .

4.4 Flow channel setup and implementation of curved mesh

Flow channel: A flow channel consisting of two tanks connected by a flat plate is constructed, where one side wall and the bottom is transparent for PIV and FS-SS measurements. A centrifugal pump circulates water through a pipe connecting the two basins leading to a flow over the plate, where a diffuser is added to the pipe exit to reduce turbulence in the upstream tank. Figure 4.22 shows a schematic drawing of the flow channel.
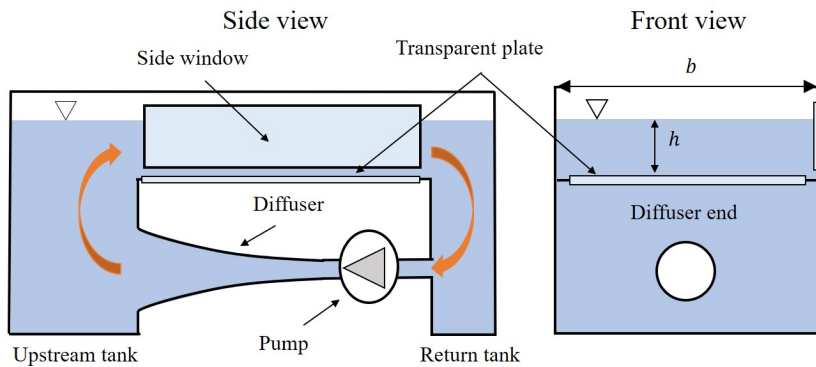

Figure 4.22: Schematic drawing of the tank/pump configuration. The pump circulates water between the two tanks resulting in a flow over the flat plate.

Mesh/Honeycomb structure: To generate a shear flow, a curved mesh is connected between two sets of honeycomb structures shown in Figure 4.23. The flow is laminated by the honeycombs and the streamlines deflected by the curved mesh, resulting in a velocity profile which is depth dependent ($U(z)$).
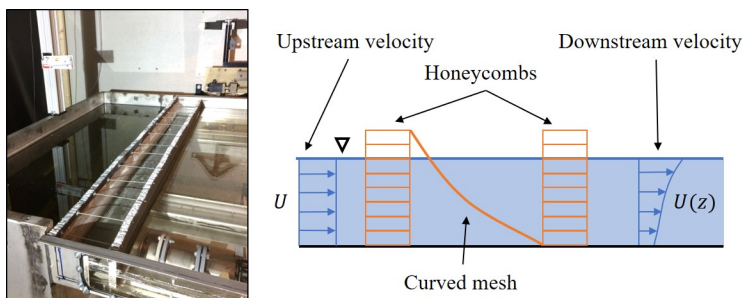

Figure 4.23: Mesh/honeycomb configuration for shear flow generation.

Wall effect: When running the pump at low capacity, it turned out a stagnation phenomenon occurred at the downstream basin leading to a zone of approximately no surface velocity. After measuring the velocity field below this zone, it turned out the velocity was strongly sheared at the surface, and approximately steady and uniform in space, which is ideal for the current inversion experiments.
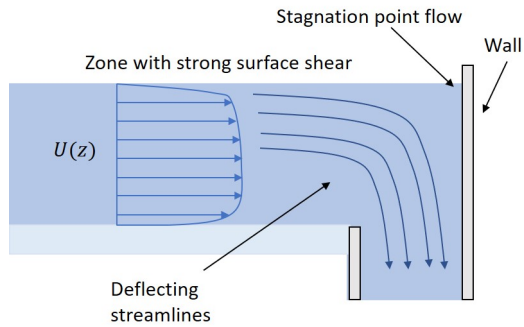

Figure 4.24: Stagnation point flow resulting in zone of strong surface shear.

4.4.1 Parameters and limitations

Suitable flow conditions can be generated by variating the parameters below. The average flow velocity (U) is related to the pump flow rate (Q_{pump}) through Equation 4.4.

$$U = Q_{\text{pump}}/(hb) \tag{4.4}$$

- **Pump capacity:** Controlled by frequency converter which ranges from $25 - 100\%$ of 50 Hz.

- **Water depth** h**:** Along with pump capacity, water depth is chosen such that suitable flow velocity (U) is achieved.

- **Mesh shape:** The mesh curvature is adjusted by changing the distance between the two honeycomb structures.

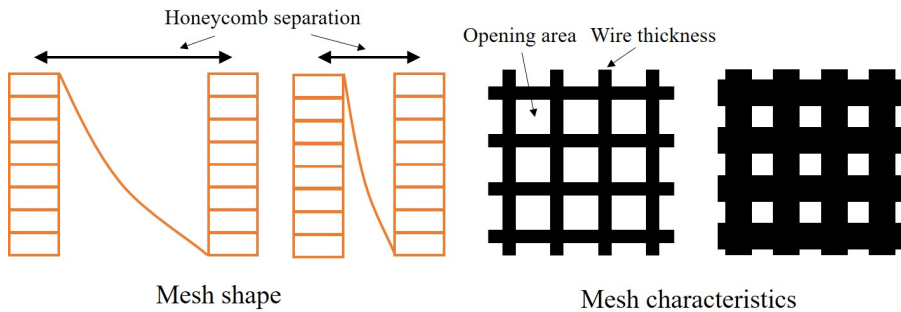- **Mesh size:** The mesh can be changed such that the characteristics are different as seen in Figure 4.25.

Figure 4.25: Honeycomb/mesh characteristics.

4.4.2 Velocity measurements by PIV

Honeycomb/curved mesh section: In the process of implementing a honeycomb/mesh structure, PIV measurements are carried out both with and without the curved mesh between the honeycombs, to verify the theoretical predictions. The measurements are only quantitative and velocities are scaled in pixel units due to no calibration image. However, comparing the two measurements shows that adding a curved mesh results in velocity gradients, roughly linear as predicted by theory.
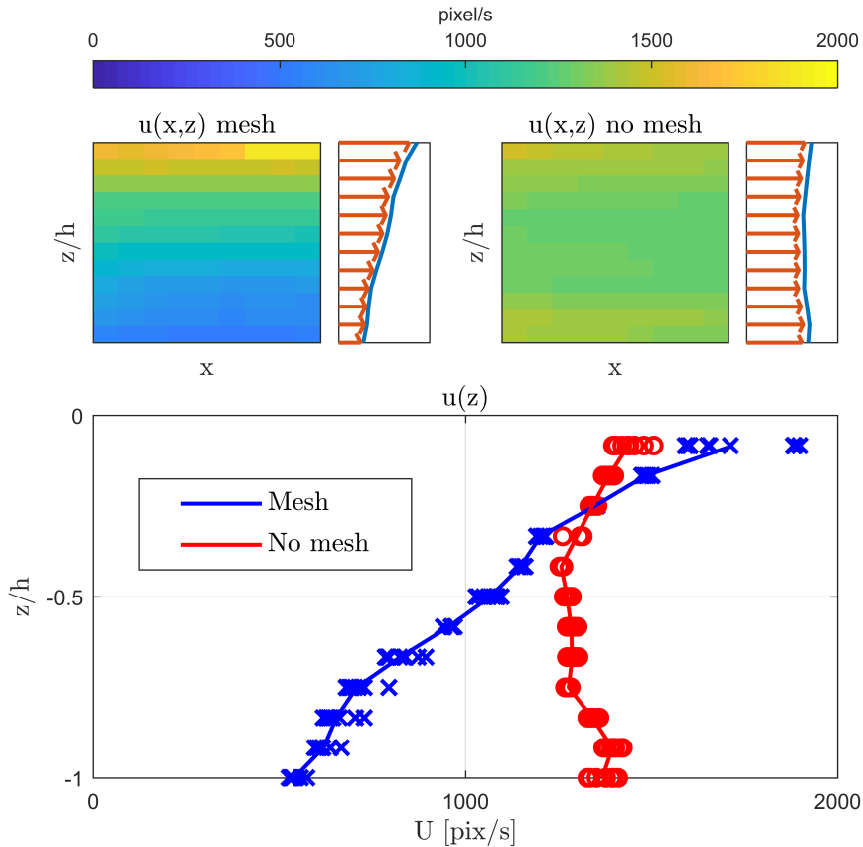

Figure 4.26: PIV measurements of mesh prototype. Velocity field with (left) and without (right) mesh are visualized as both magnitude scaled in colors and as line plots (bottom).

4.5 Implementation of Wave-makers

To perturb the surface two methods are implemented. A pneumatic jet generates a stagnation point pressure on the free surface and a mechanical wavemaker displaces liquid both generating waves as shown in Figure 4.27.
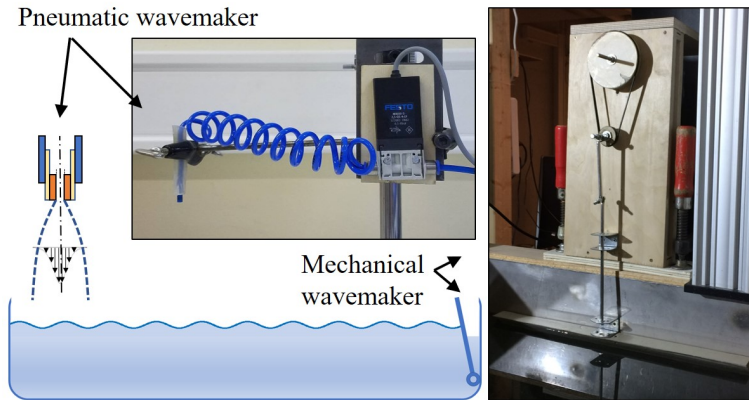

Figure 4.27: Pneumatic wave-maker (left) and mechanical wave-maker (right).

1. **Pneumatic wavemaker:** Waves generated by stagnation pressure on the free surface.

2. **Mechanical wavemaker:** Waves generated by liquid displacement.

4.5.1 Pneumatic wavemaker

Figure 4.28 shows the pneumatic system where air (8bar) is delivered to a regulator where a high-speed electromagnetic valve is controlling the flow through a choked nozzle.

Devices:

- **Regulator:** A regulator determines the back pressure of the system p_0.

- **Choke valve:** A choke valve is adjusted to throttle the flow rate.

- **Magnetic valve:** A magnetic valve is controlled by an electric signal (from a computer) where the forcing frequency (f) is controlled.

- **Nozzle:** A nozzle is added to force choked conditions, where A^* is the throat area.

- **Lab computer:** The trigger signal is sent to the valve from the lab computer.
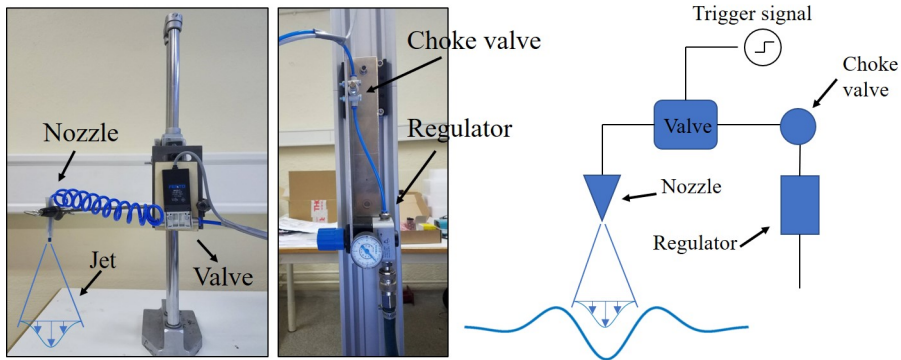
Pneumatic wavemaker

Figure 4.28: Pneumatic system. Air (8bar) is supplied to a regulator where a solenoidal valve is installed to controlled the air flow to a choked nozzle.

Parameters and limitations:

- **Pressure** p_0**:** Nozzle back pressure (p_0) is tuned by the regulator.

- **Distance** L**:** The size ($b = 0.23L$) of the perturbed area is scaled by L.

- **Frequency** f**:** Frequency of the pulse is controlled by the trigger signal sent from the lab computer.

Pressure pulse model: The pressure pulse model derived in subsection 3.4.1, is used to model the pneumatic disturbance as an applied pressure source.

$$p(r, L) \approx 20.25 p_0 \frac{C_d A^*}{L^2} \text{sech}^4 (10.4 \frac{r}{L}) \qquad b(L) \approx 0.23L \qquad (4.5)$$

Stagnation pressure measurements:

To verify that the approximated model above is valid, stagnation point measurements were carried out at different positions in the jet using a static pitot tube and a differential pressure sensor. The experimental setup is shown in Figure 4.29 where, $D = 0.7$mm and $C_d \approx 0.6$ which is the discharge coefficient for an orifice[1].

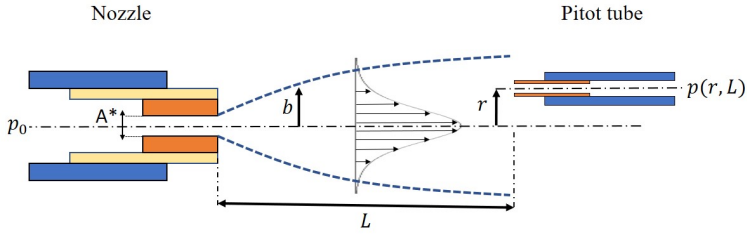[1]http://www.aft.com/documents/AFT-Modeling-Choked-Flow-Through-Orifice.pdf

Figure 4.29: Geometry and setup for jet measurements.

Figure 4.30 shows the experimental results compared to the model for both the normalized center line pressure $(p(0, L)/p_0)$, and the normalized shape $p(r, L)/p(0, L)$, which both show agreement with the model both regarding to shape and amplitude.
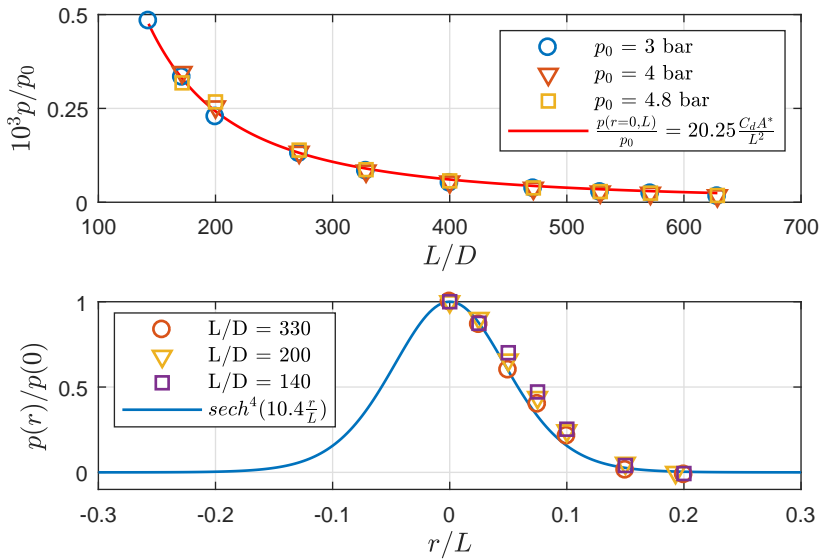

Figure 4.30: $p(0, L)/p_0$ (top) for different p_0 and $p(r, L)/p(0, L)$ (bottom) for different L.

4.5.2 Mechanical Wavemaker

To generate long wavelengths, a mechanical wave-maker powered by a synchronous motor is designed (Figure 4.31) and implemented, where the displacement shape is chosen to be curved in order to generate low amplitudes.
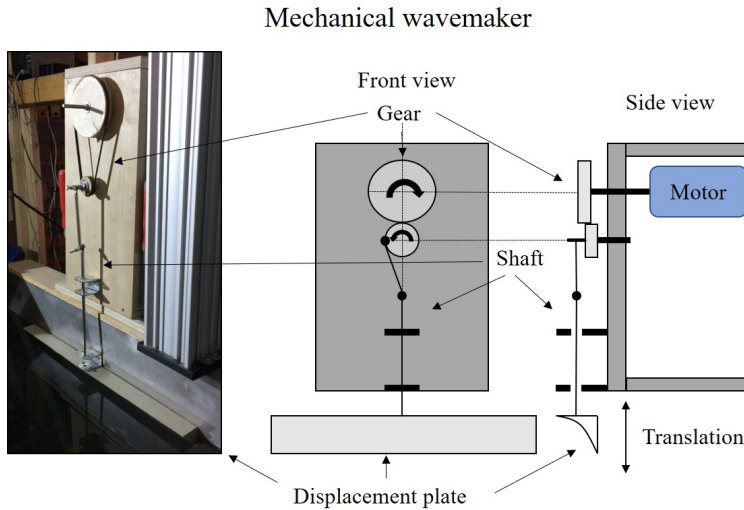

Figure 4.31: Mechanical wave-maker. A synchronous motor is powering a crank shaft mechanism translating a displacement wave-maker.

Devices:

- **Synchronous electric motor:** A synchronous motor is powering a shaft connected to a gearbox, rotating a crankshaft mechanism.

- **Gear box and crankshaft mechanism:** A mechanical mechanism (gear, crank shaft) is periodically translating a shaft with stroke length (S) and frequency f.

- **Displacement profile:** A displacement profile is attached at the end of the translating rod.

- **Control circuit:** Frequency (f) is controlled by regulating the motor voltage.

Parameters and limitation

- **Motor voltage V_{in}:** The rpm determining the frequency is controlled by tuning the motor voltage.

- **Stroke length S:** Stroke length (S) can be tuned by changing the radius of the crankshaft.

Chapter 5

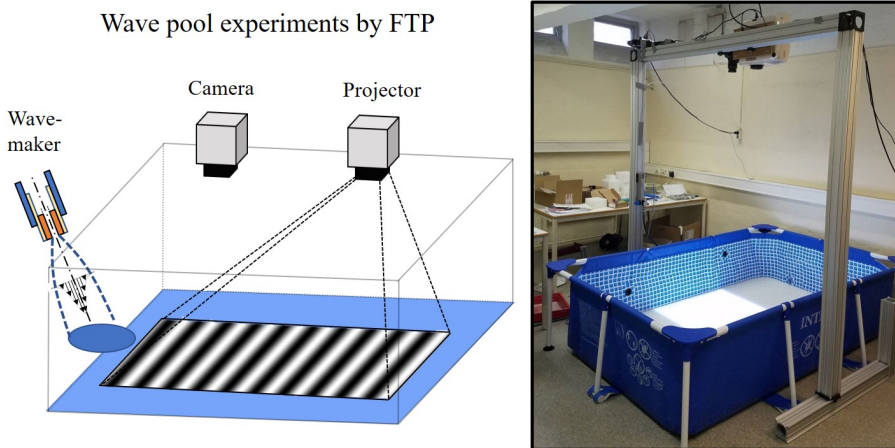# Wave pool experiments of waves using FTP

Figure 5.1: Experimental setup for FTP measurements of waves in a wave pool configuration.

FTP is tested to measure the free surface height $(h(x, y, t))$ in quiescent waters, where damping experiments and dispersion is measured and compared to wave theory.

1. **Damping and fringe contrast experiments:** Damping rates measured at different concentrations of titanium dioxide (TiO_2) and signal noise ratios (SNR) are calculated to measure the effect of adding contrast pigment to the water.

2. **Initial value problem:** Time evolution of ring waves generated by dropping an object and a droplet is measured and compared to a Gaussian shaped initial value model.

Symbols used in Contrast/damping experiments

h	Surface height	σ_I	Amplitude gray scale intensity
A	Average amplitude	σ_e	Standard deviation of gray scale intensity
t	Time		
T	Damping time constant	c_i	Pigment concentration
β	Damping coefficient	d_i	Water depth
(a, c)	Damping model parameters	α_i	Optical parameter for FTP
(N_x, N_y)	Number of image pixels	D_i	Camera projector distance
I	Gray scale intensity image	L_i	Projector reference surface distance

Symbols used in Ring waves measured by FTP

h	Surface height and water depth	g	Gravitational constant
ζ	Surface height from wave theory	σ	Surface tension water
F	Spectral phase and amplitude	ρ	Water density
t	Time		
k	Wave-number	α	Optical parameter for FTP
a	Initial width of Gaussian shape	D	Camera projector distance
ζ_0	Initial amplitude of Gaussian shape	L	Projector reference surface
ω	Angular velocity	P	Physical wave-length fringe pattern
J	Bessel Function of the First Kind	f	Camera frame rate

5.1 Contrast/damping experiments

Objectives: To use FTP, contrast pigments have to be added to the liquid, which might impose changes in fluid properties ultimately affecting measurements. Understanding these effects is essential to draw conclusions based on measurements where pigments are added, and it is useful to obtain knowledge about the amount of concentration needed to obtain good contrast levels.

Experimental outline: In this experiment titanium dioxide (TiO_2) is added as contrast pigment and contrast level and damping are measured at different concentration levels.

1. Waves are generated by wave-makers.

2. $h(x, y, t)$ is measured by FTP as the waves are damped.

3. $A(T)$ is modeled as a decaying exponential (both defined in Equation 5.1), and a damping coefficient (β) is extracted.

4. Signal noise ratio (SNR) is calculated (Equation 5.2) based on the reference image representing the quality the contrast levels.
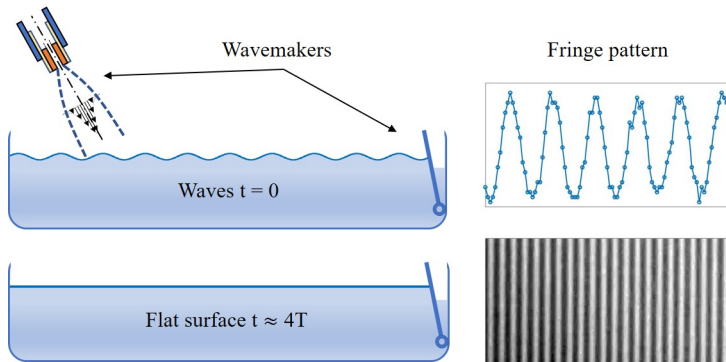

Figure 5.2: Experimental setup for damping/contrast experiments (left). SRN is calculated from N samples of the reference surface (right).

Damping models: An exponential model is chosen to look at the decaying trend for the average amplitude $(A(t))$, where model parameters (a, β, c) is extracted and compared. β determines the damping rate and a time constant $(T = 1/\beta)$ determines the time for $A(t)$ to be reduced by a factor of e^{-1}. a and c is added to compensate for a constant amplitude caused by noise.

$$A(t) = \left[\frac{1}{NxNy} \sum_{i=1}^{Nx} \sum_{j=1}^{Ny} h(x_i, y_j, t)^2 \right]^{0.5} \qquad \frac{A(t)}{a} = e^{-\beta t} + c \qquad (5.1)$$

Contrast levels and Signal Noise Ratio: The constant noise contributing to a steady amplitude is the result of high SNR values (defined in Equation 5.2), which is the ratio of the signal amplitude (σ_I) and the noise RMS (σ_e). $\sigma_e(x, y)$ is calculated based on the time variation of gray scale level measured in each pixel over N samples of a reference surface ($h(x, y) = 0$) and σ_e is the average value of $\sigma_e(x, y)$. σ_I is approximated from the variance of intensity within each image.

$$\sigma_I = \sqrt{2}\mathrm{Var}[I(x, y, t)] \qquad \sigma_e = \left[\frac{1}{N}\sum_{i=1}^{N}\left(I_i - \bar{I}\right)^2\right]^{0.5} \qquad \mathrm{SNR} = \frac{\sigma_I}{\sigma_e} \qquad (5.2)$$
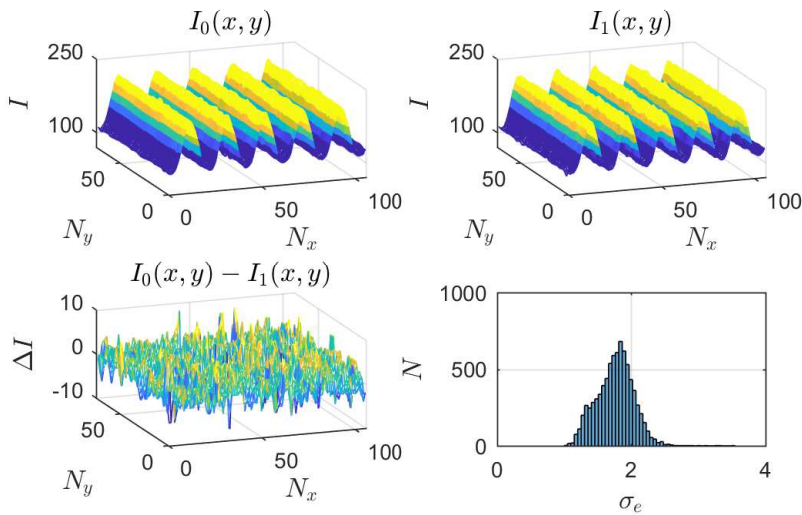

Figure 5.3: Two samples (top) of reference images, where the intensity is variation over time (bottom left) and the average standard deviation of the variation determines σ_e (bottom right).

Figure 5.3 shows grayscale intensities $I_i(x, y)$ for two reference images samples where ΔI shows pixel variation due to noise. The histogram shows the distribution $\sigma_e(x, y)$, which seem to be roughly distributed around a mean which should be a good estimator for σ_e.

5.1.1   Setup and parameters

Water-soluble paint as compromise: A bottle containing $0.5\,l$ of paint is added to the pool along with $480\,l$ liters of water, resulting in an initial concentration $c \sim 0.1\,\%$. In these experiments, the order of titanium dioxide had not arrived and paint containing the pigment was used as a compromise. The reduction in concentration was done by adding water to the pool changing the depth (h_i) for each concentration and Optical parameters are calibrated each time shown in Table 5.1. A video is taken capturing the reference surface where 100 sample images are used to calculate SNR values.

Parameters:

- **Concentration** c_i**:** Amount of pigment measured in $[\%]$ of initial concentration.

- **Water depth** h_i**:** Pool depth (h_i) is the water depth which is changed to reduce the concentration.

- **Contrast level** σ_I**:** Is the average amplitude extracted from all the reference images.

- **RMS noise** σ_e**:** Is the average standard deviation of the gray scale intensity variation over samples of reference images.

- **Signal Noise Ratio (SNR):** Fraction of contrast level and RMS noise.

Parameter	i = 1	i = 2	i = 3
c_i	0.1 [%]	0.05 [%]	0.035 [%]
d_i	80.6 [mm]	161.2 [mm]	240 [mm]
α_i	1.750 [-]	2.226 [-]	2.195 [-]
D_i	1169 [mm]	830 [mm]	795 [mm]
L_i	2045 [mm]	1849 [mm]	1746 [mm]

Table 5.1: Parameters for damping/contrast experiments.

Wave-makers: Both pneumatic and mechanical wave-makers are used to generate waves. However, the mechanical wave-maker used in these experiments was a preliminary version of the one shown in section 4.5, and the operational conditions were not as controllable in terms of stroke length and periodicity.

5.1.2 Results

Table 5.2 shows the extracted model coefficients (β, a, c), where Figure 5.6 shows both experimental points and the model. A Gaussian model seems to be an appropriate choice to model the decaying behavior.

	Concentration	β	a	c
	100	0.03761	8.067	0.8734
Mechanical	50	0.02321	15.98	0.4693
	33	0.01424	12.88	0.9065
	100	0.1591	0.5297	0.2273
Pneumatic	50	0.1448	1.712	0.393
	33	0.1238	1.262	1.149

Table 5.2: Fitted parameters for $A(t)/A(0)$.
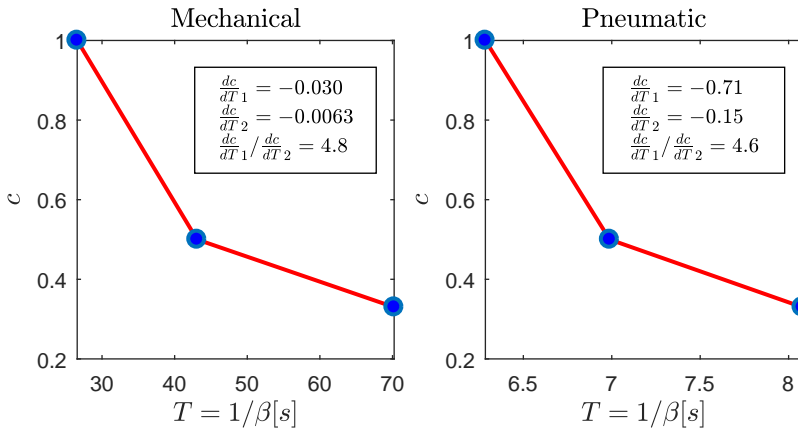
Figure 5.4: Time constants (T) for both mechanical (left) and pneumatic (right) wavemakers, where dc/dT is calculated to compare trends between the two cases.

Figure 5.4 shows the time constant (T) at different concentrations (c_i), where $dc/dT_{(1,2)}$ is the gradient in the two intervals. $\frac{dc}{dT_1} / \frac{dc}{dT_2}$ is the relative change in gradient between the two intervals, which is calculated to compare trends. The experimental data and fitted curves for $A(t)$ can be found in appendix B as Figure 5.6.
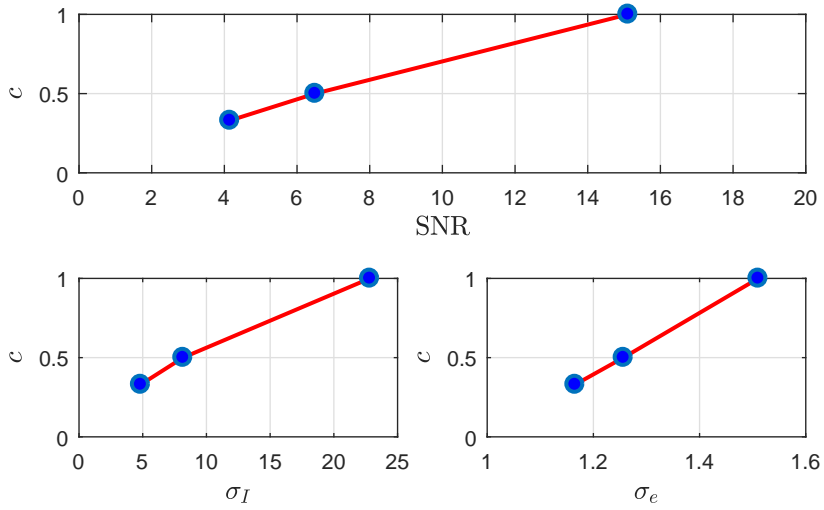
Figure 5.5: SNR (top), contrast levels (bottom left), and RMS noise (bottom right) for different concentrations of (TiO_2).

Figure 5.5 shows the the contrast calculations where $(\sigma_e, \sigma_I, SNR)$ is plotted against concentration. Both contrast level (σ_I) and the noise (σ_e) reduces along with reduced concentration. However, the SNR also reduces indicating that noise is more be more significant which seem to be visible in the experimental data shown in Figure 5.6.
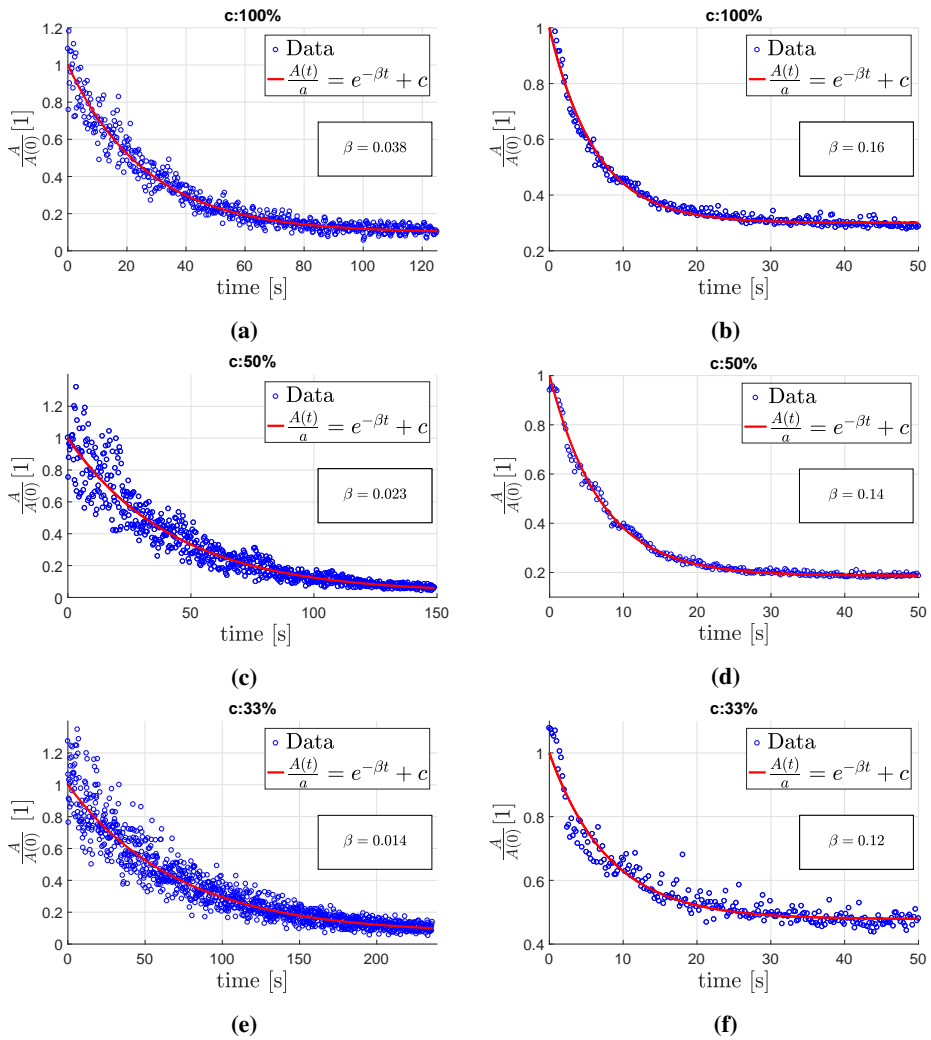
Figure 5.6: Experimental data and fitted model for damping experiments. $A(t)/A(0)$ decays in time and β determines damping rates for the mechanical (left) and pneumatic (right) wavemakers.

5.1.3   Discussion

Contrast levels and SNR: Both noise levels and contrast amplitude reduces with less concentration of pigments. However, the SNR also reduces meaning that higher concentrations of pigments lead to better quality images. Contrast levels obtained by these concentrations were still poor and ($\sigma_I = 25$) and exploring other types of pigment as a replacement might be the way to progress if one wants better quality FTP data.

Damping experiments: The results from the damping experiments shows a similar reducing trend, both for large and small waves at a lower concentration of paint. This might imply that the parameters changed from different concentration affects both large and small waves similarly. However, due to the change of water depth along with concentration, it is impossible to conclude if the reduction in damping is due to the concentration of pigment, or change in boundary conditions.

- **Water depth:** One would expect the change of water depth to affect boundary conditions for large waves more than small waves both due to reduced bottom effects and reduced flexible wall effects, which is not the case.

- **Change of concentration:** Since the trend seems to be reducing with similar magnitude for both cases, it might seem that the paint increases damping properties. However, it is hard to draw any conclusions on the absolute effects and new experiments in a better controlled environment is needed to answer that question.

5.2 Ring waves measured by FTP

Objectives: FTP is used to measure ring waves generated on the free surface. The reconstructed surface is compared to a scaled Gaussian initial shape calculated from theory (section 2.6), and the spectral magnitude of the experimental data is compared to the linear dispersion relation. The motivation is to see if the method can reproduce linear waves in quiescent waters to test if the method can provide reliable dispersion data.

- Compare reconstructed surface ($h(x, y, t)$) to a scaled Gaussian initial shape $\zeta(x, y, t)$.

- Compare spectral magnitude ($F(\omega, \mathbf{k})$) to linear dispersion relation

The ring waves are triggered by 1. droplet hitting the surface and 2. small metal object dropped into the basin (shown in Figure 5.7). $h(x, y, t)$ is calculated and compared visually to the classical Gaussian initial shape (shown in Figure 5.8) in quiescent waters.

Experimental outline:

1. $h(x, y, t)$ is calculated from images and compared with $\zeta(x, y, t)$ from linear wave theory

2. $F(\omega, k_x, k_y)$ is calculated from experimental data and compared to linear dispersion relation $\omega(\mathbf{k})$.
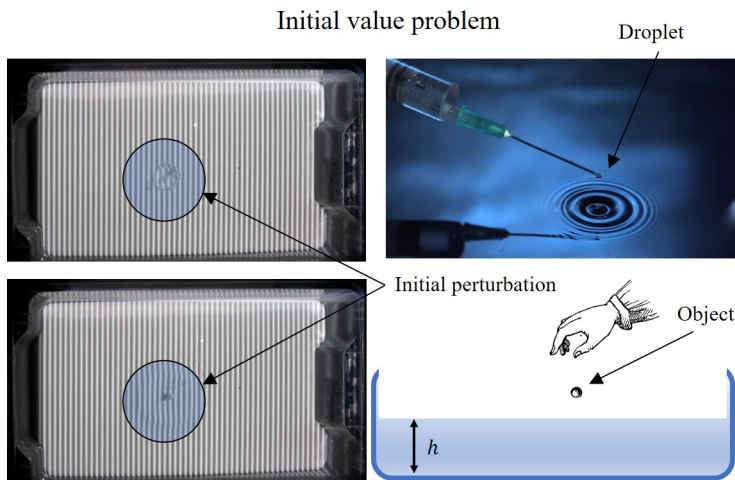

Figure 5.7: Sample images recorded by the camera (left) and images showing triggering of ring waves (right) [1].

---

[1] https://ak3.picdn.net/shutterstock/videos/3352358/thumb/9.jpg?i10c= img.resize(height:160)

- **Case1 Washer:** A small metal ring (washer) is dropped in the basin.

- **Case2 Water droplet:** A syringe is used to let a droplet of water hit the free surface.

$$\zeta(r,t) = \zeta_0 a^2 \int_0^\infty k e^{-\frac{k^2 a^2}{2}} J_0(kr) \cos{(\omega t)} dk \tag{5.3a}$$

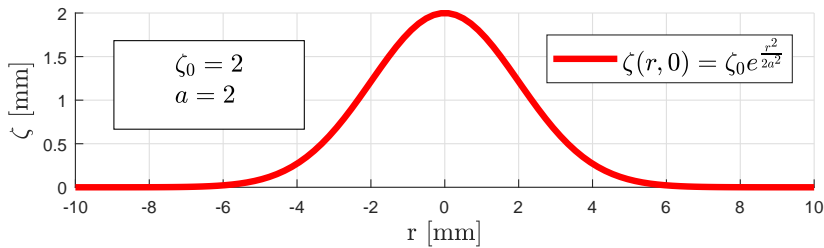$$\omega = \sqrt{k(g + \frac{\sigma}{\rho} k^2) \tanh{(hk)}} \tag{5.3b}$$

Figure 5.8: Gaussian initial shape. a determines the width and ζ_0 determines the height of the shape.

Gaussian scaling: The shape of the deformed surface caused by the objects is unknown. Therefore, ζ_0 and a, which determines the height and width of the initial shape, is scaled to roughly fit the waves measured experimentally. In addition the the spectra $(F(\omega, k_x, k_y))$ is calculated and visualized in the frequency domain, where energy should be centered on the linear dispersion relation line $(\omega(\mathbf{k}))$.

5.2.1 Setup and parameters

Optical and physical parameters used in the experiments are listed in Table 5.3. Fluid properties are taken for pure water and might differ from the water/paint solution. However, the differences seemed insignificant with exception of surface tension, which only affects capillary dispersion ($k > 369$ 1/m).

Symbol	Value	Unit
α	3.142	[-]
D	389	[mm]
L	1221	[mm]
P	12.7	[mm]
h	14	[mm]
ρ	1000	[kg/m^3]
σ	0.072	[N/m]
g	9.81	[m/s^2]

Table 5.3: Calibrated parameters (top) and fluid properties (bottom).

Table 5.4 show the scaling parameters for the Gaussian initial shapes. The model describing the dropped object required both a higher and broader initial shape than the model describing the droplet.

Washer		Droplet	
ζ_0	a	ζ_0	a
-20[mm]	30[mm]	-12[mm]	7[mm]

Table 5.4: Scaling parameters for the Gaussian initial shape.

Limitations FTP:

1. **Wavenumber** (k): $k_{\max} = (2\pi/P)d$, where d is the filter width (signal processing parameter).

2. **Frequency** (ω): $\omega_{\max}/2\pi = f/2 = 12.5$ Hz, where $(f = 25\text{fps})$ is the frame rate.

5.2.2 Results

Washer:

Snapsshots: Snapshots of $h(x, y, t)$ both for reconstructed and modeled surfaces are shown in Figure 5.9,Figure 5.10, Figure 5.11.
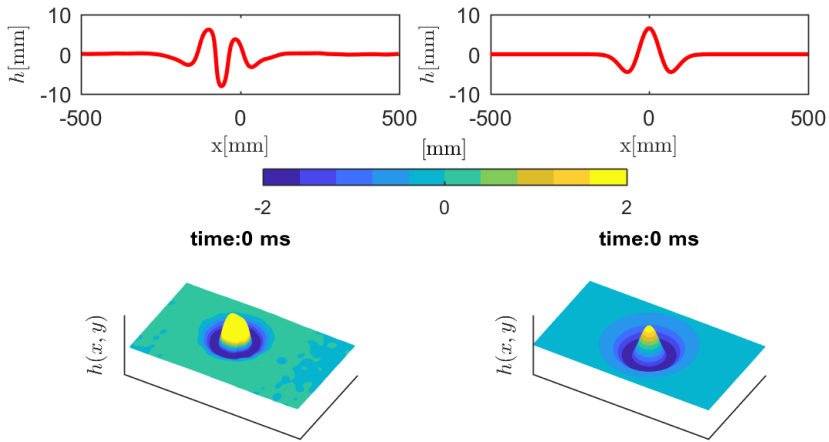

Figure 5.9: Snapshot of experimental (left) and analytic (right) $h(x, y)$ for the washer drop at t = 0ms
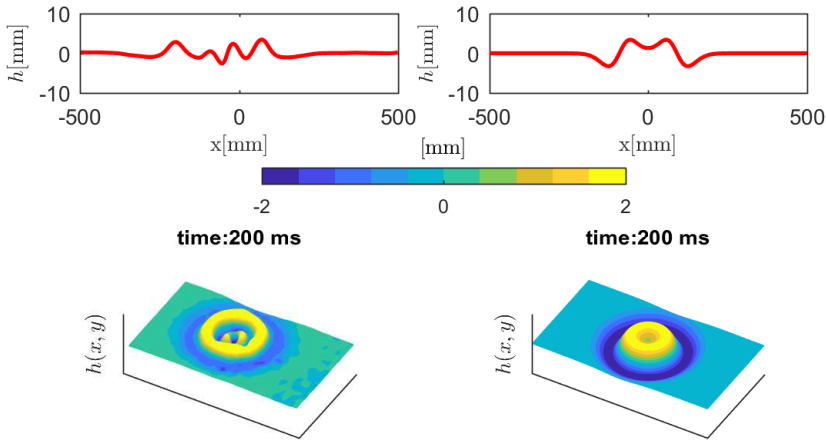
Figure 5.10: Snapshot of experimental (left) and analytic (right) $h(x, y)$ for the washer drop at t = 200 ms
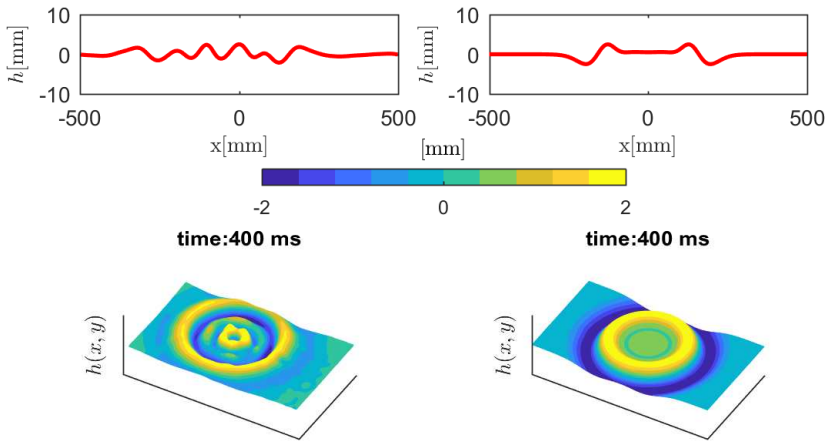

Figure 5.11: Snapshot of experimental (left) and analytic (right) $h(x, y)$ for the washer drop at t = 400 ms

Snapshots (Figure 5.9,Figure 5.10, Figure 5.11) of $h(x, y, t)$ from FTP and numerical simulation (Equation 5.3a) are visualized as a surface (bottom), where color represents magnitude in mm, and as lines plotted through the center of the initial perturbation $(h(x, y = 0, t))$.

Spectral magnitude: Figure 5.12 shows spectral magnitude $F(\omega, k_x, k_y)$ calculated from $h(x, y, t)$, where the magnitude of F is visualized as colors in decibels. The two middle figures shows F visualized in the (k_x, ω) plane, while the top and bottom figures are F visualized in the (k_x, k_y) plane.
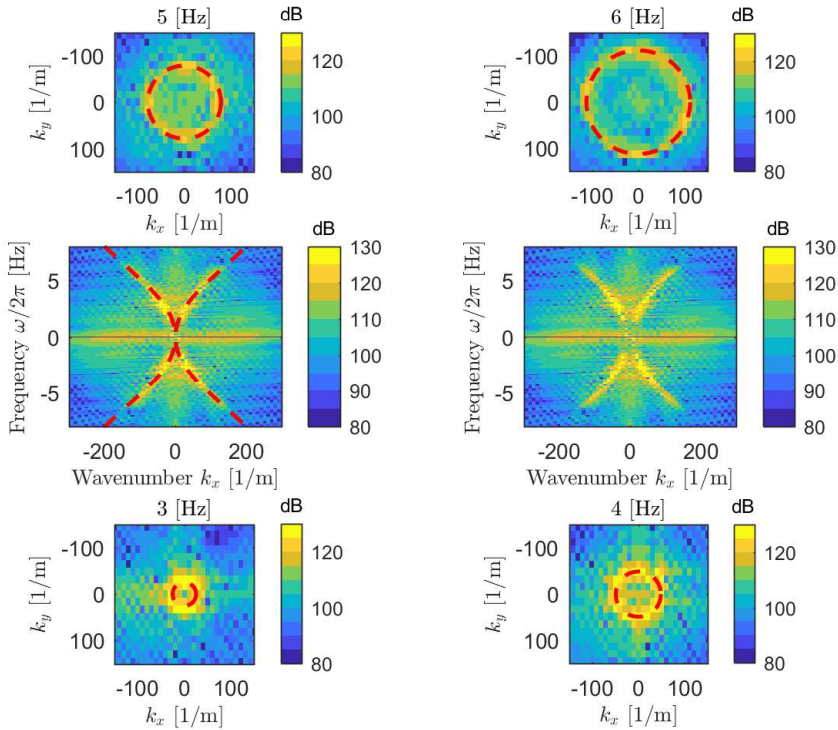

Figure 5.12: Magnitude of $F(\omega, k_x, k_y)$ visualized in a selection of 2D planes, where the linear dispersion line (red) is added.
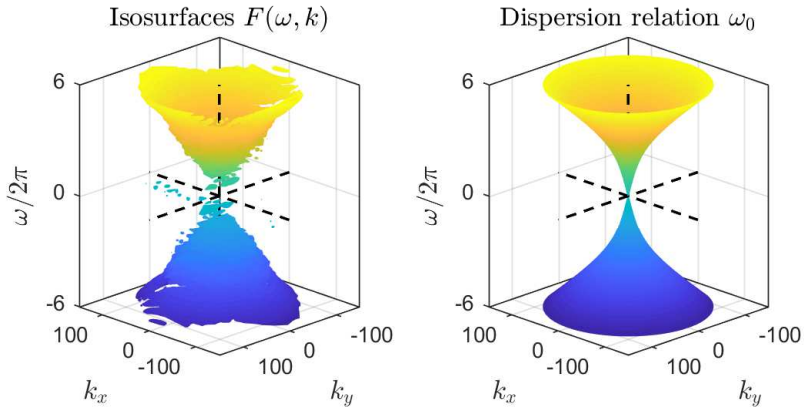
Figure 5.13: Isosurfaces from dispersion relation data(left) and the linear dispersion relation visualized as a surface(right).

Isosurfaces where $(120 < F < 130)$ are extracted from Figure 5.12 and visualized as a surface in the (ω, k_x, k_y) plane and compared to the linear dispersion relation $(\omega_0(k_x, k_y))$ (Figure 5.13).

Droplet:

Snapsshots: Snapshots of $h(x, y, t)$ both for reconstructed and modeled surfaces are shown in Figure 5.14, Figure 5.15, Figure 5.16.
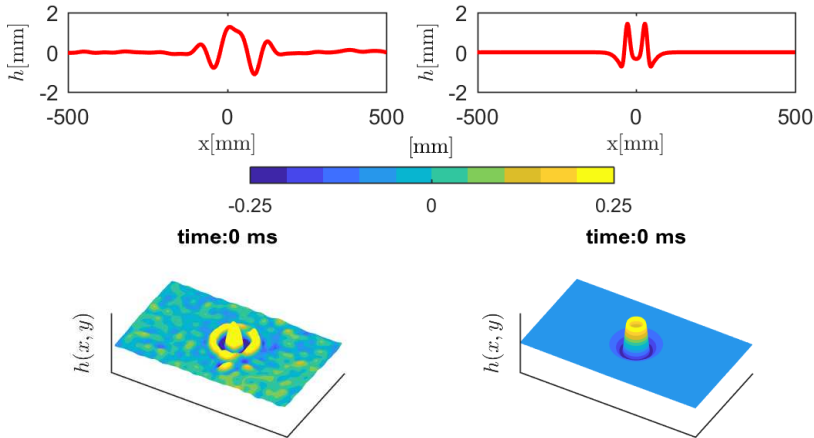

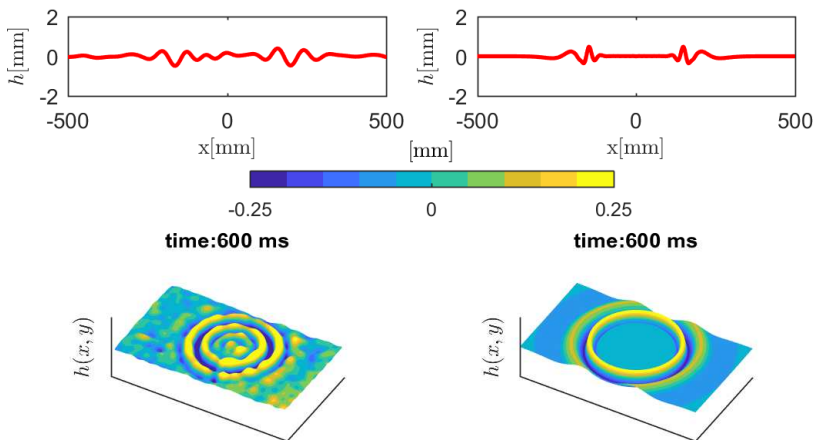**Figure 5.14:** Snapshot of experimental (left) and analytic (right) $h(x, y)$ for the droplet at t 0ms.

Figure 5.15: Snapshot of experimental (left) and analytic (right) $h(x, y)$ for the droplet at t = 600 ms.
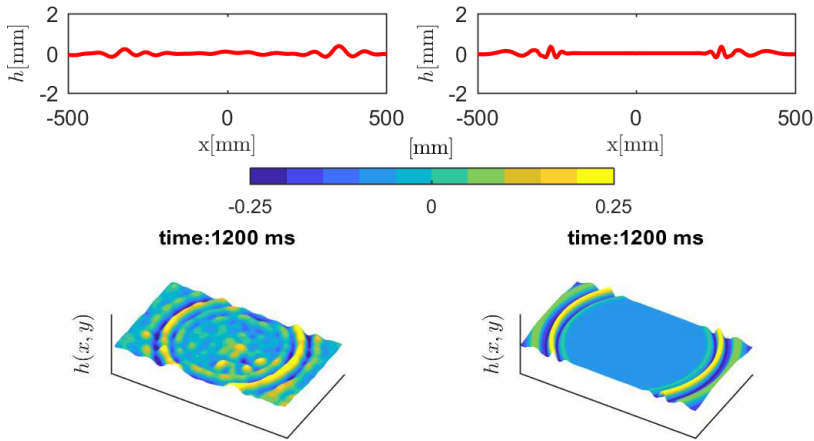
Figure 5.16: Snapshot of experimental (left) and analytic (right) $h(x, y)$ for the droplet at t 1200 ms.

Snapshots (Figure 5.14, Figure 5.15, Figure 5.16) of $h(x, y, t)$ from FTP and numerical simulation (Equation 5.3a) are visualized as a surface (bottom), where color represents magnitude in mm, and as lines plotted through the center of the initial perturbation $(h(x, y = 0, t))$.

Spectral magnitude: Figure 5.17 shows spectral magnitude $F(\omega, k_x, k_y)$ calculated from $h(x, y, t)$, where the magnitude of F is visualized as colors in decibels. The two middle figures shows F visualized in the (k_x, ω) plane, while the top and bottom figures are F visualized in the (k_x, k_y) plane. Note that the magnitude of F drops rapidly for $k > 300$, which is due to the limitation of FTP, where $F(k > 300)$ are filtered out in the signal processing.
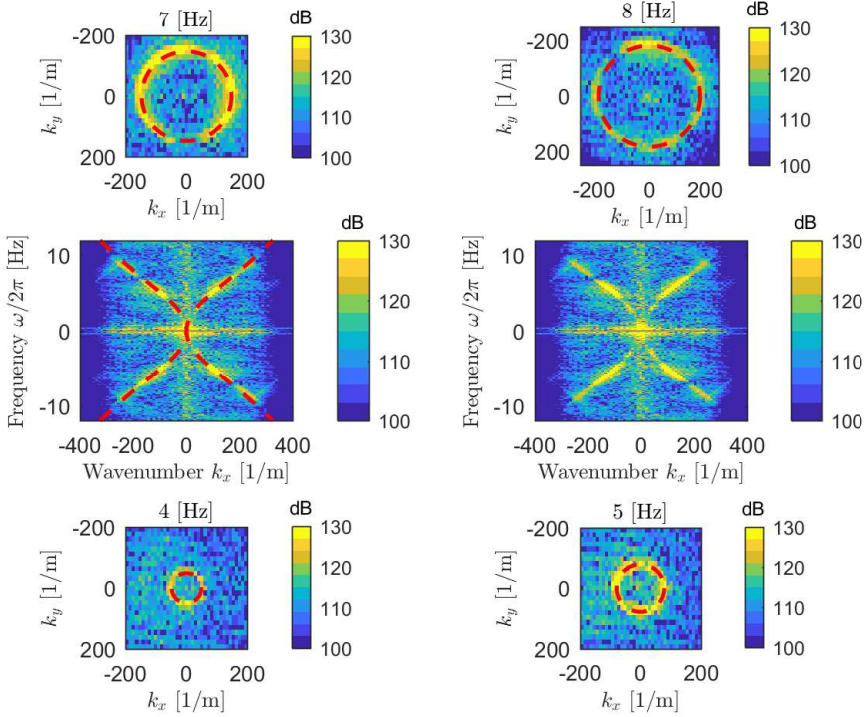

Figure 5.17: Magnitude of $F(\omega, k_x, k_y)$ visualized in several 2D planes for droplet data. $d = 0.6 \rightarrow k_{\text{max}} \approx 300$ 1/m.
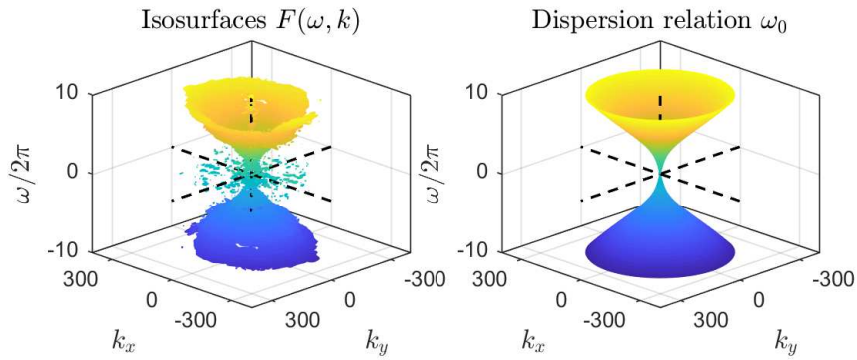
Figure 5.18: Isosurfaces from dispersion relation data (left) and the linear dispersion relation visualized as a surface (right).

Isosurfaces where $(120 < F < 130)$ are extracted from Figure 5.17 and visualized as a surface in the (ω, k_x, k_y) plane and compared to the linear dispersion relation $(\omega_0(k_x, k_y))$ (Figure 5.18).

5.2.3 Discussion

Model representation of experiments: Scaling a Gaussian initial shape gives a rough reproduction of the propagating ring waves generated in both cases. However, the physical initial conditions differ from the experiments and accurate comparisons are hard to obtain.

Initial conditions:

- **Mass conservation:** An initial shape contains extra mass, which might be unequal to the mass introduced by the suppressed volume caused by the objects.

- **Initial momentum:** The falling objects have initial velocity corresponding to initial momentum, which is not addressed in the Gaussian model used in these experiments.

Boundary conditions:

- **Reflecting walls:** The experiments were carried out in a container with reflecting walls, which is different from the Gaussian model, which is modeled as a hyperbolic system where the domain extends to infinity.

Dispersion data (F)**:** The best way of confirming physical measurements is to calculate and compare the dispersion data $F(\omega, k_x, k_y)$, which is in good correlation with linear theory $(\omega_0(\mathbf{k}))$.

FTP for free surface measurements: FTP seems to reproduce the free surface evolution accurately and dispersion data is centered on the linear dispersion relation, according to theory. However, because of a small measurement area, the spectral resolution is poor with respect to spatial coordinates (k_x, k_y), and spectral leakage is introducing a source of error..

- Limitations: The spatial wave-number restriction predicted by theory is confirmed in these experiments and shorter wavelengths than the fringe pattern are filtered.

- Noise: There is noise due to variation in contrast levels caused by pigment sedimentation.

Chapter 6

Flow tank experiments of waves and currents using FS-SS and PIV.

Objectives: This section is dedicated to the experimental setup shown in Figure 6.1, where FS-SS, PIV, wave-makers, and curved mesh implementations are combined to measure wave phenomena in the flow tank. Surface gradient $(\nabla h(x, y, t))$ and surface height $(h(x, y, t))$ is reconstructed using FS-SS for waves propagating on currents and in quiescent waters where PIV is used to measure velocities. All waves are generated by either the pneumatic or mechanical wave-maker.

1. **Ring and ship waves in quiescent waters:** Quantitative measurements of ring and ship waves in quiescent waters is presented. Dispersion data is also extracted from spectral analysis and compared to the linear dispersion relation.

2. **Nonlinear waves**: Plane Non-linear waves generated by the pneumatic wave-maker are examined where steepness is calculated both from spectral analysis and from estimation in the spatial domain.

3. **Current inversion:** Spectograms are generated by analyzing windows of waves generated by both pneumatic and mechanical wave-makers propagating on currents. Thereafter, the dispersion data is used to reconstruct current profiles, which are compared to direct flow measurements by PIV.
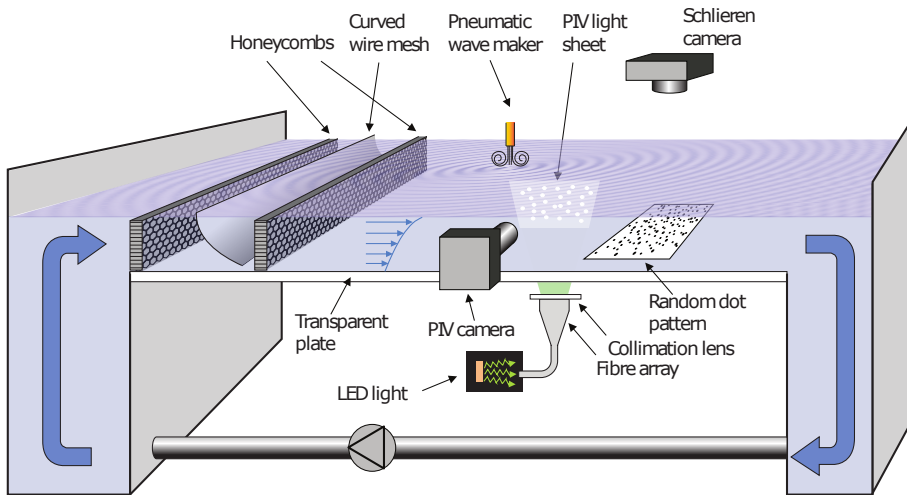
Figure 6.1: Experimental setup current inversion experiments, where experimental methods presented in chapter 4 are combined to study waves propagating on currents (fig. by S.Å.E)

- **Flow conditions:** Flow tank setup.

- **Waves:** Generated by pneumatic and mechanical wavemakers.

- **Surface topology**: Measured by FS-SS.

- **Velocity field:** Measured by PIV.

Symbols used in Ring and ship waves measured by FS-SS

∇h	Surface gradient from FS-SS	L	Ship length
h	Surface height from FS-SS and water depth	U	Ship speed
h_p	Perplex thickness	d	Pulse width / initial perturbation width
h_a	Air gap distance		
ρ	Fluid density	F	Spectral magnitude
g	Gravitational constant	ω	Angular velocity distance

Symbols used in Nonlinear waves

∇h	Surface gradient from FS-SS	ka	Steepness parameter
h	Surface height from FS-SS and water depth	ω	Angular velocity distance
		N	Number of samples
h_a	Air gap distance	f_0	Sampling rate/camera frame rate
ρ	Fluid density	F	Spectral magnitude
g	Gravitational constant	k	Wave-number

Symbols used in Current inversion from dispersion data and PIV measurements

∇h	Surface gradient from FS-SS	ω	Angular velocity distance
h	Surface height from FS-SS and water depth	ψ	Stream function
		t	Time
h_a	Air gap distance	k	Wave-number
U	Flow velocity	ϵ	Residual

6.1 Ring and ship waves measured by FS-SS

Objectives: FS-SS for surface reconstruction is tested through measurements of linear wave phenomenon in quiescent waters, where both the wake generated by dragging a rod across the surface, and ring waves formed by a droplet impact, are considered. Measurements are compared quantitative to models calculated from the impulse response formulation (section 2.6), and the spectral quantities are calculated.

- Ring waves by droplet and pressure pulse
- Ship wake by translating rod
- Spectral analysis of plane waves for dispersion

6.1.1 Procedure

Initial perturbations are generated by dropping a water droplet impacting the surface and triggering a single pressure pulse. The ship wakes are generated by dragging a metal rod across the domain. The surface topology $(\nabla h, h)$ is measured and reconstructed by FS-SS, and compared to numerical models based on a pressure impulse response (section 2.6).
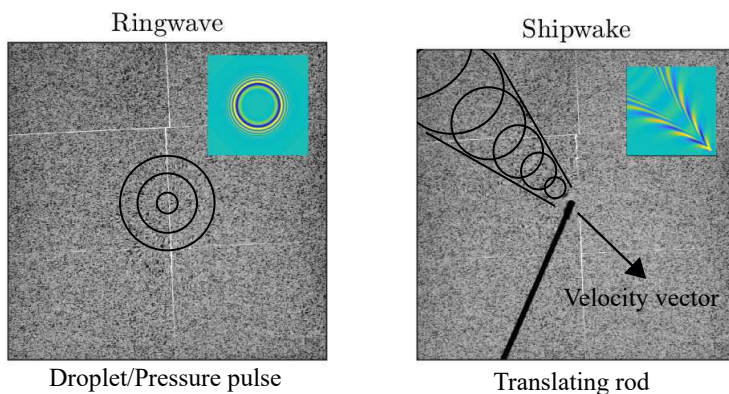

Figure 6.2: Single impulse impact (left), and ship-wake behind translating object (right)

1. Generate wave pattern.

2. Measure ∇h and h.

3. Estimate initial conditions and compare with theory (impulse response).

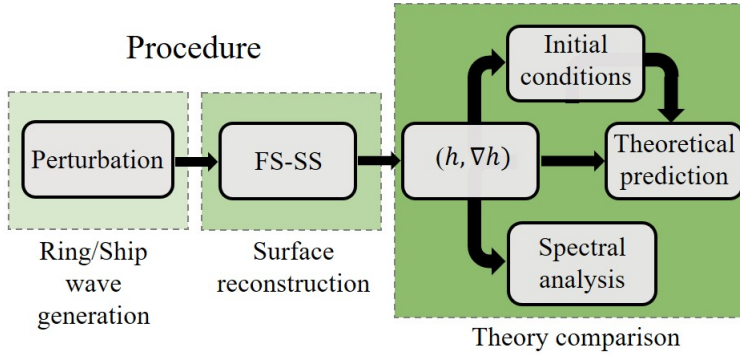4. Calculate dispersion data and compare with linear dispersion relation.

Figure 6.3: Experimental procedure.

6.1.2 Parameters

Table 6.1 contains the optical lengths used in FS-SS and fluid properties for water.

Symbol	Value	Unit
h	0.035	[m]
h_a	0	[m]
ρ	1000	[kg/m^3]
σ	0.072	[N/m]
g	9.81	[m/s^2]

Table 6.1: Optical parameters for FS-SS (top), and fluid properties(bottom)

Scaling parameters: The wave-making mechanisms used in this experiments do not have quantifiable initial conditions (exept for the pressure pulse), which has to be estimated from images.

- **Domain size:** 0.5×0.5 m.

Ship1:

- **Ship length**(L)**:** 0.1 m (Roughly estimated from wave pattern)
- **Ship speed** (U)**:** 0.59 m/s (calculated from images $U = \Delta s/\Delta t$)
- **Froude number (Fr):** Fr$= U/\sqrt{gL} \approx 0.55$.

Ship2:

- **Ship length**(L)**:** 0.1 m (Roughly estimated from wave pattern).
- **Ship speed** (U)**:** 0.5 m/s (calculated from images $U = \Delta s/\Delta t$).
- **Froude number (Fr):** Fr$= U/\sqrt{gL} \approx 0.5$.

Droplet:

- **Droplet width**(d)**:** 0.01 m (estimated from initial perturbation).

Pressure pulse:

- **Pulse-width**(d)**:** 0.2 m (Calculated from pressure model $d = 0.23L$).

6.1.3 Results

Ring wave patterns: Figure 6.4 show the reconstructed surface height obtained from FS-SS for a single impulse response caused by a droplet impact. The physical dimensions (x, y) are scaled by the pulse width d and snapshots are compared with theoretical predictions calculated from section 2.6 with the estimated initial conditions.
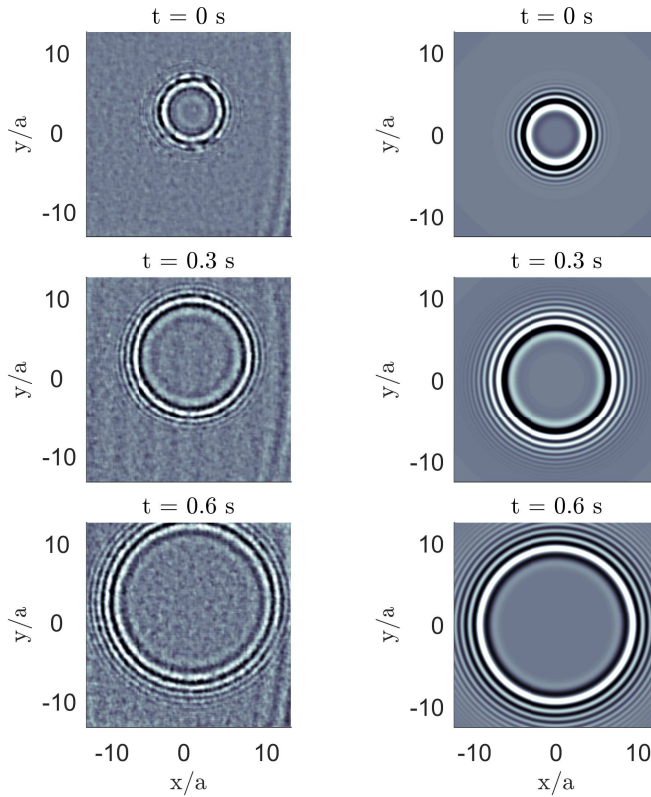

Figure 6.4: Snapshots of experimental (left) and numerical (right) ring wave patterns, where $h(x, y)$ is plotted in normalized coordinates $(x/a, y/a)$ as color, where a is the pulse width. The color map is scaled as a fraction of the max amplitude ($c = h_{\max}[-0.5, 0.5]$).

Pressure pulse: Figure 6.5 show the reconstructed surface height obtained from FS-SS for a single impulse response caused by a pressure pulse. The physical dimensions (x, y) are scaled by the pulse width d and snapshots are compared with theoretical predictions calculated from section 2.6 with the estimated initial conditions.
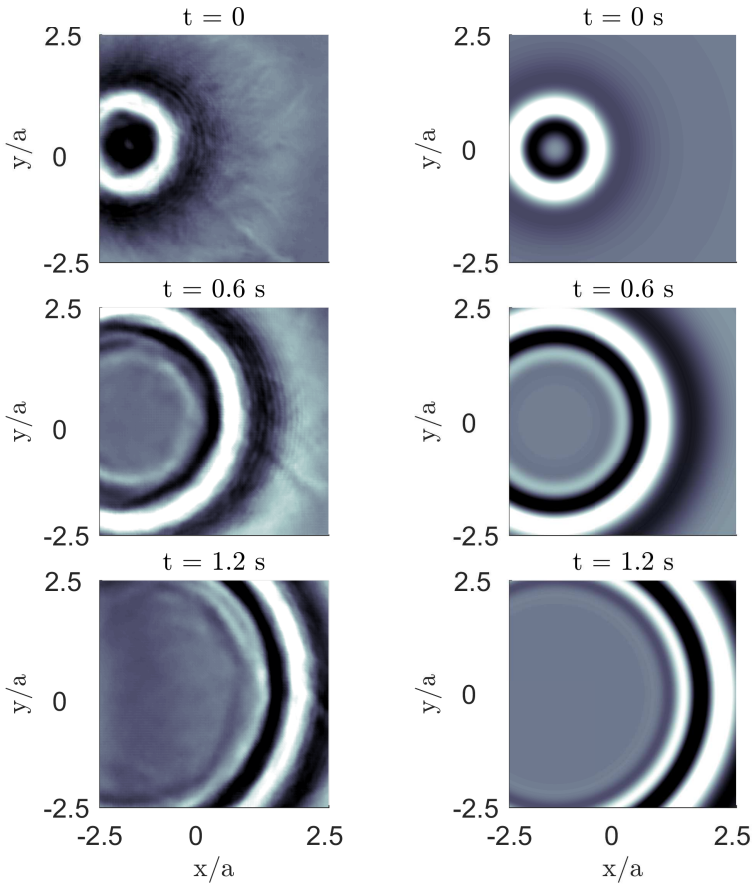

Figure 6.5: Snapshots of experimental (left) and numerical (right) ring wave patterns, where $h(x, y)$ is plotted in normalized coordinates $(x/a, y/a)$ as color, where a is the pulse width. The color map is scaled as a fraction of the max amplitude ($c = h_{\text{max}}[-0.5, 0.5]$).
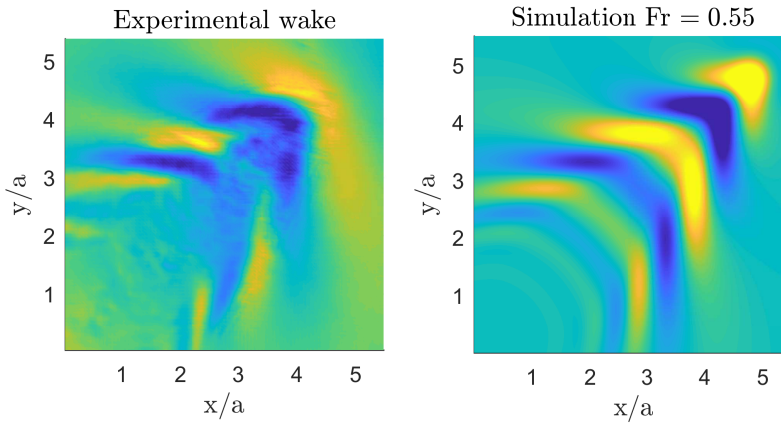
Ship wake:

Figure 6.6: Experimental (left) and numerical (right) shipwake, where $h(x, y)$ is plotted in normalized coordinates $(x/a, y/a)$ as color, where a is the scaling parameter for the ship. The color map is scaled as a fraction of the max amplitude ($c = h_{\max}[-0.5, 0.5]$).

Figure 6.7: Experimental (left) and numerical (right) shipwake, where $h(x, y)$ is plotted in normalized coordinates $(x/a, y/a)$ as color, where a is the scaling parameter for the ship. The color map is scaled as a fraction of the max amplitude ($c = h_{\max}[-0.5, 0.5]$).
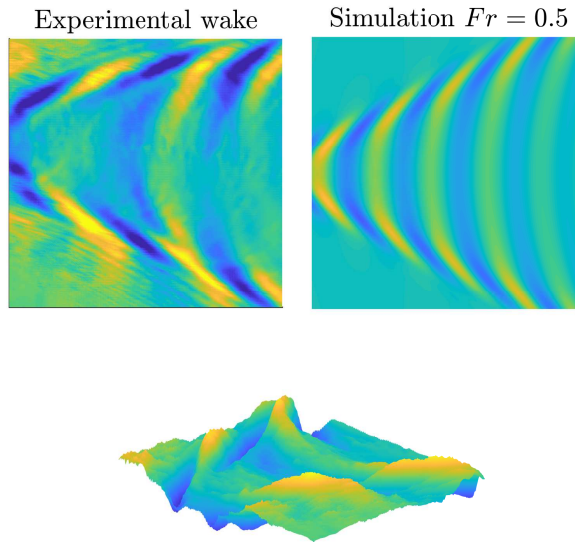
Spectral analysis: The spectral magnitude of the ring-waves generated by the pressure pulse is calculated and shown in Figure 6.8. One can clearly see that energy is centered on the linear dispersion line. For further analysis, discrete points are extracted by analyzing F finding the peak location for each ω.
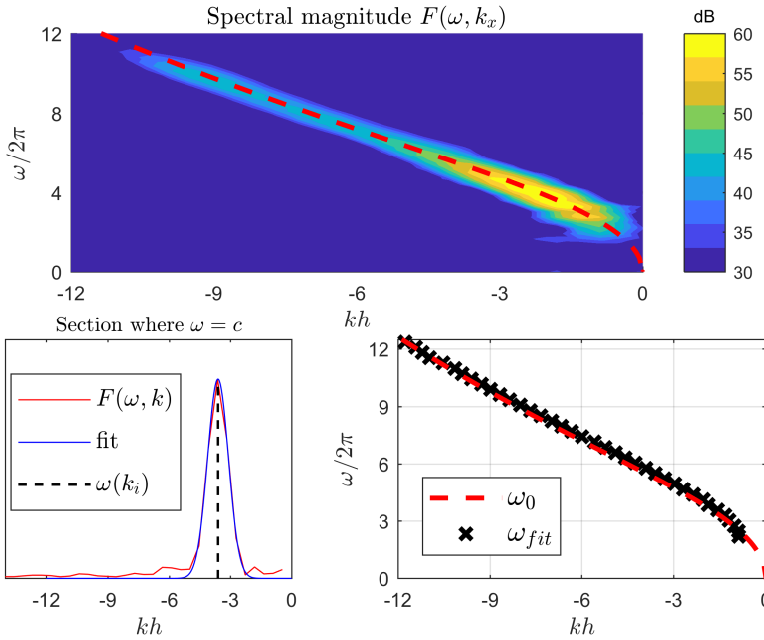

Figure 6.8: Dispersion data in quiescent waters. Sections from the spectral magnitude ($F(\omega, k)$), is fitted to a Gaussian to find the peak positions corresponding to the dispersion relation in discrete points.
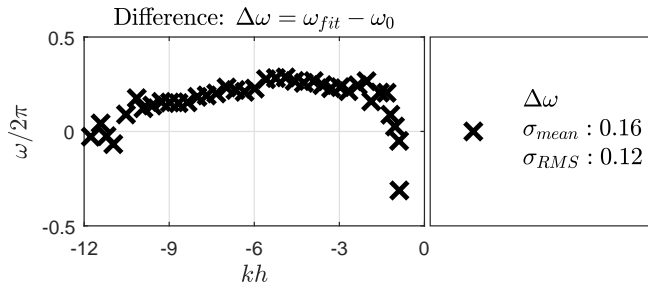

Figure 6.9: Difference between the linear dispersion relation and the discrete dispersion data obtained from experiments.

6.1.4 Discussion

Qualitative similarities: One can see from the different cases that by eye, theory seem to reconstruct the patterns. However, it is hard to find strong evidence to link the initial conditions in such a way hard comparisons are possible. Therefore it is much more quantitatively to analyze the dispersion data and compare it to the linear dispersion relation, which seems to agree quite well.

- **Droplet:** The experimental measurements of waves generated by the droplet is quantitatively comparison with the model of a pressure pulse. One can also note that the waves generated are a mixture of both capillary and gravitational waves, where the short wavelengths propagate faster than longer wavelengths, as predicted by theory.

- **Single pressure pulse:** Waves generated by a single pressure pulse seem to be in agreement with the model, where the data set seem to contain mostly gravitational waves, where longer wavelengths propagate faster than short ones also predicted by theory.

- **Ship wakes:** Both ship-wakes show similarity with the Froude scaled ship models, even though the estimate of the pulse width from experiments are rough. One should also note that the theoretical models require constant ship speed, which also was not well controlled in the experiments. However, the scaling laws seem to predict roughly the patterns and if one wants to perform ship resistance experiments no shear currents one need to improve boundary conditions (proper geometry), and a controlled ship speed.

- **Spectral analysis:** The analysis of the spectral magnitude reveals that the method is able to accurately predict wave dispersion in quiescent waters. The method of using Gaussian windows and fit spectral magnitude to a Gaussian model to obtain discrete dispersion data seem to give good agreement with the linear dispersion relation. However, there seems to be a small overprediction of ω, since the mean difference seems to lie above zero. This might be due to an error in the spatial calibration leading to a constant prediction error in the spectral domain.

6.2 Nonlinear waves

Objectives: To test limitations of FS-SS, nonlinear waves are generated and measured. In theory, FS-SS should struggle at large angles, which is apparent in nonlinear theory, where the nonlinearity is described through the average angle (steepness ka). Plane waves are generated by the pressure pulse resonating at 4Hz, which are measured by FS-SS and the waves are analyzed in both spatial and frequency domain and compared with Stokes theory (section 2.3).
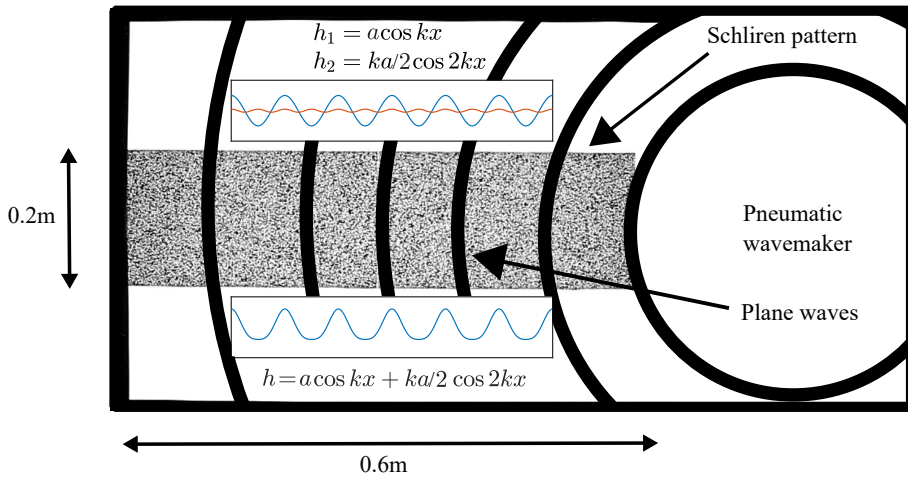

Figure 6.10: Setup for nonlinear wave experiment. Plane waves are generated by the pneumatic wavemaker at 4Hz, which is measured by FS-SS and compared to second-order theory.

Plane waves are measured using FS-SS and analyzed, both in spatial and frequency domain, where the steepness parameter (ka) is extracted. The spectral magnitude of $F(\omega, k_x)$ is calculated and compared to second order wave theory (stoke waves).

6.2.1 Procedure

Three methods to estimate the wave steepness (ka) are performed on data generated by the pneumatic wave-maker.

1. **Steepness calculation:**

   - ka from spectral analysis.

   - ka from gradient field (∇h).

   - ka from surface field (h).

2. **Dispersion relation:**

   - $F(\omega, k)$ is calculated and visualized in the (ω, k_x) plane, where the magnitude of F is compared to the first and second order dispersion lines ω_0.

Direct steepnes estimation: Stokes nonlinear theory (section 2.3) describes a second order wave, as Equation 6.1a, where the steepness parameter (ka) determines the relative magnitude of higher order terms compared to the first order harmonic (k). Amplitudes $(h_{\mathrm{amp}}, \nabla h_{\mathrm{amp}})$ are extracted from experimental measurements, which are used to solve roots of Equation 6.1a and Equation 6.1c expressed for steepness ka.
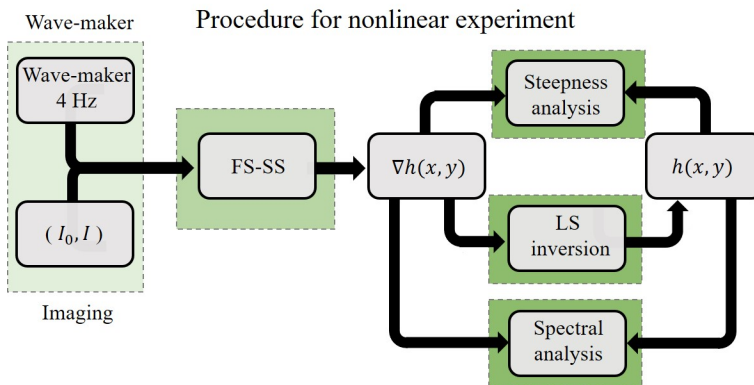

Figure 6.11: Procedure for nonlinear experiments. h and ∇h is obtained using FS-SS and steepness and spectral magnitude is estimated.

$$h = a(\cos{(kx + \omega t)} + (ka/2)\cos{2(kx + \omega t)}) \tag{6.1a}$$

$$ka = \frac{-1 + \sqrt{1 + 16h_{\mathrm{amp}}k}}{4} \qquad h_{\mathrm{amp}} = \sqrt{2}\mathrm{Var}[h] \tag{6.1b}$$

$$\nabla h_x = ka(\cos{(kx + \omega t)} + (ka)^2 \cos{2(kx + \omega t)}) \tag{6.1c}$$

$$ka = \frac{-1 + \sqrt{1 + \nabla h_{\mathrm{amp}}}}{2} \qquad \nabla h_{\mathrm{amp}} = \sqrt{2}\mathrm{Var}[\nabla h] \tag{6.1d}$$

Amplitudes ($h_{\mathrm{amp}}, \nabla h_{\mathrm{amp}}$) are estimated from the experimental data by multiplying the RMS by a factor $\sqrt{2}$.

Spectral steepness estimation: Steepness is also calculated by spectral analysis of h, and ∇h, where single frames are used to calculate $F(k_x)$, which is averaged over 200 frames. The magnitude of F should be peaked at k and $2k$, where the peak at $2k$ should be a factor $(ka, ka/2)$ of the peak at k.

Dispersion data: h and ∇h are transformed to frequency domain ($F(\omega, k_x, k_y)$), in window sizes of 2 seconds (100 samples), which are visualized in the (ω, k_x) plane and compared to linear and second order dispersion lines (ω_0).

6.2.2 Parameters

Optical parameters (summarized in Table 6.2) are obtained by measuring the lengths with a caliper, where the uncertainty could be in the order of 5%, resulting in a prediction error in the magnitude of the measured gradient field.

Parameter	symbol		Unit
Water depth	h	0.05	[m]
Air gap	h_a	0	[m]
Sampling rate	f_0	50	[1/s]
Number of samples	N	200	[-]

Table 6.2: Optical parameters for FS-SS.
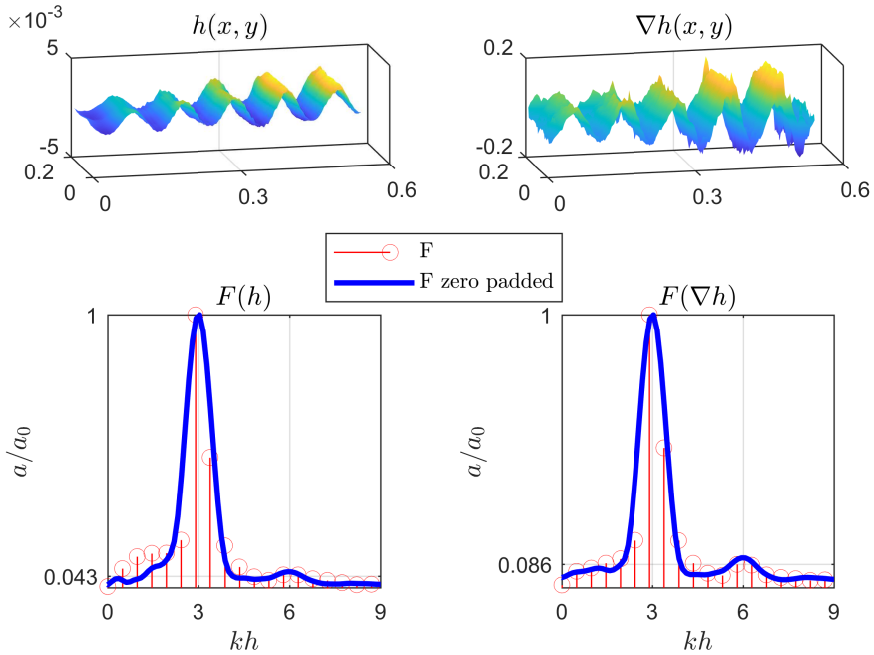
6.2.3 Results

Figure 6.12: Surface height scaled in meter (top left), gradient field scaled in meter and rad/meter (top right), and corresponding specters (bottom) normalized by depth h. F is calculated and averaged over 200 samples, where the peak is located at $kh \approx 3$, where $ka \approx 0.086$ for ∇h and $ka \approx 0.043$ for h. Spectral resolution is poor (red) due to short measurement domain, therefore zero padding and windowing (blue) is performed to obtain a smoother specter.
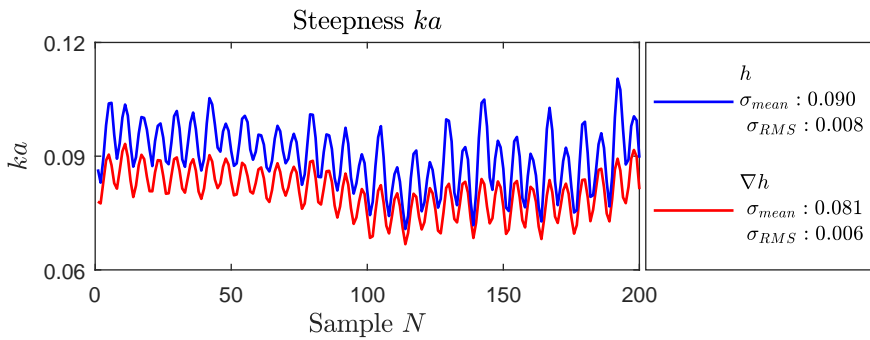

Figure 6.13: Steepness calculation in spatial domain, where both gradient field (red) and surface field (blue) is used to calculate the steepens parameter (ka).

steepness:

- From spectral analysis: $ka = 0.086$.

- From gradient field (∇h): $ka = 0.081 \pm 0.006$.

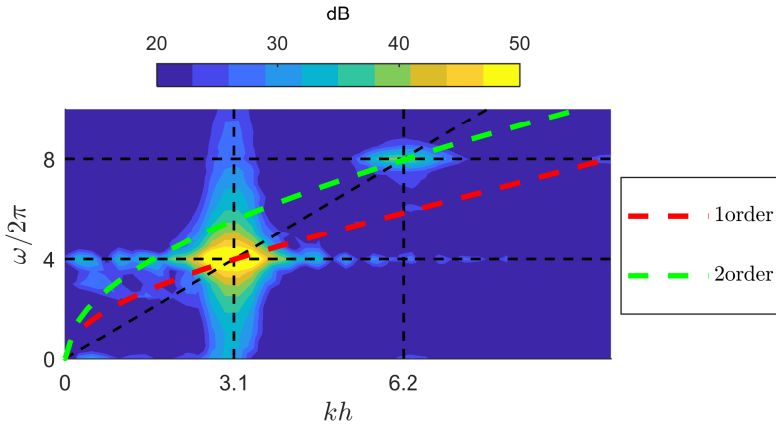- From surface field (h): $ka = 0.090 \pm 0.008$.

Figure 6.14: Spectral magnitude $F(\omega, k_x)$ (color) of ∇h, where analytic dispersion relation (lines) are added.
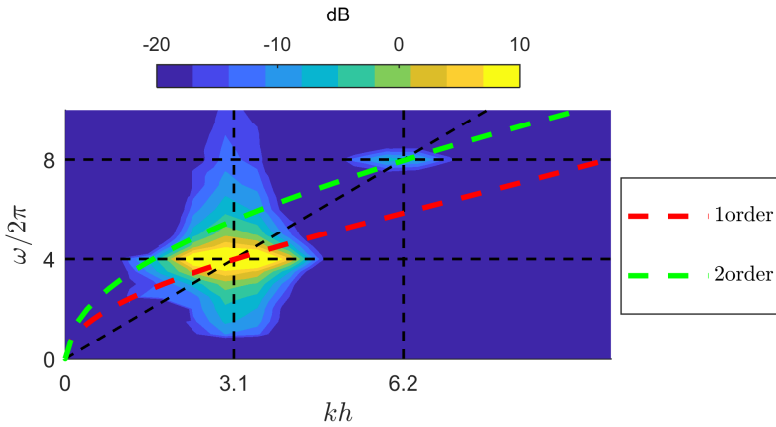

Figure 6.15: Spectral magnitude $F(\omega, k_x)$ (color) of h, where analytic dispersion relation (lines) are added.

Two Gaussian windows (2 seconds) are used to calculate $F(\omega, k_x)$ from both h and ∇h (Figure 6.14, Figure 6.15), which are visualized as color surfaces scaled in decibel. The first and second order dispersion lines (red, green) are added in addition to the average slope $(\Delta\omega/\Delta k)$ going through $\omega/2\pi = 4$Hz. The magnitude of F is peaked at $\omega/2\pi = 2$Hz where $kh = 3.1$, and at 8Hz where $kh = 6.2$, as predicted by 2nd order stokes theory.

6.2.4 Discussion

- **Steepness estimation:** The steepness calculated from the three different methods (spectral, h,∇h), are in agreement with each other, where the waves measured are non linear with a steepness factor of $ka = 0.86$. h seems to give higher prediction then ∇h, while the estimate from spectral analysis lies in between the two, where variation within each method, might be due to spectral leakage, finite domain measurements, and variating wave steepness over the samples. red gradient field ∇h.

- **Dispersion realtion:** Dispersion data $(F(\omega, k))$(Figure 6.14 , Figure 6.15) shows evidence of second order dispersion, where two distinct magnitude peaks are located at $(\omega = (4, 8)Hz, kh = (3.1, 6.2)$ as predicted by theory. However, one clearly see that spectral leakage occurs, especially at the first harmonic peak, smearing out the spectral magnitude, which might be the reason why it is hard to see two distinct peaks in Figure 6.12, where the peaks are not separated by ω.

- **Biased errors from cailbration:** All three methods are calculated from the same experimental data, and biased errors might have occurred due to errors in the optical calibration of the FS-SS setup. An overestimation of ∇h will lead to an overestimation of ka for all the methods used in this experiment.

- **Small angle approximation:** The reconstruction of the refracted pattern is dependent on a small angle approximation which is in direct violation with this experiment. The more non-linear the wave is, the more in violation is the measurement with the small angle approximation. However, DIC seem to handle the measured refraction pattern from these data, where the steepness is approximated to be around 0.1.

6.3 Current inversion from dispersion data and PIV measurements

Objectives: In this experiment, dispersion data obtained from FS-SS is used to calculate the velocity field $(U(z))$ which is compared to PIV measurements. Waves are strategically generated in 10 second ranging from 2-8Hz by both pneumatic and mechanical wavemakers. Two cases are considered, where different flow conditions $(U(z))$ are generated and measured.

1. **Case1:** Approximately linear shear.

2. **Case2:** Strong surface shear.

6.3.1 Procedure

Both mechanical and pneumatic wavemakers are used to generate a broad specter of waves, which is recorded, windowed, and fitted to obtain discrete points of $\omega(\mathbf{k})$. Further, the experimental dispersion data is used in an inversion algorithm calculating $U(z)$, which is also obtained by measuring several locations covering the schlieren pattern with PIV.
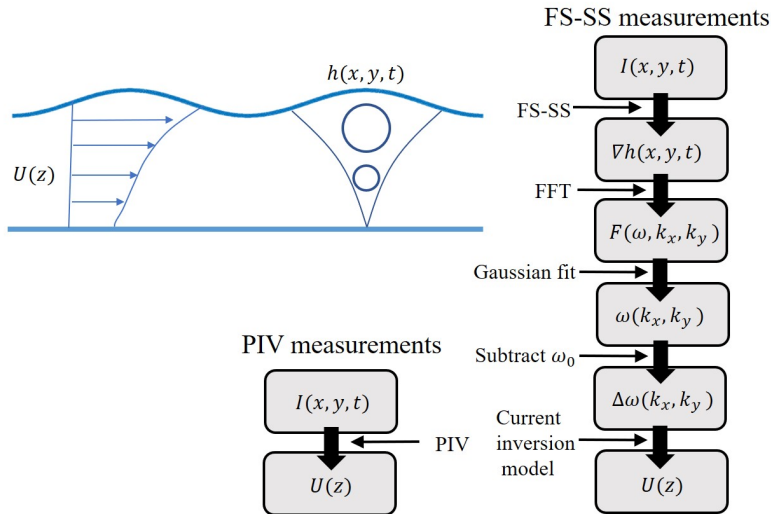

Figure 6.16: Flowchart for inversion experiments. The relationship between wave propagation $(\omega(\mathbf{k}), U(z))$ and flow velocity $(U(z))$ is used to measure the velocity profile from dispersion data obtained from FS-SS measurements, which is compared with PIV measurements.

Procedure:

- **Dispersion data:** Dispersion data is obtained by strategic measurements of wave-maker induced waves.

  1. **Data recording:** Waves are recorded in 10-second windows where the wave-makers changes frequency in 0.1 Hz steps.

  2. **Gradient reconstruction:** FS-SS is used to reconstruct $\nabla h(\mathbf{x}, t)$ and the spectral magnitude is calculated for each window $F(\mathbf{k}, \omega)$.

  3. **Discrete dispersion data:** A Gaussian fitting procedure is performed to obtain discrete points for the dispersion data $\omega(\mathbf{k})$.

  4. **Subtract linear dispersion shell:** The linear dispersion shell is subtracted to obtain $\Delta\omega = \omega - \omega_0$.

  5. **Inversion:** $U(z)$ is calculated using current inversion algorithm.

- **PIV measurements:** Velocity profiles are obtained by performing PIV measurements on different location covering the schlieren pattern.

  1. **Image pairs:** Image pairs are sampled by the PIV system in strategic positions covering the schlieren pattern.

  2. **Velocity calculations:** 2D velocity fields are calculated from image processing, which is averaged to obtain an estimate of the average velocity profile $U(z)$.

6.3.2   Parameters

		Symbol	**Value**	**Unit**
Case1	Depth	h_1	50	[mm]
	Air gap	h_a	0	[mm]
	Pumpcap		50	[%]
Case2	Depth	h_2	35	[mm]
	Air gap	h_a	20	[mm]
	Pumpcap		25	[%]

Table 6.3: Depth and pump capacity for the two cases.

FS-SS: Waves generated by wavemakers are measured where windows of data are analyzed to obtain spectral information ($\omega(\mathbf{k})$).

Case1: Approximately linear sheared profile.

- Wavemaker: Pneumatic.

- Frequency range: [2-6] Hz.

- Number of windows: $41 \rightarrow \omega(k)$ 41 samples.

- Window size: 10 sec $\rightarrow \Delta\omega = 0.1$ Hz.

- Window type: Gaussian.

Case2: Strong surface shear

- Wavemaker: Mechanical and pneumatic.

- Frequency range: [1-4] and [4-8] Hz.

- Number of windows: $(37 + 41) \rightarrow \omega(k) = 76$ samples.

- Window size: 10 sec $\rightarrow \Delta\omega = 0.1$ Hz.

- Window type: Gaussian.

PIV: PIV measurements were carried out at equally distributed locations covering the schliren pattern (Figure 6.17).

Case1: Approximately linear sheared profile.

1. Number of positions: 9 positions.

2. Interrogation window size: Changes but roughly 100x50 pixels $\rightarrow U(y)$ 15-20 samples.

3. Number of samples/correlation function: 200 image pairs.

Case2: Strong surface shear

1. Number of positions: 4 positions.

2. Interrogation window size: Changes but roughly 100x50 pixels $\rightarrow U(y)$ 15-20 samples.

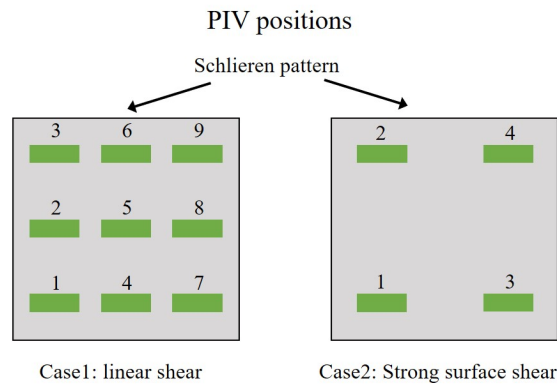3. Number of samples/correlation function: 200 image pairs.

PIV positions

Figure 6.17 show positions measured by PIV relative to the schlieren pattern for both cases. Case1 (linear shear) seemed to be both stationary and steady. Therefore, a reduction to 4 measurement positions were chosen for the second case.

6.3.3 Results

Case1: Approximately linear profile

PIV measurements: PIV measurements are carried out at different positions (1-9), which are shown in Figure 6.18. Streamlines ($\psi = C$) are computed from (u, w) and plotted as contour lines where color determines magnitude of ψ. The velocities are averaged and plotted in Figure 6.19 (blue crosses), where the red line is the total averaged velocity profile $U(z)$, which will be used to compare to the inversion.
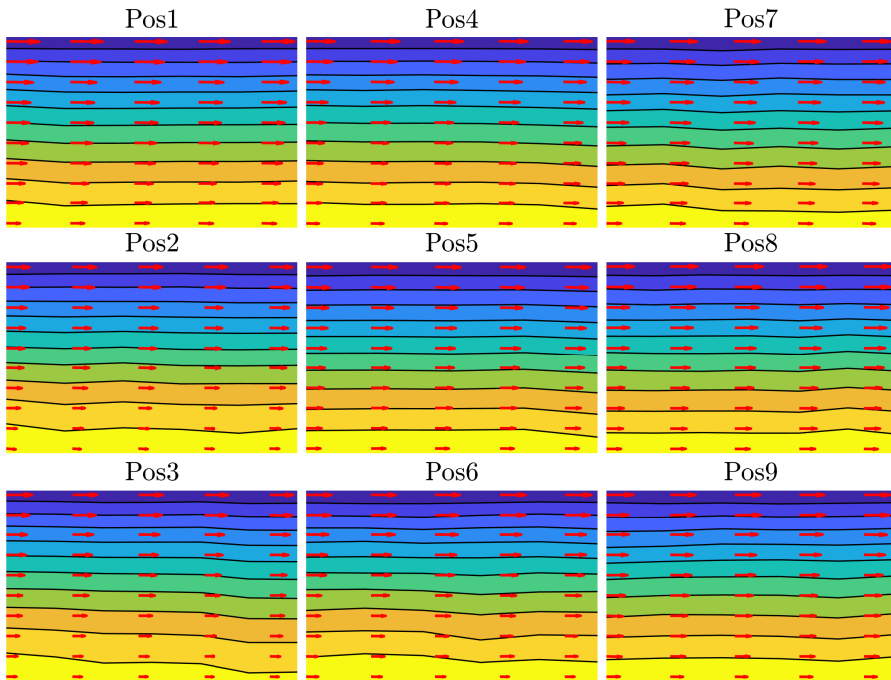

Figure 6.18: Streamlines ($\psi = \int u \, dz$) and velocity vectors (u, w) shown in all nine positions from PIV measurements. The average profiles from each position are further used to estimate the velocity profile $U(z)$.
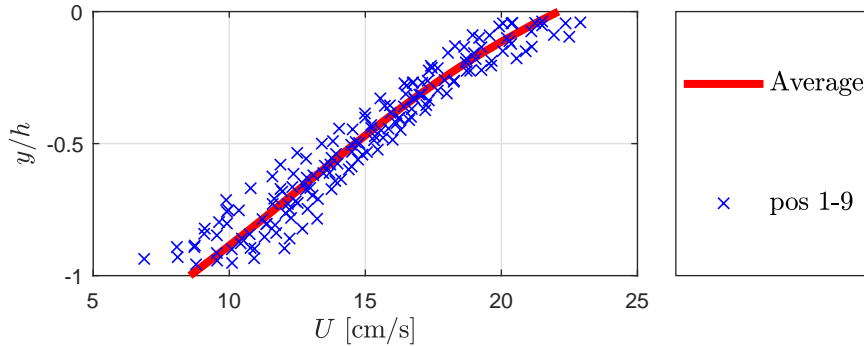
Figure 6.19: Average velocity profile, where the downstream averaged PIV measurements from pos 1-9 are used to obtain $U(y)$ (red line).

Dispersion measurements:

Spectrogram: The pneumatic wave-maker was programmed to pulse at a range of frequencies for 10 second windows with a step of $\Delta f = 0.1$Hz, corresponding to the frequency resolution. Figure 6.20 show a spectrogram of the measured frequencies $(\omega/2\pi)$ of the surface gradient (∇h), which corresponds to the pneumatic pulse frequency. ω is extracted from the spectral magnitude F, where discrete points are plotted together with the linear dispersion line (red line), where upstream propagating waves have a positive shift, while downstream propagating waves have a negative shift.
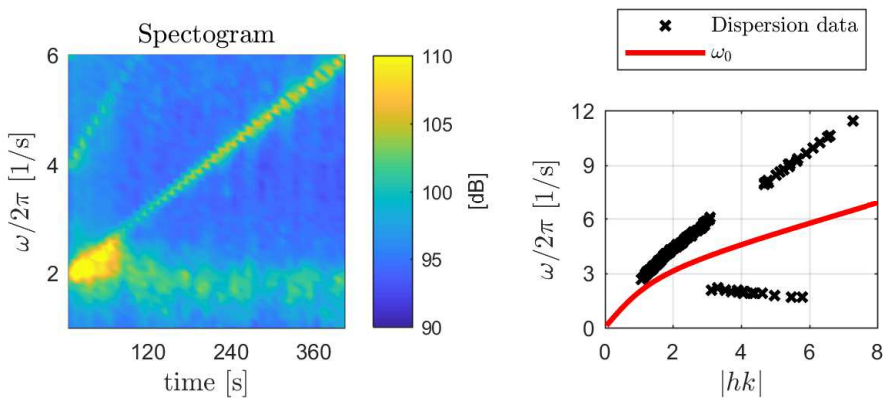

Figure 6.20: Spectrogram (left) where the spectrum $(F(\omega))$ is shown for each window (10 seconds). Dispersion data fitted to obtain discrete points for $\omega(k)$ (right), where both upstream and downstream waves are plotted with positive wave-numbers.

Current inversion: Dispersion data is used in the inversion algorithm described in section 2.5. Figure 6.21 shows the velocity profile from PIV measurements and inversion at different curvature constraints, where the residual error is plotted at the top.Figure 6.22 shows the chosen solution where the reduction in residual seem to stagnate along with the discrete dispersion data together with lines obtained from the resulting profiles both from PIV and the final inversion.
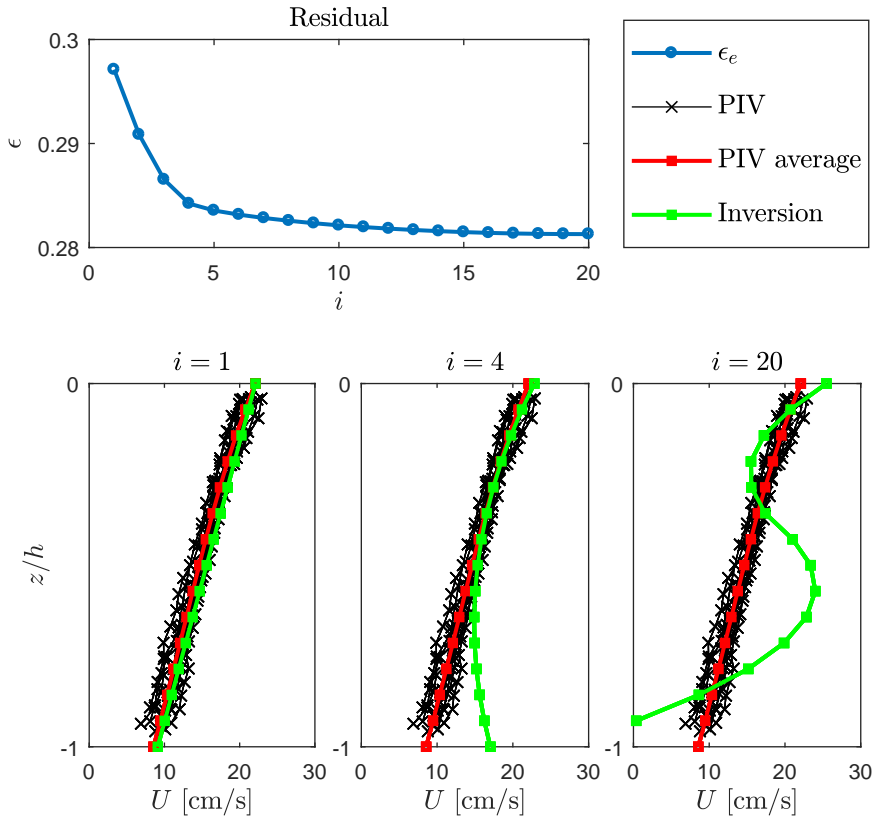

Figure 6.21: Residual (top) where i relates to reduced constraint on the curvature (d^2U/dz^2), and velocity reconstructions (bottom) for different constraints (green lines), where PIV (crosses) measurements are carried out at nine positions covering the domain of interest represented by the mean profile (red line).
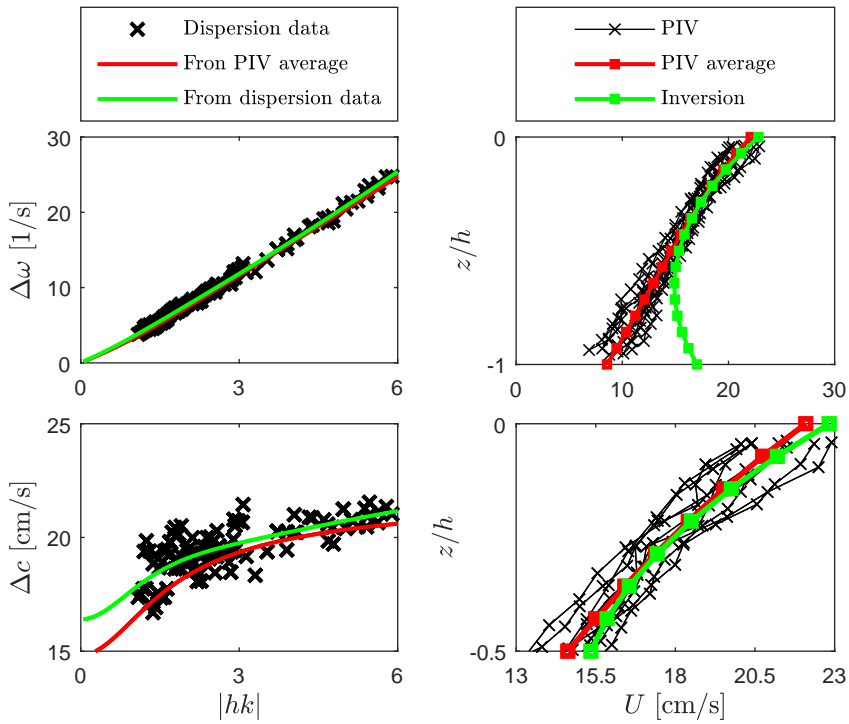
Figure 6.22: Dispersion data (left) where both experimental data (crosses) and $c_1/\Delta\omega$ from PIV and inversion (red/green lines) are shown. Velocity data (right) are shown both for PIV measurements (position 1-9) as black crosses, where the red line denotes the average, and the velocity profile obtained from the inversion (green line).

The dispersion data (left in Figure 6.21) is used in the inversion algorithm resulting in an optimal solution for $U(y)$, with constrains on the curvature(d^2U/dz^2), where both experimental data (black crosses) and models (red/green curved) are shown in Figure 6.21.

Case2: Strong surface shear

PIV measurements:

Pos1 Pos4

Pos2 Pos3

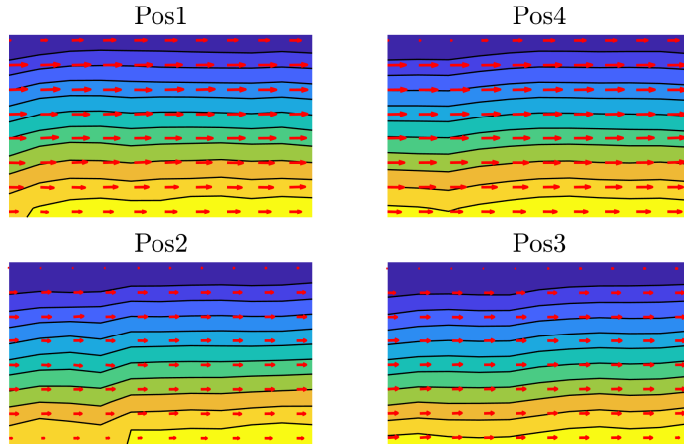**Figure 6.23:** Streamlines ($\psi = \int u dz$) and velocity vectors (u, w) shown in all nine positions from PIV measurements. The average profiles from each position are further used to estimate the velocity profile $U(z)$.

Streamlines and average profile: PIV measurements are carried out at different positions (1-4), which shown in Figure 6.23. Streamlines ($\psi = C$) are computed from (u, w) and plotted as contour lines where color determines magnitude of ψ. The velocities are averaged and plotted in Figure 6.19 (blue crosses), where the red line is the total averaged velocity profile $U(z)$, which will be used to compare to the inversion.
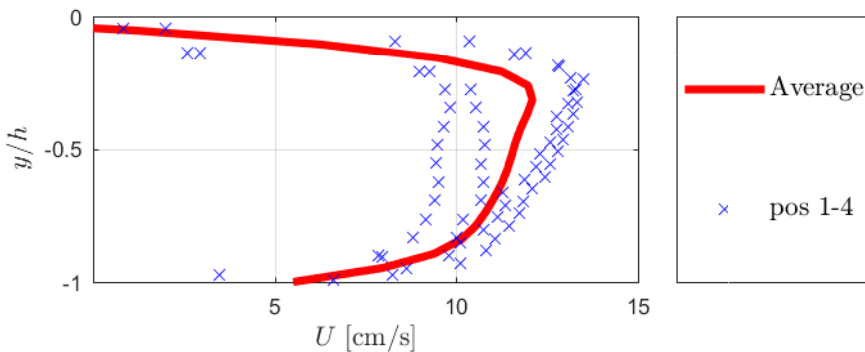
Figure 6.24: Average velocity profile, where PIV measurements from pos 1-4 are used to obtain $U(z)$ (red line). There seems to be a span wise variation between (1,2) and (3,4) in the velocity profiles. However, the downstream variation (1,4) and (2,3) seems to be developed.

Dispersion measurements:
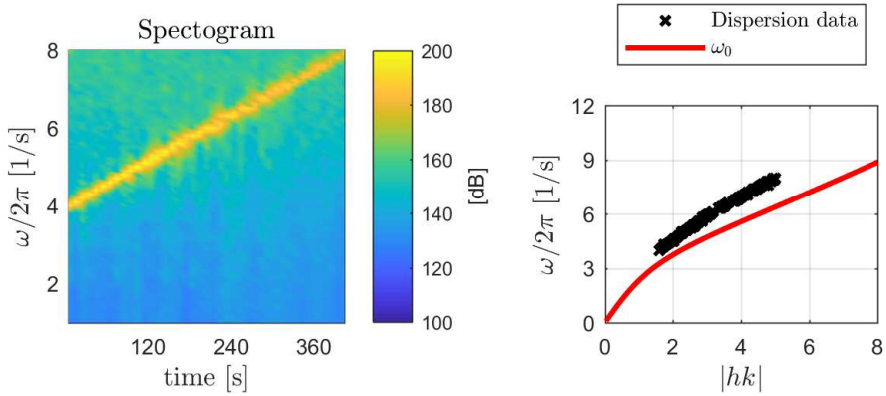
Figure 6.25: Spectogram (left) generated by pneumatic wavemaker, where the spectrum $(F(\omega))$ is shown for each window (10 seconds). Dispersion data fitted to obtain discrete points for $\omega(k)$ (right).
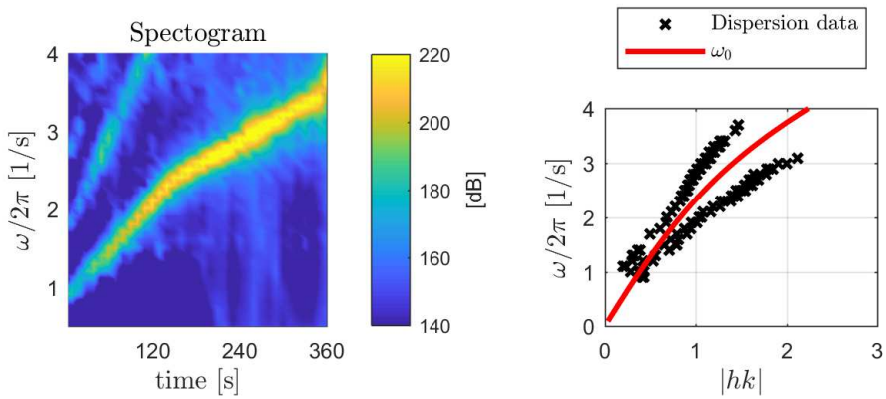
Figure 6.26: Spectogram (left) generated by mechanical wavemaker, where the spectrum $(F(\omega))$ is shown for each window (10 seconds). Dispersion data fitted to obtain discrete points for $\omega(k)$ (right)

Spectograms and dispersion data: For the second case (strongly sheared current), both pneumatic and mechanical wavemakers were used to generate dispersion data, where Figure 6.25 and Figure 6.26 show spectograms of waves generated as a function of time. The dispersion data (black crosses) are extracted by finding peak positions from $F(\mathbf{k}, \omega)$, which are combined for both cases giving a broader specter (Figure 6.27). Both upstream and downstream propagating waves are plotted for positive wave-numbers.
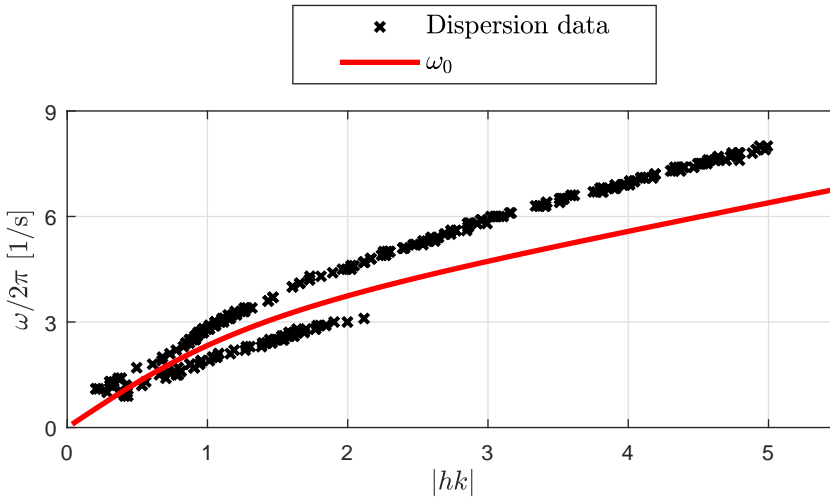
Figure 6.27: Dispersion data (crosses), where both data from both mechanical and pneumatic wave-makers are added and linear dispersion (red line).

Current inversion: Dispersion data is used in the inversion algorithm described in section 2.5. Figure 6.28 shows the velocity profile from PIV measurements and inversion at different curvature constraints, where the residual error is plotted at the top.Figure 6.29 shows the chosen solution where the reduction in residual seem to stagnate along with the discrete dispersion data together with lines obtained from the resulting profiles both from PIV and the final inversion.
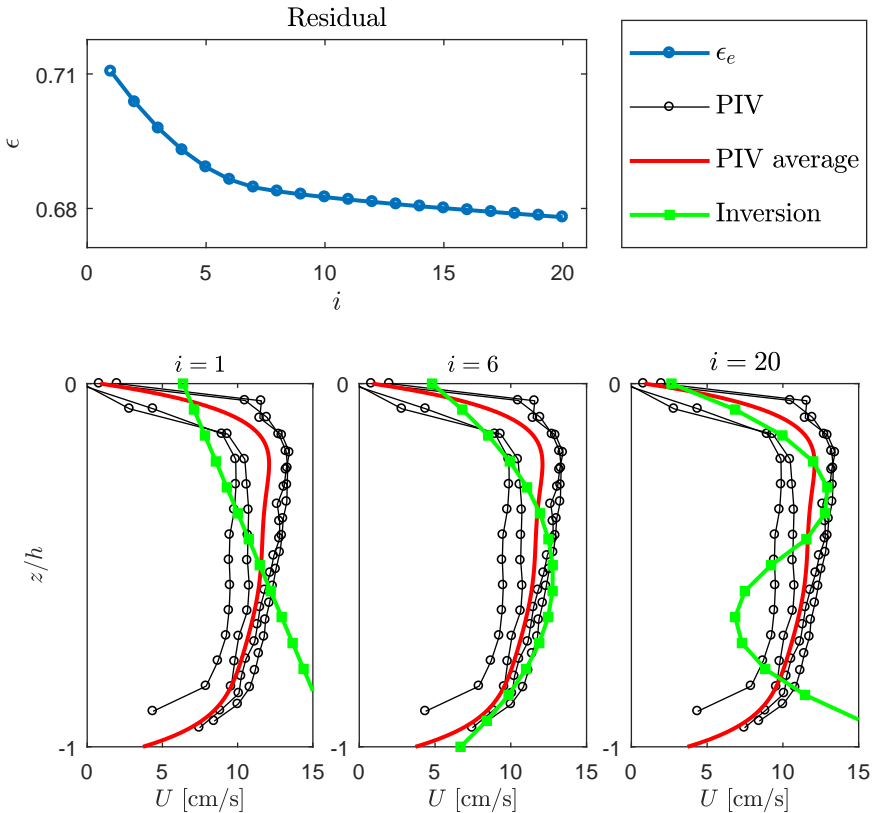
Figure 6.28: Residual (top) where i relates to reduced constraint on the curvature (d^2U/dz^2), and velocity reconstructions (bottom) for different constraints (green lines), where PIV (crosses) measurements are carried out at nine positions covering the domain of interest represented by the mean profile (red line).
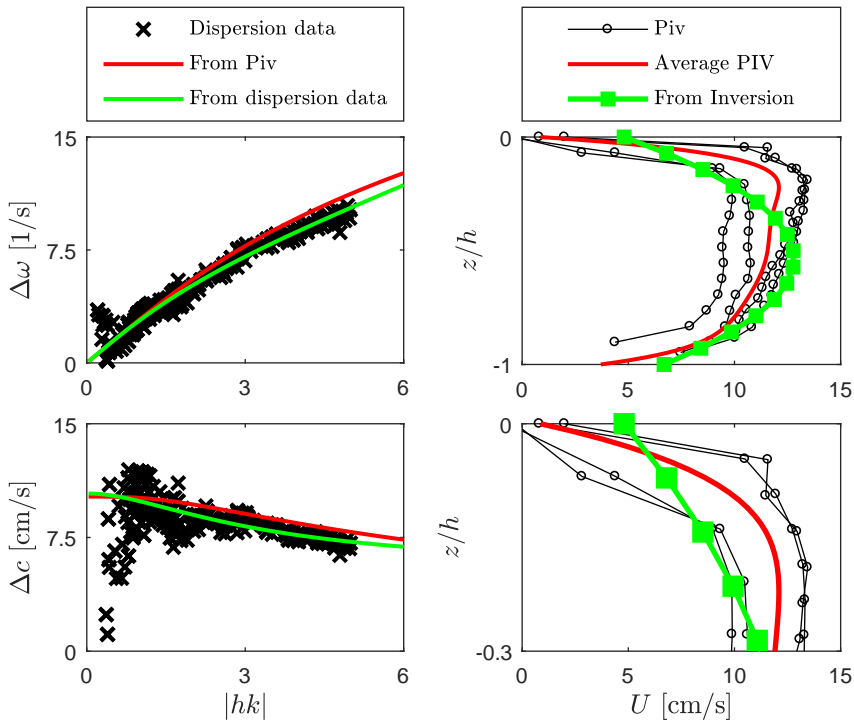
Figure 6.29: Dispersion data (left) where both experimental data (crosses) and $c_1/\Delta\omega$ from PIV and inversion (red/green lines) are shown. Velocity data (right) are shown both for PIV measurements (position 1-4) as black crosses, where the red line denotes the average, and the velocity profile obtained from the inversion (green line).

6.3.4 Discussion

Average measurements by PIV: PIV measurements are performed by averaging correlation functions over several image pairs, thus the measurements are averaged in time. However, both downstream and in-plane differences between locations seem to be small, and the corresponding space averaged profile is a good representation of the flow field.

- **Case1:** 9 positions are averaged where all profiles show similar shape and magnitude.

- **Case2:** In the case of strong surface shear only 4 positions were measured. The downstream variation of velocities are small, however, there seems to be an in-plane variation, which is resulting in a larger uncertainty of the overall profile compared to the linearly shared case.

Dispersion measurements by FS-SS: The dispersion data obtained from analyzing windows of schlieren data is hard to relate to sources of uncertainty. However, the analysis in quiescent waters showed that the precision was quite good, and there was a small constant deviation, probably caused by calibration errors or spectral leakage.

- **Case1 Linear profile:** The data was taken before the construction of the mechanical wave-maker, hence a smaller broadband of frequencies (3-6 Hz). were generated. However, the spectrograms show that the generated waves correspond well to the measured dispersion data.

- **Case2 Strong surface shear:** Both the mechanical and pneumatic wave-makers were used to generate dispersion data, hence a broader broadband of frequencies (1-8 Hz) was generated. However, the spectrograms show that the generated waves correspond well to the measured dispersion data.

Inversions: The inversion algorithm is highly dependent on the curvature constraint, which restricts the shape of the profile.

- **Linearly shared current:** For a linearly shear current, a though constraint seem to reproduce the profile quite good. However, a linear profile is not a good test case, since over constraining gives a good representation even though the experimental data contains a lot of noise.

- **Strong surface shear:** The second case of strong surface shear better demonstrates the consequence of imposing a too tough constrain on curvature, where the surface shear is underpredicted. To accurately capture the strong curvature close to the free surface, one also notes that huge deviations from the PIV measurements occur close to the bottom.

Depth dependent accuracy: The dispersion data obtained from analyzing waves are most sensitive close to the surface, hence accuracy decreases exponentially with depth for the reconstructed current profile. This effect can be seen by looking at kh which determines how deep the wave penetrates, hence how much information the dispersion data reveals on the current.

Chapter 7

Conclusion and suggestions for further work

Objetives: In this thesis experimental methods to measure shear-dependent wave dispersion are implemented and used to study waves propagating on vertically sheared currents. To achieve such measurements the following systems will be put in place, implemented, and tested.

1. Measure surface topology both in space and time.

2. Generate waves which can be controlled in space and time.

3. Measure velocities present in the flow.

4. Generate steady and uniform shear flow conditions.

This, together with implementing and using accompanying data analysis techniques, are the objectives of the thesis.

Surface topology: Two optical methods for reconstructing the liquid surface topology are implemented, tested and used in case study experiments, where wave phenomenon has been measured and compared to theory.

- **Fourier Transform Profilometry (FTP):** FTP is shown to be an accurate method for measuring how a free liquid surface deforms in space and time. However, there are many parameters that have to be understood and tuned depending on the setup, to obtain good images. This study has through case studies investigated the importance of these parameters, where FTP depends on geometrical relations relating a deformed optical fringe pattern to the reconstruction of the surface topology. A method to calibrate the optical parameters is designed and shown to be an efficient and accurate method, where a calibrated shape is reconstructed and compared to caliper measurements. Using FTP on a liquid surface depends on diffuse reflection, hence color pigment has to be added to the water, where titanium

dioxide is chosen as the pigment. Contrast levels, signal noise ratios (SNR), and effect on wave damping properties are measured in a case study, where higher pigment concentrations result in better SNR giving improved FTP images. The study also showed increased damping with pigments. However, the damping experiment was performed with different boundary conditions for each concentration level, hence decoupling the two variables is not possible from these data sets. Dispersion of linear surface waves is measured and compared to linear wave theory, which shows good correlation between measured values and theoretical predictions.

- **Free Surface Synthetic Schlieren (FS-SS):** FS-SS is also shown to be an accurate method to reconstruct surface topology. However, this method measures the surface gradient, hence the topology has to be reconstructed by a least square inversion technique implemented. However, the dispersion experiments do not require the surface topology since the dispersion of waves can be related directly to the specter of the gradient components, hence the gradient inversion is not necessary to measure dispersion data used in the current inversion technique. FS-SS relates diffraction of a dot pattern to the surface gradient and unlike FTP is compatible with Particle Image Velocimetry (PIV), which also requires a transparent fluid, hence topology and velocity can be measured simultaneously. The accuracy of the FS-SS measurements are measured through dispersion measurements performed on linear waves in quiescent waters, where the known linear dispersion relation is compared to measured values. The full surface topology reconstruction is also demonstrated in a study where ring and ship wave patterns in quiescent waters are measured and compared to theoretical predictions, which quantitatively show good agreement.

Wave-makers: To generate waves, two wave-maker mechanisms are implemented where spectrograms calculated from dispersion analysis shows agreement between generated waves and calculated wave spectrum from the measured surface topology. Wave-makers are used to generate waves used in experiments where dispersion data are used to calculate flow velocities and linear and nonlinear waves are studied and compared to theoretical predictions from wave theory.

- **Pneumatic wave-maker:** A pneumatic wave-maker is implemented where a nozzle/valve/regulator system is used to generate controlled pulses (puffs) of air flow perturbing the free surface. The stagnation point pressure is explicitly described through a pressure model developed by combining classical fluid flow solutions, which is confirmed experimentally by pitot tube measurements of the jet. The pneumatic wave-maker is used to generate linear and non-linear ring waves, which are measured using FS-SS, and compared to theory showing agreement.

- **Mechanical wave-maker:** A mechanical wave-maker is implemented where a crankshaft mechanism powered by a DC-motor is driving a displacement wave-maker generating waves at the same rate as the rotation of the mechanism. The system is used to generate dispersion data where spectrograms obtained from spectral analysis confirms the relation between wave-maker motion and generated waves.

Velocity measurements by Particle Image Velocimetry (PIV): To measure the velocity field an LED powered PIV system is designed and implemented where image pairs of tracer particles are used to calculate the average flow velocities. A capacitor circuit dumping high current pulses through an LED synchronized with a double exposure CCD camera is installed. Light collimation is achieved by a combination of directing light from the LED through optical fibers and a cylindrical lens converging to a thin light sheet with high intensity. The resulting measurements reproduce correlation averaged velocity fields at low signal noise ratios (SNR).

Shear flow generation: A centrifugal pump is circulating water between two tanks flowing over a flat transparent plate, where both PIV and FS-SS are used to measure surface topology and velocities.

- **Curved mesh/honeycombs:** A combination of a curved mesh and straight honeycombs are implemented to generate a depth varying velocity profile, which is approximately linear. PIV is used to measure the 2D flow velocity downstream of the honeycombs both with and without a mesh where the shear-generating mechanism is confirmed.

- **Wall effect:** By running the pump at low capacity it turned out a stagnation phenomenon caused a section of strong surface shear upstream from the wall in the downstream basin. The velocities were measured using PIV, which confirmed that the profile was approximately uniform in space and time, and current inversion experiments were performed on this velocity profile giving similar velocity profile.

Inversion technique for current profile reconstruction: FS-SS, Wave-makers, and PIV are combined in a case study where space and time-averaged velocity profiles are measured both using PIV and shear affected dispersion data in an inversion algorithm, where the integral relation between wave-number dependent Doppler shifts and flow velocities are inverted to calculate the vertical structure of the current. Both methods show measurements in agreements with each other where the results from the inversion are strongly dependent on a curvature constraint and the broadness of the measured wave spectra.

- **Linear shear current:** The inversion method is in agreement with the PIV measurements of the velocity profile. However, the results show that imposing a strong constraint on curvature on a profile without curvature, results in a good reconstruction even though the dispersion data is noisy, hence does not give valuable information on the sensitivity of the method.

- **Strong surface shear:** The inversion of the strongly sheared profile also is in agreement with the PIV measurements. However, one clearly sees the weakness of the method due to noise on the dispersion data, where the inverted profile is heavily dependent on the curvature constraint. By roughly having the actual profile, one can determine a curvature constraint, giving a good representation. However, in field measurements, this will not be the case and further work on determining good ways of constraining the inversion from the experimental data is needed.

Suggestions for further work: The work performed in this thesis lays the foundation for further current-wave interaction experiments, where topics such as wave turbulence, wind-induced waves, and shear affected ship resistance are among topics which can be performed using the same measurement systems. Improving the existing methods getting a better understanding of sources of error, accuracy and systematic routines are also necessary. Further analysis of the inversion problems described in section 2.5 where better theoretical understanding can give better ways of constraining the inversion, which can be tested on data obtained from experiments.

- **More measurements:** More measurements on different current profiles which are more uniform spanwise and in time can give a better understanding of what causes the different sources of uncertainty. By understanding sources of uncertainty one might design systems to avoid or compensate for errors leading to better data.

- **Improve methods for current generation:** Better ways of generating flow conditions, which are uniform spanwise and in time could reduce uncertainty in experimental data caused by varying flow conditions, decoupling a source of error.

- **Compare to field measurements:** To further investigate the practical use of the current inversion technique it would be interesting to obtain dispersion data from field measurements, which can be compared to experimental analysis. One could either obtain existing data or invest in an X-band radar system to perform in-house measurements.

Other topics: The main focus in this thesis has been to measure the dispersion of waves, which can be related to depth varying Doppler shifts. The experimental techniques implemented can also be used for other wave topics listed below.

- **Wind induced waves:** Most waves are generated by momentum transfer from the wind velocity in the atmosphere. The transfer processes on the interface between gasses and liquids are not well understood and is a potential field of study where the experimental methods could contribute in an experimental setup.

- **Ship resistance/wake patterns:** The shear induced effect on ship resistance has not been experimentally verified, hence a natural continuation of the work performed in this thesis would be to measure forces and wake patterns on objects moving relative to vertically sheared currents. Force measurements could be achieved by adding a strain gauge to a translating rod system driven by a pneumatic cylinder and surface patterns can be measured by either FTP or FS-SS.

- **Nonlinear waves:** The shear induced effects on nonlinear waves are also a topic in which there are not much understanding, hence experimental studies complimented with extended theoretical analysis of nonlinear waves propagating on sheared currents could be a way to progress with the methods implemented in this thesis.

Bibliography

[1] J. Campana, E. J. Terrill, and T. D. Paolo, "A new inversion method to obtain upper-ocean current-depth profiles using x-band observations of deep-water waves," *Journal of atmospheric and oceanic technology*, vol. 34, pp. 957–970, 2017.

[2] B. Lund, H. Graber, H. Tamura, C. O. Collins, and S. M. Varlamov, "A new technique for the retrieval of near-surface vertical current shear from marine x-band radar images," *Journal of Geophysical Research*, vol. 32, pp. 1928–1944, 2015.

[3] D. H. Peregrine, "Interaction of water waves and currents," *Advances in Applied Mechanics*, vol. 16, pp. 9–117, 1976.

[4] R. A. Skop, "Approximate dispersion relation for wave-current interactions," *Journal of waterway, Coastal and Ocean engineering*, vol. 113, pp. 187–195, 1987.

[5] J. T. Kirby and T. M. Chen, "Surface waves on vertically sheared flows: Approximate dispersion relations," *Journal of Geophysical Research*, vol. 94, pp. 1013–1027, 1989.

[6] R. H. Stewart and J. W. Joy, "Hf radio measurements of surface currents," *Deep Sea Research*, vol. 21, pp. 1039–1049, 1974.

[7] S. Å. Ellingsen and Y. Lie, "Approximate dispersion relations for waves on arbitrary shear flows," *Journal of Geophysical Research*, 2017.

[8] B. K. Smeltzer and S. Å. Ellingsen, "Surface waves on currents with arbitrary vertical shear," *Physics of Fluids*, vol. 29, 2017.

[9] S. Å. Ellingsen, "Initial surface disturbance on a shear current: The cauchy-poisson problem with a twist," *Physics of Fluids*, vol. 26, 2014.

[10] S. Å. Ellingsen, "Ship waves in the presence of uniform vorticity," *Journal of Fluid Mechanics*, vol. 742, 2014.

[11] M. Takeda and K. Mutoh, "Fourier transform profilometry for the automatic measurement of 3-d object shapes," *Applied Optics*, vol. 22, pp. 3977–3982, 1983.

[12] M. Chekroun, A. Maurel, V. P. G. Lagubeau, P. Cobelli, and P. P. A. Przadka, "Space-time resolved experiments for water waves," *Acta Physica Polonica*, vol. 120, pp. 143–148, 2011.

[13] A. Maurel, P. Cobelli, V. Pagneux, and P. Petitjeans, "Experimental and theoretical inspection of the phase-to-height relation in fourier transform profilometry," *Applied Optics*, vol. 48, pp. 380–392, 2009.

[14] P. Cobelli, A. Maurel, V. Pagneux, and P. Petitjeans, "Global measurement of water waves by fourier transform prolometry," *Exp Fluids*, vol. 46, pp. 1037–1047, 2009.

[15] A. Przadka, B. Cabane, and P. P. V. Pagneux, A. Maurel, "Fourier transform profilometry for water waves: how to achieve clean water attenuation with diffusive reflection at the water surface," *Exp Fluids*, vol. 52, p. 519–527, 2012.

[16] W. Dunn and S. Tavoularis, "The use of curved screens for generating uniform shear at low reynolds numbers," *Exp Fluids*, vol. 42, pp. 281–290, 2006.

[17] H. G. C. Woo and J. E. Cerak, "The production of constant shear-flow," *Journal of Fluid Mechanics*, vol. 234, pp. 279–296, 1991.

[18] I. P. Castro, "Some problems concerning the production of a linear shear flow using curved wire-gauze screens," *Journal of Fluid Mechanics*, vol. 76, pp. 689–709, 1976.

[19] P. R. Owen and H. K. Zieknkiewicz, "The production of uniform shear flow in a wind tunnel," *Journal of Fluid Mechanics*, vol. 2, pp. 521–531, 1957.

[20] C. Willert, B. Stasicki, J. Klinner, and S. Moessner, "Pulsed operation of high-power light emitting diodes for imaging flow velocimetry," *Measurement Science and Technology*, vol. 21, no. 7, 2010.

[21] M. Raffel, C. E. Willert, S. T. Wereley, and J. Kompenhans, *Particle Image Velocimetry- A practical guide 2nd edn.* springer, 2007.

[22] U. Shavit, R. J. Lowe, and J. V. Steinbuck, "Intensity capping: a simple method to improve cross-correlation piv results," *Exp Fluids*, vol. 42, pp. 225–40, 2006.

[23] F. Moisy, M. Rabaud, and K. Salsac, "A synthetic method for the measurement of the topography of a liquid interface," *Exp Fluids*, vol. 46, pp. 1021–1036, 2009.

[24] W. Thompson, *Mathemathical and Physical Papers.* Cambridge University Press, 1910.

[25] H. Lamb, *Hydrodynamics.* Cambridge University Press, 1932.

[26] L. D. Landau and E. M. Lifshitz, *Fluid Mechanics.* New York: Pergamon, 1987.

[27] S. Chandrasekhar, *Hydrodynamic and Hydromagnetic Stability.* Oxford University Press, 1961.

[28] R. G. Dean and R. A. Dalrymple, *Dalrymple-Water wave mechanics for engineers and scientists.* World Scientific, 1991.

[29] P. G. de Gennes, F. B. Wyart, and D. Quéré, *Capillarity and Wetting Phenomena—Drops, Bubbles, Pearls, Waves.* Springer, 2002.

[30] Y. Li, B. K. Smeltzer, and S. Å. Ellingsen, "Transient wave resistance upon a real shear current," *B Fluids*, 2017.

[31] C. D. Meinhart, S. T. Wereley, and J. G. Santiago, "A piv algorithm for estimating time-averaged velocity fields," *Journal of Fluids Engineering*, vol. 122, pp. 285–289, 2000.

[32] F. M. White, *Viscous fluid flow*. McGraw-Hill, 2005.

[33] Y. A. Cengel and J. M. Cimbala, *Fluid Mechanics, Fundamentals and Applications*. McGraw-Hill, 2010.

[34] F. Ahmed and B. E. Lee, "The production of shear flow profiles in a wind tunnel by a shaped honeycomb technique," *Journal of fluid engineering*, vol. 119, pp. 713–715, 1997.